Oscillation Analysis of Atmospheric Neutrinos in Soudan 2

A dissertation submitted by

Mayly Sanchez

In partial fulfillment of the requirements

for the degree of

Doctor of Philosophy

in

Physics

TUFTS UNIVERSITY

August 2003

Advisor: J. Schneps

Abstract

The discovery of neutrino oscillations, and hence neutrino mass, in both solar and atmospheric neutrinos has been one of the major recent advances in particle physics. Among the many experiments that contributed to the study of this phenomenon. Super-Kamiokande is regarded as the experiment having established neutrino oscillations using atmospheric neutrinos. The final data sample of 5.90 kiloton-year exposure collected by the Soudan 2 detector is studied for the effects of atmospheric neutrino oscillations. These data are analyzed with a maximum likelihood analysis of the neutrino L/E distribution using the Feldman-Cousins approach. The result confirms the discovery of oscillations in atmospheric neutrinos.

To Massimo...

Acknowledgments

Along the path traveled, many hands have held mine. Some of them I encounter everyday, some are looking from afar, some have left this world... without them, this work would not have been completed. To all of them my sincere and deep gratitude.

Jack, thanks to you for showing me the way; without your guidance I would have never found the path to experimental physics. You have been more than a mentor to me; to you and Lucia, thanks for being family.

Tony and Tom, thank you for welcoming me in the Tufts HEP group; I have learnt many things working by your side. To my Soudan collaborators, especially Maury, Peter, Earl and Hugh, thanks for sharing your knowledge and experience with me.

Alex, it has been a ton of good luck to meet you; the forces of optimism and pessimism are now in equilibrium. Thanks for the company and support of your friendship; the road would not have been as fun without it.

Nelson and Adel, you introduced me to the beauty of physics and I would not be here without your advise. To you and my other friends back home, thanks for being there and for not complaining (too much) of my periodic abandonments.

To my friend Javier, you accompanied me a long part of the way in physical presence and you continue to be with me everyday of my life. I wish you could see this.

Mamina, thanks for being what you are; your strength and optimism are with me everyday. Viejin, thanks for the encouragements and disencouragements, they all worked. To my little sister, Gayla, thanks for being there.

Massimo, and Ornitorinko of course, you have been my center and source of peace and happiness, my everything. You believed in me when I would not trust myself. This work I dedicate to you.

The Soudan 2 Collaboration

W.W.M. Allison[3], G.J. Alner[4], D.S. Ayres[1], W.L. Barrett[6], P.M. Border[2], J.H. Cobb[3], D.J.A. Cockerill[4], R. Cotton[4], H. Courant[2], J. Chung[5], D.M. Demuth[2], T.H. Fields[1], H.R. Gallagher[3], M.C. Goodman[1], T. Joffe-Minor[1], T. Kafka[5], S.M.S. Kasahara[2], P.J. Litchfield[4], W.A. Mann[5], M.L. Marshak[2], R.H. Milburn[5], W.H. Miller[2], L. Mualem[2], A. Napier[5], J.K. Nelson[2], W.P. Oliver[5], G.F. Pearce[4], E.A. Peterson[2], D.A. Petyt[4], K. Ruddick[2], M. Sanchez[5], J. Schneps[5], A. Sousa[5], B. Speakman[2], J.L. Thron[1], N. West[3]

[1] *Argonne National Laboratory, Argonne, IL 60439, USA*

[2] *University of Minnesota, Minneapolis, MN 55455, USA*

[3] *Department of Physics, University of Oxford, Oxford OX1 3RH, UK*

[4] *Rutherford Appleton Laboratory, Chilton, Didcot, Oxfordshire OX11 0QX, UK*

[5] *Tufts University, Medford, MA 02155, USA*

[6] *Western Washington University, Bellingham, WA 98225, USA*

Contents

List of Figures

List of Tables

Introduction

This thesis presents the results of the atmospheric neutrino oscillation analysis carried out using the final data sample collected by the Soudan 2 experiment during twelve years of operation. The result offers independent confirmation of the discovery of oscillations in atmospheric neutrinos as established by the Super-Kamiokande collaboration via observation of a variation in the atmospheric neutrino event rate with zenith angle [1]. The relatively small exposure of the Soudan 2 data sample, 5.90 fiducial kton-years, is compensated to some extent by excellent energy and direction resolution achieved with the Soudan 2 detector. The data is analyzed using a method advocated by Feldman and Cousins [2].

The thesis has been organized into seven chapters. The first begins with a brief history of neutrino physics, then discusses some phenomenology of neutrinos oscillations and reviews the current experimental evidence for neutrino oscillations. Chapter 2 briefly describes the Soudan 2 detector and gives details relating to triggering and its simulation via Monte Carlo. In Chapter 3, a detailed description of the data is given. The Chapter describes the data reduction from its raw form to the final event sample used in the analysis. Chapter 4 discusses the treatment of various backgrounds to Soudan neutrino data. Chapter 5 reviews the atmospheric neutrino prediction from various flux calculations and presents evidence for oscillation in the atmospheric neutrino data from Soudan 2. The final chapter presents the analysis using the Feldman-Cousins method to determine the oscillation parameters and confidence level regions. It concludes by comparing these results to other experiments and to the official Soudan 2 result soon to be published.

Chapter 1

Neutrino Physics Overview

Neutrinos are frequently described as mysterious, ghostly particles; very often as a form of matter which cannot be touched and therefore cannot be understood. While these descriptions tantalize our imagination, neutrinos can also be described as one of the best tools to access new physics. Neutrinos have played a crucial role in physics for most of the 20$^{\text{th}}$ century and promise to keep playing a role in this new century. The fact that neutrinos do not participate in electromagnetic and strong interactions, make them ideal as weakly interacting probes which can pass through matter while still providing signals which are accessible to laboratory instruments. Furthermore, the abundance of neutrinos produced in a variety of natural processes has allowed their study even without their production in high flux beams at accelerators.

The neutrino was first proposed as a "desperate remedy" to the problem of β-decay by Wolfang Pauli in 1930. He proposed a light, neutral, spin-1/2 particle that he initially called the "neutron" to explain the continuous energy spectrum of electrons emitted in nuclear beta decay. The other option was to abandon the law of energy conservation in nuclear processes as was suggested by Niels Bohr. The mass of this particle was to be the same order of magnitude as the electron mass, not larger than 0.01 of the proton mass. The proposal initially suggested that this particle was a nuclear constituent so that it would help with the problems of spin and statistics that plagued the description of nuclei that was available at that time.

Two years later, Chadwick discovered what we now know as the neutron. This clearly was not Pauli's particle since its mass was closer to the proton and not to the electron. It was Fermi who gave the neutrino its name in 1931 and a few years later he published his theory of β-decay, the first theory of weak interactions. The theory not only included the neutrino but also described its properties. Fermi's theory was readily accepted because of its excellent description of the electron energy spectrum as measured in the experiments.

More than 20 years later, in 1956, the neutrino was first directly observed. Cowan and Reines working at the Savannah River nuclear reactor in South Carolina, were able to observe the "inverse β-decay" reaction: $\bar{\nu}_e+^{37}\mathrm{CL}\rightarrow\ e^{+}+^{37}\mathrm{Ar}$. Reines was awarded the Nobel prize for this work in 1995; Cowan had already died. The distinction between types or "flavors" of neutrinos was clarified in 1961 at Brookhaven National Laboratory, where the muon neutrino was observed through the reaction $\nu_\mu + X \rightarrow \mu^- + X'$. The latter observation implied the existence of a separate conserved quantum quantity, the lepton family number. The discovery in 1975 of a third charged lepton, namely the tau (τ^-), implied the existence of a third neutrino ν_τ. The measurement of the width of the Z-boson in 1989 confirmed that three light neutrinos should exist, predicting the number of neutrino families with masses less than 1/2 of the Z-boson to be 2.984 ± 0.008. Direct evidence for the tau neutrino was announced by the DONUT collaboration (which includes researchers from Tufts University) in the year 2000, more than 40 years after the ν_e was first observed.

1.1 Neutrino Mass

In the Standard Model of particle physics, the neutrinos are particles of spin 1/2, zero electric charge and zero mass. There is no fundamental symmetry of the model that predicts that the mass is zero as in the case of the massless photon which is required by gauge invariance. However, one cannot just add massive neutrinos to the Standard Model since that would break a useful albeit accidental symmetry of the model, namely $B - L$ quantum number conservation. Consequently, the discovery of neutrino mass implies physics beyond the current Standard Model. Many extensions of the Standard Model have been proposed in which lepton number is violated at some level and massive neutrinos are required. In the underlaying Lagrangian for the

Standard Model and its extensions, a number of different neutrino mass terms are possible. Neutrinos which have "Dirac" masses are distinct from their antiparticles just as the charged leptons (e^-) are distinct from their antiparticle (e^+). However neutrinos may also have "Majorana" masses, in which case each neutrino is its own antiparticle. Majorana mass terms violate lepton number conservation by $|\Delta L| = 2$. Such terms can be interpreted as transitions from an antineutrino into a neutrino or alternatively as the creation or annihilation of two neutrinos. The presence of a Majorana mass term would allow neutrinoless double beta decay which has not yet been observed.

To date, the experimental attempts to measure neutrino mass directly have been unsuccessful, but an interesting set of limits has been produced and the experiments continue to improve. The techniques used include *i*) precise observation of decay kinematics in nuclear or particle decay processes (as in β-decay or muon momentum in pion decay), and *ii*) the utilization of time-of-flight measurement in detection of supernova neutrinos. The best upper limits cited by the Particle Data Group (PDG) [3] are: $m_{\nu_e} < 3$ eV using tritium β-decay, $m_{\nu_\mu} < 0.19$ MeV with CL = 90% using pion decay and $m_{\nu_\tau} < 18.2$ MeV with CL=95% using tau lepton decays.

An indirect method to determine whether neutrinos have mass is to examine neutrino oscillations. This measurement offers the most sensitive method of probing neutrino mass, however it measures only the difference between mass-square values. The possible existence of the neutrino oscillation phenomenon was first pointed out by Pontecorvo in 1957; the possibility of arbitrary mixing between two massive neutrino states was first introduced by Maki, Nakagawa and Sakata in 1962. There is recent compelling evidence that neutrino oscillations explain the long-standing neutrino "anomalies" concerning neutrinos produced in atmosphere and in the Sun and this evidence implies that neutrinos have mass. In the next Section, we review the phenomenology of neutrino oscillations as it relates to atmospheric neutrinos.

1.2 Neutrino oscillations

Neutrinos are mainly created in weak charged current (CC) interactions, which produce eigenstates of the weak interactions $|\nu_\alpha\rangle$, where $(\alpha = e, \mu, \tau)$ corresponding to each charged lepton. In general the weak eigenstates are not identical to the mass eigenstates, however they can be expressed as a unitary transformation of the latter set. For n states $|\nu_1\rangle \ldots |\nu_n\rangle$ with masses $m_1 \ldots m_n$, ignoring time evolution we have:

$$|\nu_\alpha\rangle = \sum_{k=1}^{n} U_{\alpha k} |\nu_k\rangle \tag{1.1}$$

where U is the unitary matrix for the transformation. At the moment of creation a ν_α will be a superposition of mass eigenstates $|\nu_k\rangle$ with energies $E_k = \sqrt{p^2 + m_k^2}$. As the neutrino propagates freely, the different components will evolve differently with phases depending on time and therefore on distance. A pure neutrino state ν_α at $t = 0$, becomes a coherent superposition of the mass eigenstates at a time t:

$$|\nu_\alpha(t)\rangle = \sum_{k=1}^{n} U_{\alpha k} e^{-iE_k t} |\nu_k\rangle \qquad (\alpha = e, \mu, \tau) \; . \tag{1.2}$$

If at least some of the masses are different and if we have a non-diagonal transformation matrix then: $|\nu_\alpha(t > 0)\rangle \neq |\nu_\alpha(0)\rangle$. The amplitude for finding a flavor state after propagation over some distance is

$$\langle \nu_\beta(t) | \nu_\alpha(0) \rangle = \sum_k U^*_{\beta k} U_{\alpha k} \, e^{-iE_k t} \tag{1.3}$$

and the probability of finding ν_β in a flux of ν_α is the square of the amplitude:

$$\begin{aligned} P_{\nu_\alpha \to \nu_\beta}(t) &= |\langle \nu_\beta(t) | \nu_\alpha(0) \rangle|^2 \\ &= \sum_{j,k} U^*_{\beta j} U_{\alpha j} U_{\beta k} U^*_{\alpha k} \, e^{-i(E_j - E_k)t} \\ &= \sum_{j,k} U^*_{\beta j} U_{\alpha j} U_{\beta k} U^*_{\alpha k} \, e^{-i\Delta m^2_{jk} L/2E} \; . \end{aligned} \tag{1.4}$$

Here we have used $E_k \simeq p + m_k^2/2p$ to obtain $E_j - E_k = ({m_j}^2 - {m_k}^2)/2p \equiv \Delta m^2_{jk}/2p$ as well as $L \simeq t$ and $p \simeq E$ (in units $c = 1$) given that neutrinos are highly relativistic. The probability can thus be written as:

$$P_{\nu_\alpha \to \nu_\beta}(t) = \delta_{\alpha\beta} \quad - \quad 4 \sum_{j>k} \mathrm{Re}(U^*_{\beta j} U_{\alpha j} U_{\beta k} U^*_{\alpha k}) \, \sin^2\left(\frac{\Delta m^2_{jk} L}{4E}\right)$$

$$+ \quad 2\sum_{j>k} \mathrm{Im}(U^*_{\beta j} U_{\alpha j} U_{\beta k} U^*_{\alpha k}) \sin^2\left(\frac{\Delta m^2_{jk} L}{2E}\right) \tag{1.5}$$

where we have used the unitarity contraint $\sum_k U^*_{\alpha k} U_{\beta k} = \delta_{\alpha\beta}$. The most obvious consequence of Eq. 1.5 is that if all neutrino masses vanish (or are degenerate) then $P_{\nu_\alpha \to \nu_\beta} = \delta_{\alpha\beta}$ and so there is no oscillation from one flavor to another. Thus neutrino oscillations require neutrino mass. The probability oscillates as a function of L/E. The unitarity of the transformation matrix assures that even if neutrinos change flavor through oscillations, the total flux of neutrinos will be conserved $\sum_\beta (P_{\nu_\alpha \to \nu_\beta}) = 1$. The L/E dependence of neutrino oscillations arises from interferences between the contributions of the different mass eigenstates $|\nu_k\rangle$. However, the interference can only reveal the relative phases of the interfering amplitudes; therefore experiments studying neutrino oscillations can only determine the mass splittings Δm^2_{jk} and not the m_k values directly.

1.2.1 Three-family neutrino oscillations

We now apply the general formalism for neutrino oscillations for the specific case of three-family neutrino oscillations. For this case we write the unitary mixing matrix as:

$$U = \begin{bmatrix} U_{e1} & U_{e2} & U_{e3} \\ U_{\mu 1} & U_{\mu 2} & U_{\mu 3} \\ U_{\tau 1} & U_{\tau 2} & U_{\tau 3} \end{bmatrix}, \tag{1.6}$$

which relates the neutrino mass eigenstates $|\nu_k\rangle$ to the flavor states $|\nu_\alpha\rangle$, *i.e.*:

$$|\nu_e\rangle = U_{e1}|\nu_1\rangle + U_{e2}|\nu_2\rangle + U_{e3}|\nu_3\rangle. \tag{1.7}$$

Since we are interested in the ν_μ component of atmospheric neutrinos, we obtain the probability that a neutrino $|\nu_\mu\rangle$ retains its original flavor as:

$$\begin{aligned} P_{\nu_\mu \to \nu_\mu}(t) \quad = \quad 1 - 4\Big[& |U_{\mu 1}|^2 |U_{\mu 2}|^2 \sin^2\left(\frac{\Delta m^2_{21} L}{4E}\right) \\ & + |U_{\mu 1}|^2 |U_{\mu 3}|^2 \sin^2\left(\frac{\Delta m^2_{31} L}{4E}\right) \\ & + |U_{\mu 2}|^2 |U_{\mu 3}|^2 \sin^2\left(\frac{\Delta m^2_{32} L}{4E}\right)\Big], \end{aligned} \tag{1.8}$$

where the conservation of probability ($P_{\nu_\alpha \to \nu_\alpha} = 1 - P_{\nu_\alpha \to \nu_{\beta \neq \alpha}}$) is clearly implied.

The other expression of particular interest for atmospheric neutrinos is the oscillation probability for $\nu_\mu \to \nu_\tau$:

$$P_{\nu_\mu \to \nu_\tau} = \Big\{ -4\,\mathrm{Re}[U^*_{\tau 1} U^*_{\mu 2} U_{\tau 2} U_{\mu 1}]\,\sin^2\left(\frac{\Delta m^2_{21} L}{4E}\right) - 2\,\mathrm{Im}[U^*_{\tau 1} U^*_{\mu 2} U_{\tau 2} U_{\mu 1}]\,\sin\left(\frac{\Delta m^2_{21} L}{2E}\right)\Big\} + \text{cyclic terms}\,, \qquad (1.9)$$

where we have used the orthogonality relation $\sum_k U^*_{\tau k} U_{\mu k} = 0$. Ignoring the imaginary part, that corresponds to CP violation effects, this simplifies to:

$$\begin{aligned} P_{\nu_\mu \to \nu_\tau} = & -4 U_{\tau 1} U_{\mu 2} U_{\tau 2} U_{\mu 1} \sin^2\left(\frac{\Delta m^2_{21} L}{4E}\right) \\ & - 4 U_{\tau 2} U_{\mu 3} U_{\tau 3} U_{\mu 2} \sin^2\left(\frac{\Delta m^2_{32} L}{4E}\right) \\ & - 4 U_{\tau 3} U_{\mu 1} U_{\tau 1} U_{\mu 3} \sin^2\left(\frac{\Delta m^2_{13} L}{4E}\right)\,. \end{aligned} \qquad (1.10)$$

1.2.2 Two-family neutrino oscillations

A three-neutrino scenario that we will find interesting occurs when two of the neutrino mass eigenstates are nearly degenerate, as the neutrino mass spectrum shown in Fig. 1.1 from Ref. [4],

$$\begin{aligned} |\Delta m^2_{21}| &\equiv \Delta m^2_{\text{small}} \\ |\Delta m^2_{31}| &\cong |\Delta m^2_{32}| \equiv \Delta m^2_{\text{large}} \end{aligned}$$

where $\Delta m^2_{\text{small}} \ll \Delta m^2_{\text{large}}$ and with all $U_{\alpha k} \simeq \mathcal{O}(1)$. Then, by unitarity, Eq. 1.10 simplifies to:

$$P_{\nu_\mu \to \nu_\tau} \simeq 4 |U_{\mu 3}|^2 |U_{\tau 3}|^2 \sin^2\left(\frac{\Delta m^2_{32} L}{4E}\right). \qquad (1.11)$$

This simplification reduces the oscillation probability to a form that depends on the mass splitting among two neutrinos and their respective mixing angles. The problem is thus reduced to a two-neutrino mixing scenario.

For experiments which are not sensitive to the $\Delta m^2_{\text{small}}$ splitting, it is reasonable to study the two-family neutrino case. In these experiments, there will appear to be

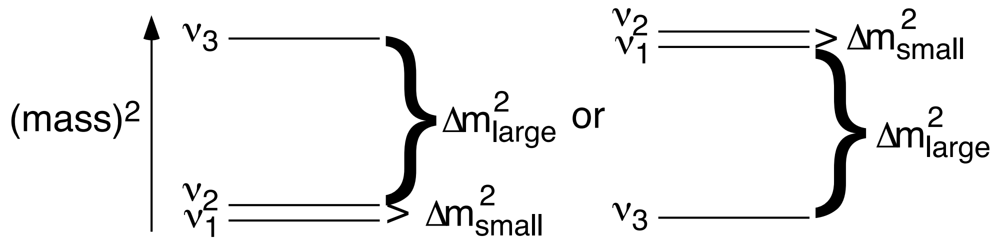

Figure 1.1: Mass spectral patterns for three neutrinos in which the $\nu_2 - \nu_1$ splitting $\Delta m^2_{\text{small}}$ is much smaller than the splitting $\Delta m^2_{\text{large}}$ between ν_3 and the $\nu_2 - \nu_1$ pair. The small splitting may be at either the bottom or the top of the spectrum.

only two neutrinos with distinct masses. The unitary transformation matrix can thus be written as:

$$U = \begin{bmatrix} e^{i\phi_1}\cos\theta & e^{i\phi_2}\sin\theta \\ -e^{i(\phi_1+\phi_3)}\sin\theta & e^{i(\phi_2+\phi_3)}\cos\theta \end{bmatrix}, \tag{1.12}$$

where θ is the leptonic mixing angle and $\phi_{1,2,3}$ are phases. From Eq. 1.12, $4|U_{\mu 3}|^2|U_{\tau 3}|^2 = \sin^2 2\theta$, so that Eq. 1.11 takes the form:

$$P_{\nu_\mu\to\nu_\tau}(t) = \sin^2 2\theta \, \sin^2\left(\frac{1.27\Delta m^2_{\text{large}} L(\text{km})}{E(\text{GeV})}\right). \tag{1.13}$$

where we have considered the factors $\hbar$ and c to obtain:

$$\frac{\Delta m^2 L}{4E} = 1.27\,\Delta m^2(\text{eV}^2)\frac{L(\text{km})}{E(\text{GeV})}. \tag{1.14}$$

Eq. 1.13 is the most commonly quoted form of the two-neutrino oscillation probability. As we have shown it is possible to use it in a three-neutrino "world" under the condition that one of the mass splittings is much smaller than the other. When the three-neutrino case is studied by an experiment for which this relation holds, the experiment cannot see the splitting between ν_1 and ν_2. As we shall see in Sect. 1.3 there is solid experimental evidence for neutrino oscillations: Solar neutrinos have been found to oscillate and the results point to a very small mass splitting, $\Delta m^2_{\text{small}} = \Delta m^2_{\odot}$; atmospheric neutrinos have been found to oscillate and results indicate a large mass difference with respect to the solar neutrino mass difference, so $\Delta m^2_{\text{large}} = \Delta m^2_{\text{atm}}$. It is thus natural to use Eq. 1.13 to study atmospheric neutrinos.

In the above discussion, we have restricted ourselves to a three-neutrino scenario and to its two-neutrino approximation. The current evidence from atmospheric and solar neutrinos suggests two independent mass splittings as in the three neutrino case. Scenarios with more than two mass splittings and therefore more than three neutrinos are not completely excluded from current experimental data. However, there are strong constraints on their possibilities. For instance, a fourth light neutrino must be sterile (not participating in weak interactions) since it is not observed in Z-boson decays. The mass spectrum in a scenario with a sterile neutrino could be: A 3+1 spectrum, where one heavier mass state is separated from three lighter degenerate states or viceversa; or, a 2+2 spectrum where two nearly degenerate mass pairs are separated from each other. The evidence for a third mass splitting suggesting the latter spectrum has been presented by only one experiment, as we shall see later, and it is still in need of confirmation.

We have also restricted our discussion to vacuum neutrino oscillations. However, it must be noted that under certain conditions neutrinos passing through matter gain effective masses through the weak interaction, enhancing oscillations. This effect has been shown to be relevant for solar neutrinos passing through solar material on their way out of the Sun and it is known as the MSW effect. It affects only electron neutrinos since ordinary matter contains electrons and not μ or τ leptons. In the case of atmospheric neutrinos passing through the Earth, it is the muon neutrinos that show oscillations. Therefore no matter effects are expected.

1.3 Experimental evidence for oscillations

As noted previously neutrino oscillation experiments can only measure mass difference but not neutrino masses directly. It is commonly assumed that the largest mass difference approximates the mass of the heaviest mass neutrino, the other masses being negligible. Note that if neutrino oscillations are observed, neutrino mass is implied, but not the reverse, since the masses could be degenerate and thus no oscillations would occur.

An important consideration is the “reach” of the different types of experiments.

Neutrinos (Baseline)	L(km)	E(GeV)	$\frac{L(\text{km})}{E(\text{GeV})}$	$\Delta m^2_{jk}(\text{eV}^2)$ Reach
Accelerator (Short)	10^{-1}	1	10^{-1}	10^{1}
Reactor (Medium)	$1-10^{2}$	10^{-3}	$10^{3}-10^{5}$	$10^{-3}-10^{-5}$
Accelerator (Long)	10^{3}	1	10^{3}	10^{-3}
Atmospheric	10^{4}	1	10^{4}	10^{-4}
Solar	10^{8}	10^{-3}	10^{11}	10^{-11}

Table 1.1: Approximate reach in Δm^2 for experiments studying various types of neutrinos using typical L and E values.

From the oscillation probability Eq. 1.13 we see that an oscillation experiment characterized by a given value of $L(\text{km})/E(\text{GeV})$ is sensitive to a mass splitting, obeying

$$\Delta m^2 \geq \left[\frac{L(\text{km})}{E(\text{GeV})}\right]^{-1}. \tag{1.15}$$

Therefore, to be sensitive to a small Δm^2, an experiment must have a large L/E. Table 1.1 from Ref. [4] shows the Δm^2 implied by the above equation for neutrinos produced in different types of experiments.

Experiments searching for neutrino oscillations can be categorized as either *appearance* or *disappearance* experiments. The appearance experiments search for neutrinos of a flavor that is not originally present in the beam or flux being studied. Evidence in an experiment of this kind would be a “smoking gun” signature that neutrinos do indeed change flavor. This is always complicated because there might be background neutrinos of the same type being searched for, or the new neutrino type might be difficult to detect as in the case of tau neutrinos. Disappearance experiments measure whether some fraction of the neutrinos present in the original beam or flux are not found at a certain distance from the source. Ideally for this type of experiment one would perform measurements of the neutrino flux at different distances from the source. This is not possible in atmospheric neutrinos, however an accurate model of the flux prior to oscillations must be calculated.

Many experiments have searched for evidence of neutrino oscillations. The neutrino deficits in the predicted atmospheric neutrino flux and in the solar neutrino flux have been explained with neutrino oscillations, and quite recently, compelling evidence has been obtained. In the following sections we summarize the current experimental evidence for neutrino oscillations with focus on the more recent and compelling results. A more detailed review of previous neutrino experiments can be found in Ref. [5].

The evidence for neutrino oscillations can be separated in three categories according to increasing mass scale: *i*) strong evidence from the solar neutrinos with confirming evidence from a reactor experiment ($L \sim 180$ km), *ii*) compelling evidence from atmospheric neutrinos and supporting evidence from an accelerator experiment ($L \sim 250$ km), and *iii*) unconfirmed evidence from the LSND experiment ($L \sim 30$ m). There are also constraints from experiments which have not observed oscillations.

1.3.1 Solar neutrinos

Thermonuclear reactions in the Sun produce electron neutrinos, these are the so-called solar neutrinos ($\nu_\odot$). Solar neutrino experiments are characterized by the long path length ($\sim 10^{11}$ km) and the low energy (few MeV) of these neutrinos. The reactions occur via different production chains and several experiments have studied the neutrinos produced in the various chains and reported neutrino deficits with respect to the predicted flux [6, 7, 8, 9, 10, 11]. This deficit was designated "the solar neutrino problem". The neutrino fluxes are predicted in the Standard Solar Model (SSM), which is in excellent agreement with helioseismological observations. The best hypothesis to explain the problem was found to be neutrino oscillations.

Recently the SNO (Sudbury Neutrino Observatory) collaboration has published results from their measurements of the high energy part of the solar neutrino flux arriving to Earth. The neutrinos in this experiment are detected using the reactions: $\nu_\odot + d \to \nu + n + p$ (NC), $\nu_\odot + d \to e + p + p$ (CC) and $\nu_\odot + e \to \nu + e$ (ES). The results offer unambiguous evidence of oscillations since the NC reaction measures the total flux of active neutrinos ($\phi_e + \phi_\mu + \phi_\tau$) independent of flavor and the CC reaction measures the ν_e flux (ϕ_e) which is roughly a third of the expectation confirmed by the

NC measurement. This indicates an oscillation of the type $\nu_e \to \nu_{\mu,\tau}$ and their results (along with those of previous experiments) imply the so called Large Mixing Angle (LMA) solution taking into account the matter effects due to interaction between the neutrinos and solar material. The neutrino properties implied by this result [12] are:

$$\begin{aligned} 2.3 \times 10^{-5}\ \mathrm{eV}^2 \leq &\quad \Delta m^2_{\odot} &\leq 9.3 \times 10^{-5}\ \mathrm{eV}^2 \\ 0.66 \leq &\quad \sin^2 2\theta_{\odot} &\leq 0.88 \end{aligned}$$

.

A very recent result is that published by the KamLAND collaboration [13]. KamLAND is a reactor experiment located in Japan. It is sensitive to electron antineutrinos from several reactor sources at an average distance of 180 km. Their measurements are consistent with the LMA solution obtained from solar experiments, that is, they see a substantial disappearance of the $\bar{\nu}_e$ flux. This is an interesting result, not only because it confirms independently the results from solar experiments, but it also constrains the allowance for CPT violation since this is an antineutrino experiment.

1.3.2 Atmospheric neutrinos

The evidence for neutrino oscillations as the explanation for muon neutrino disappearance in atmospheric neutrinos was reported [1] in 1998 by the Super-Kamiokande experiment (Super-K). This is a 50 kiloton water Cerenkov underground detector located in Japan. Atmospheric neutrinos arise from the decay of pions, kaons and also muons which are produced in the atmosphere by cosmic ray interactions. The pion decay chain

$$\begin{aligned} \pi^{\pm} &\rightarrow \mu^{\pm} + \nu_\mu(\overline{\nu}_\mu) \\ \mu^{\pm} &\rightarrow e^{\pm} + \nu_e(\overline{\nu}_e) + \overline{\nu}_\mu(\nu_\mu) \end{aligned}$$

produces neutrinos in a ν_μ/ν_e ratio of roughly 2:1. Earlier experiments [14, 15, 16], including the Soudan 2 experiment [17], had observed a deficit in atmospheric neutrinos with respect to the predicted ratio. This ratio is known to a much better accuracy (better than 5%) than the overall flux of neutrinos which is known to about 20%.

The deviation from the expected ratio became know as "the atmospheric neutrino anomaly" and was found to be a good indication of oscillations. Atmospheric neutrinos are characterized by the wide variation of their flight distance, from roughly 20 km for down-coming neutrinos to 13,000 km for those traversing the Earth from the far side; while their energies range from the few tens of MeV to TeVs. The observed energy is of course limited by the detector capabilities. On average it is around 1 GeV for events which are fully contained in the detector volume. The atmospheric neutrino oscillation evidence from Super-K is based on the angular distribution of their data sample. There is a deficit for muon neutrinos coming up from the other side of the Earth ($\phi_{\nu_\mu}(\mathrm{up})$), whereas muons neutrinos coming down from just above the detector $\phi_{\nu_\mu}(down)$ show no depletion. The electron neutrinos are on the other hand well described by the predicted flux. Super-K finds in the comparison of these fluxes $\phi_{\nu_\mu}(\mathrm{up})/\phi_{\nu_\mu}(\mathrm{down}) = 0.54 \pm 0.04$. Their results indicate $\nu_\mu \rightarrow \nu_\tau$ neutrino oscillations with the oscillations parameters given by:

$$\begin{aligned} 1.6 \times 10^{-3}\ \mathrm{eV}^2 \leq \quad \Delta m^2_{\mathrm{atm}} &\leq 3.9 \times 10^{-3}\ \mathrm{eV}^2 \\ \sin^2 2\theta_{\mathrm{atm}} &> 0.92\,. \end{aligned}$$

The purpose of this thesis is to show evidence for this same effect in the atmospheric neutrino data collected by the Soudan 2 experiment which is an iron tracking calorimeter which offers an independent confirmation of these results using a very different detection technique. While evidence of this type has been presented by the MACRO experiment [18], the observations are limited to neutrino-induced events which are partially contained and solely ν_μ-flavor. The MACRO detector is a massive planar tracking calorimeter of coarse granularity.

The K2K experiment, an accelerator experiment with a 250 km baseline using the Super-K detector as well, studies ν_μ disappearance and has recently published results [19] that indicate oscillations consistent with the values established by Super-K. Future accelerator experiments, such as the MINOS experiment, will be able to measure these parameters to higher accuracy.

1.3.3 Other neutrinos

The LSND experiment, a short baseline (~ 30 m) accelerator experiment, has been the only experiment to report an appearance signal and it is in a mass scale which differs from any of the experiments described above. They report a signal for $\bar{\nu}_e$ in a beam made by $\mu^+ \rightarrow e^+\nu_e\bar{\nu}_\mu$, suggesting $\bar{\nu}_\mu \rightarrow \bar{\nu}_e$ with a mass scale of $\Delta m^2_{\mathrm{LSND}} \sim 1$ eV^2 [20]. The Karmen experiment has searched for this signal without success and has now excluded part of the region in parameter space allowed by LSND [21, 22]. The MiniBooNE experiment [23] is now searching for $\nu_\mu \rightarrow \nu_e$ oscillations; it has been designed to make a conclusive statement about the LSND evidence. If the LSND result is confirmed, Nature must contain at least 4 neutrinos, since there would 3 independent mass splittings. For the remaining discussion in this work, we will ignore this possibility since the observations reported do not have the level of confidence that the other measurements have achieved.

Another set of interesting experimental results are those that study neutrino disappearance using neutrino beams from nuclear reactors. The reactors produce $\bar{\nu}_e$ beams with neutrino energies in the MeV range. Depending on their baselines the experiments have access to different neutrino mass scales. In particular, the CHOOZ and Palo Verde experiments do not observe any evidence for oscillations, and with a baseline of about 1 km provide the strongest constraint on the amount of ν_e mixing in the atmospheric neutrino mass range [24, 25, 26].

1.4 Summary

The consequences of the experimental results described in the previous section can be displayed as in Fig. 1.2 from Ref. [27], which shows the mass spectrum of neutrinos assuming only 3 active neutrinos. The figure presents the relative mass scales in m^2 for the neutrinos ($\nu_1 - \nu_2 - \nu_3$) in the standard hierarchy; however the order could be reversed in an inverted hierarchy, ($\nu_3 - \nu_1 - \nu_2$).

The picture contains a pair of mass eigenstates, ν_1 and ν_2 separated by a mass splitting of $\Delta m^2_\odot \sim 7 \times 10^{-5}$ eV^2 that drives the solar neutrino oscillations. In addition, the spectrum contains a third mass eigenstate ν_3 separated from the solar

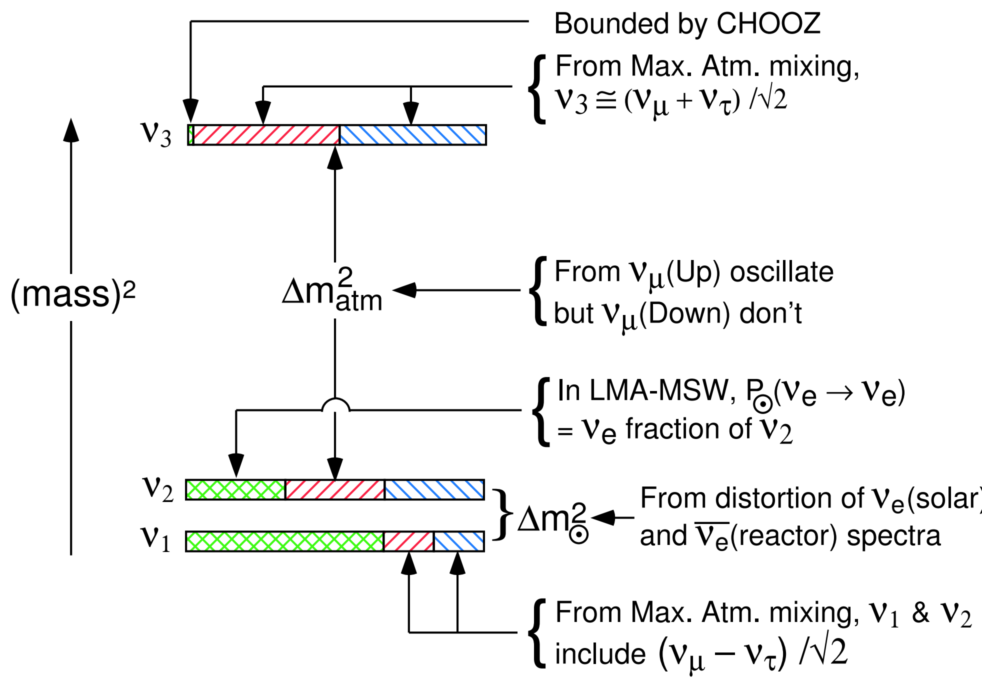

Figure 1.2: A three-neutrino mass spectrum that accounts for the flavor changes of the solar and atmospheric neutrinos. The ν_e fraction of each mass eigenstate is crosshatched, the ν_μ fraction is indicated by right-leaning hatching, and the ν_τ fraction by left-leaning hatching.

pair by a much larger splitting $\Delta m^2_{\text{atm}} \sim 2.5 \times 10^{-3}\text{eV}^2$ that would drive atmospheric neutrino oscillations.

Fig. 1.2 also shows the flavor content of the various mass eigenstates. It is interesting to see where some of these features come from. The component of ν_e in ν_3 is known to be small from the bound imposed by the CHOOZ experiment . The rest of ν_3 is almost entirely ν_μ and ν_τ divided equally due to the close to maximal mixing of the atmospheric neutrinos. Similarly, ν_1 and ν_2 contain equal amounts of ν_μ and ν_τ due to this maximal mixing, but they contain different fractions of ν_e. For ν_2, the solar neutrino data (SNO) and KamLAND indicate that the fraction of ν_e is $\sim 1/3$. The unitarity condition then forces the fraction of ν_e in ν_1 to be $\sim 2/3$.

In this thesis, we present the results of the Soudan 2 experiment that contributes to this picture by confirming the discovery of oscillations in atmospheric neutrinos. Neutrino physics has entered a new phase where we go from Nature's neutrino sources to man-made ones. Many of the measurements done with natural neutrino sources will be improved by these newer experiments where we can tune the experimental setups to measure the oscillation parameters to higher precision and measure the remaining elements of the mixing matrix.

Chapter 2

The Soudan 2 Detector

The Soudan 2 experiment is located at the 27th level of the Soudan Underground Mine State Park, in Soudan, Minnesota. It was proposed in 1981 by the High Energy Physics groups of the University of Minnesota, Argonne National Laboratory, and Oxford University to deploy a 1000 ton tracking calorimeter to study nucleon instability. Within the following two years these groups were joined by the HEP group from the Rutherford-Appleton laboratory and by Tufts University. Soudan 1 was a 30 ton detector running at the time of the proposal which consisted of proportional tubes embedded in concrete blocks. Experience with the Soudan 1 detector provided insights for the design and construction of the new detector. Although the Soudan 2 detector was designed and optimized to search for proton decay modes predicted by Grand Unified Theories (GUTs), the proposal discussed the detection of "background" neutrinos produced by cosmic ray interaction in the upper atmosphere and estimated the rate with energies above 200 MeV to be 200/year/1000 tons. The proposal suggested — in a paragraph of a section entitled "Cosmic-ray physics" — neutrino oscillations might be observed if the the mass squared difference was in a range of 10^{-1} to 10^{-3} eV^2 and it forecast that: "[...] the low expected event rate implies that many years of operation will be needed to obtain a statistically meaningful result" [28]. The first 64 modules of the detector started data taking in April 1989 after a short period of routine operation. The detector reached full operational mass in November 1993, and it continued to run until June 2001. By that time 7.36 kton-years (corresponding to a fiducial exposure of 5.90 kton-years) had been obtained. The atmospheric neutrino sample collected during this time now shows clear evidence for two-state neutrino oscillations.

The detector is located at a depth of 2341 ft (700 meters) from the surface or 2100 meters-water-equivalent. The purpose of placing the detector deep underground is to minimize the cosmic ray background (attenuation $\sim 10^{-5}$ for $\mu^{\pm}$) for the nucleon decay and neutrino oscillations studies. The construction of a dedicated cavern started in 1985 and the assembly of the detector in 1986. The Soudan 2 collaboration is currently comprised of approximately 40 scientists (see page ix) from five major institutions.

A brief description of the detector is given below. Details of its design and early performance can be found in Ref. [29, 30]. Additionally a short description of the triggering, software and Monte Carlo is given in Sect. 2.2; more details on these topics can be found in Ref. [31, 32, 33].

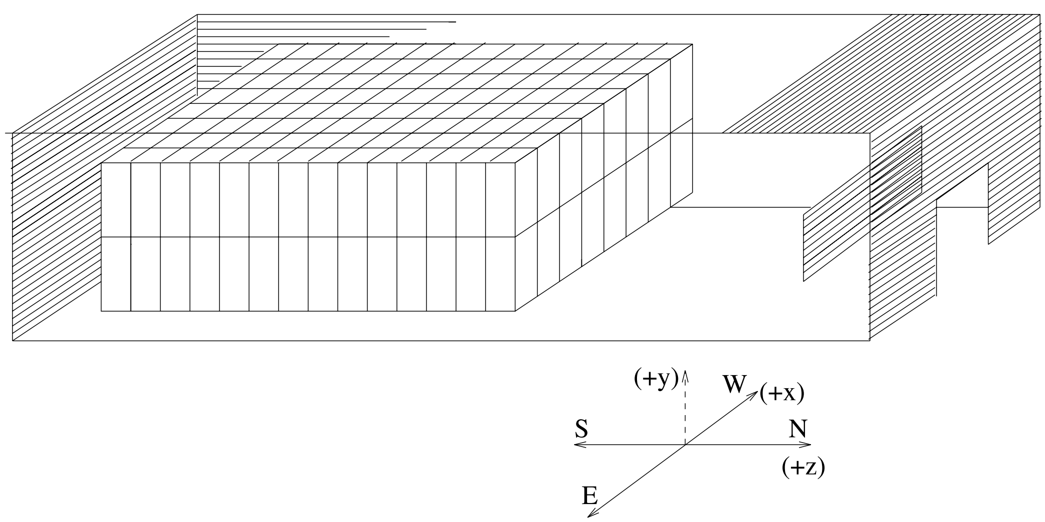

Figure 2.1: The layout of the Soudan 2 main detector and the surrounding veto shield. The detector global coordinates system is also shown.

2.1 Physical description

The main detector is a fine grained tracking calorimeter with a total mass of 963 metric tons. It is composed of 224 calorimeter modules weighing 4.3 metric tons each

(See Fig. 2.1). The modular design allowed the detector to be operated as it was being assembled and to be repaired in case of malfunction with minimal disruptions. However, the modular design has one disadvantage in that it introduces uninstrumented volume ("cracks") through which charged particles can enter or exit the detector, possibly undetected. Openings into these cracks constitute approximately 10% of the surface area of the calorimeter.

Each calorimeter module has dimensions of 1.0 m $\times$ 1.1 m $\times$ 2.7 m. The dimensions were determined by the constraint of fitting a module into the Soudan mine elevator cage. The modules consist of corrugated iron sheets instrumented with drift tubes, filled with Argon-CO_2 gas and read out by proportional wireplanes. A schematic drawing of a calorimeter module is shown in Fig. 2.2. There are 241 layers of 1.6 mm thick corrugated steel sheets of size 1 m $\times$ 0.94 m in each module which provide 85% of the mass of the detector. The layers form a hexagonal honeycomb lattice which support of 1.6 cm outer diameter Hytrel drift tubes. There are 7650 of these tubes per module. The drift tubes are sandwiched between mylar sheets which carry copper high voltage electrodes spaced so as to yield a uniform electric field of 180 V/cm along the axes of the tubes. To prevent breakdown through the mylar to the steel, additional polystyrene insulation is inserted as an extra layer. The drift tubes are filled with a gas mixture of 85% argon and 15% carbon dioxide. This mixture is continuously recirculated through an oxygen removal and purification system.

When a charged particle traverses a tube, the ionization deposited in the gas drifts toward the nearest end under the influence of the electric field. Each module has two wireplanes on opposite sides facing the ends of the drift tube stack. The wireplanes consist of vertical anode wires with high voltage ($\sim$ 2150 V) and horizontal cathode pads held at ground potential (See Fig. 2.3). The charge is collected at the ends of the tubes and the signals on the anodes and cathodes can be matched to determine X and Y coordinates of the hit tube. The data acquisition electronics records the arrival times of the signals, so that the drift time can be used to obtain the Z coordinate of the hit within the drift tube. The nominal drift velocity is 0.6 cm/μsec which gives a maximum drift time of 83.3 μsec. From the knowledge of anode channel, cathode

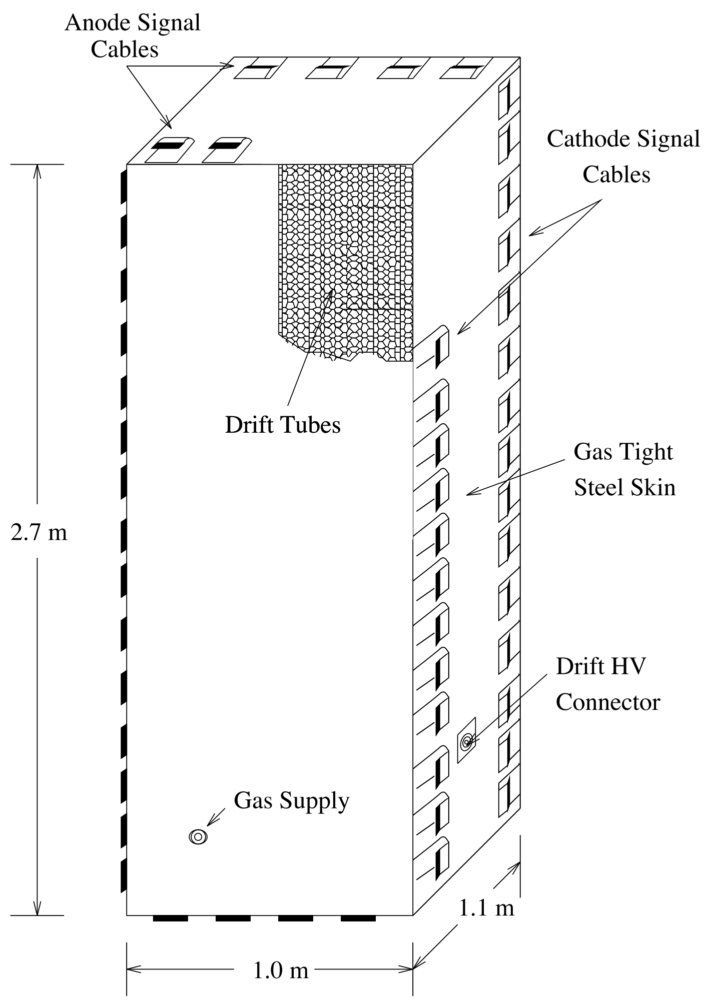

Figure 2.2: One of the 224 tracking calorimeter modules.

channel, drift time and drift velocity, the three coordinates can be determined with a resolution of the order of 1 cm for each of the spatial coordinates. The software that matches the cathode and anode signals requires that the two signals have the same pulse shape.

The wireplane is located 10 mm from the ends of the tubes and the cathode boards are 5 mm behind the wireplanes. A sketch of this layout can be seen in Fig. 2.4. If a particle traverses this 15 mm gap between the tubes and the cathode boards, a large pulse extending across several anode wires and cathode pads occurs at a common time. This charge formation, defined as "blob", is useful in determining the start time T_0

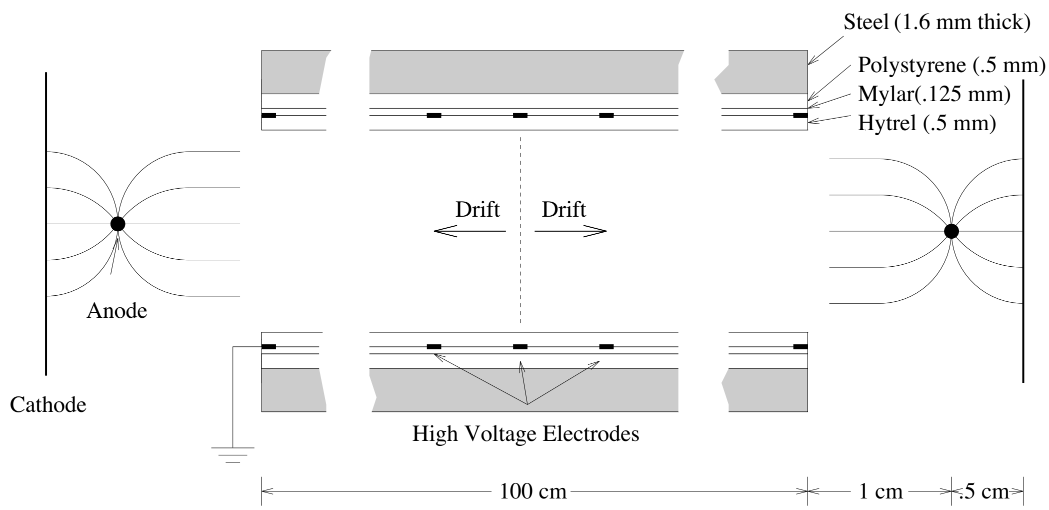

Figure 2.3: A drift tube.

of the event (the time when the ionization was actually deposited in the detector). Since the Z coordinate is determined from the drift time, the difference in arrival times at the wireplane for different hits gives the relative z-distance between hits. However, knowing the location in Z of the event requires determining the absolute z-position of the hits. Since blobs occur only in the wireplane, they are a good source for the absolute z-positon. There is another method that consists in requiring that a reconstructed event is continuous across the boundary between drifting regions, this is known as "loom crossing". Each drift tube has drifting in different directions on either side of its midpoint, these separate drifting regions are referred to as looms. Any event which does not have a wireplane blob nor crosses a boundary will have some ambiguity as to the absolute position in z of the event hits.

The modules of the detector are organized in units of half-walls, consisting of eight modules stacked two high and four across. The detector uses multiplexing for the electronic signal readout by connecting together corresponding cathodes of four modules and corresponding anodes of two modules. This reduces the total number of channels by a factor of eight in the final electronic readout and resulted in large savings on electronic costs. The multiplexing is done so that for events which are of the typical size for a proton decay candidate (1-2 meters), there is no ambiguity as to

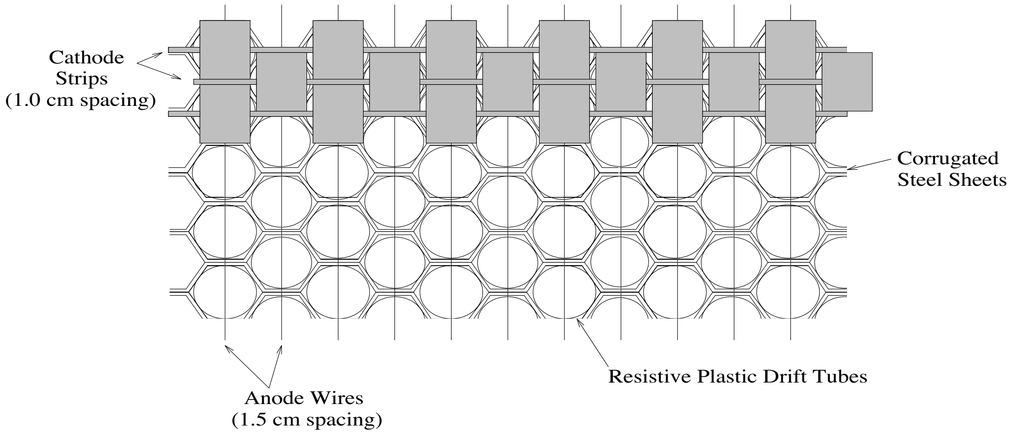

Figure 2.4: A Soudan 2 central module wireplane and a cathode pad section.

the loom location. The summed pulse signals are transferred to flash-encoder ADCs in one of 24 data crates. The digitized values are stored in a 1024 bit buffer each 200 nsec, referred to as a "detector tick". Each data crate is controlled by a local Intel 8086 microprocessor, and in addition it contains a data crate communication card, a compactor card and CAMAC interface, and 15 or 16 ADC cards. Eight anode data crates and sixteen cathode data crates service the detector. Five additional CAMAC crates serve the shield readout system. Table 2.1 shows a number of the main operating parameters of the Soudan detector.

The detector is surrounded by a 1700 m^2 shield of aluminum proportional tubes which comprise the Veto Shield (or Active Shield). It covers the entire ceiling and wall areas and most of the floor. The shield allows the identification of events in which a charged particle either enters or exits the main detector. The shield array provides veto tagging for events which are not completely contained within the fiducial volume of the detector. It was designed and built by the Tufts group and it consists of extruded aluminum manifolds of eight proportional tube cells each arranged in two layers of four. Each cell in a manifold is filled with a mixture of 95% Ar - 5% CO_2 which is recirculated in the same manner as the central detector gas. Anode wires are held at a potential of 2335 volts, consequently a charged particle traversing a region

Location	Soudan, MN 55782 48° N. Latitude, 92° W. Longitude
Overburden	713 m Rock 2090 m water equivalent
Mass	963 metric tons (224 modules)
Dimensions	8 m wide $\times$ 16.1 m deep $\times$ 5.4 m high
Density	1.6 gm/cm^2 (active region)
Composition	85.5% Steel 14.5% Plastic (Polystytrene, Hytrel, Mylar)
Electronics	14,122 Anode channels 26,880 Cathode channels 5,126 Multiplexed 6-bit ADC channels
Resolution	9 mm in the anode - cathode (x-y) plane 10 mm in the drift (z) volume
Threshold	50% trigger efficiency for 160 MeV/c muons 50% trigger efficiency for 130 MeV/c electrons
Radiation Length	9.7cm
Nuclear Interaction Length	$\sim$ 81 cm

Table 2.1: Soudan 2 operating parameters.

of the tube will produce a charge avalanche that reaches the anode wire within 0.8 μsec. The four tubes in a single layer of a manifold are connected in parallel and read out in one channel. A preamplifier and discriminator card mounted on one end of each manifold preprocesses the signals before they are FIFO buffered for 128 μsec. In the event of a detector trigger, this shield buffer is read out along with the main detector data via CAMAC, and shield coincidences with the main detector activity are checked.

Upon readout, if only one of the two layers is fired, a shield "single" is recorded. However, if any number of adjacent layers of the shield manifolds produce signals within 1 μsec of each other, then a single "adjacency" is recorded. An "overlap" is registered when a tube is fired in coincidence with a single or an adjacency in an overlapping panel. These activity categories are used in physicist scans to tag contained data events that are associated with cosmic muon interactions in the walls of the cavern. The operating parameters and geometric efficiency of the shield are given in Table 2.2.

2.2 Triggering, software and Monte Carlo

The central detector is designed to be self-triggering and it is based on the acquisition of several signal pulses within a 72 μsec time window from the pulse processing and discriminating output. Any clock tick which has one or more signal pulses starting is considered an "edge", this occurs when a charged particle traverses a tube in the detector. At least seven edges are required from any sixteen adjacent anodes, or eight edges from any sixteen adjacent cathodes within the 72 μsec time window to generate an edge trigger. This signals the system to read out both the entire detector and shield data buffers. The trigger is designed to reject most of the low levels of ionization from radioactivity due to decays from uranium and K^{40} in the cavern walls, in the concrete, in the G-10 of the wireplanes and in radon gas within the cavern. Compton electrons due to these processes can sometimes produce blobs which are then multiplexed, causing a substancial increase in the random trigger rate. Events

Panels	230
Coverage	1700 m^2
Random Singles	800 kHz
Adjacencies	4.5 kHz
Ceiling Efficiency	97.6%
Floor Efficiency	88%
East Wall	88%
West Wall	89%
North Wall	91 %
South Wall	97 %

Table 2.2: Veto shield operating parameters.

that satisfy the trigger are then written to disk and are subject to further processing.

Since the triggering system records only hits that pass the trigger, the details of the triggering decisions are irreversibly lost. A software simulation of the hardware trigger, called SIMTRIG, was used to simulate the trigger logic for Monte Carlo events.

The Monte Carlo sample generated was 6.1 times the expected data sample for the detector exposure assuming no neutrino oscillations. The Monte Carlo starts with the selection of neutrino energy in the range between 50 MeV and 20 GeV, using the atmospheric neutrino flux provided by the Bartol group (BGS) [34]. Later calculations of the neutrino atmospheric flux were accommodated by weighting the generated events as described in Sec. 5.1. The neutrino interactions were generated in a simulated detector using the NEUGEN package [35, 36] and particle transport using GHEISHA [37] and EGS [38, 39].

Every 240 seconds a data acquisition was randomly initiated irrespective of detector activity. These "pulser" events provided a snapshot of the ambient levels of activity in the main detector and shield. They are used in estimates of background noise rates. They were also used as underlaying events by which real detector noise is added to generated Monte Carlo events, thus making them indistinguishable from the data. The Monte Carlo events and data events were then processed simultaneously and identically through the analysis chain as will be described in the following Chapter.

Chapter 3

Isolation of Neutrino Events in Soudan 2

In non-accelerator as well as accelerator experiments, raw data recorded electronically must be assimilated and eventually codified into quantities suitable for physics analysis. The details of data processing and reduction differ in each experiment. For decade-long experiments such as Soudan 2, these details necessarily reflect the evolution in utilization of the experiment's hardware and in understanding of its analysis capabilities. Two aspects of Soudan 2 data processing which distinguish it from other underground experiments are: *i*) Later steps in the data reduction involves physicist scanning of individual events; consequently intermediate procedures are designed to reduce the number of triggered events which require scanning. *ii*) Originally the detector and the data reduction procedures were intended to search for nucleon decay imaged as fully contained events, with vertices and all event prongs recorded in active detector regions. As a result, processing for events which are not completely contained was added later by expanding upon procedures initially set up to handle contained events.

3.1 Event Samples

There are three distinct samples of events which are either collected (data events) or simulated (Monte Carlo events) for the atmospheric neutrino analysis:

Gold data events: These are data events in which the active shield surrounding the detector was quiet during the allowed time windows. They originate mostly from interactions of atmospheric neutrinos within the detector.

Rock events: These are data events for which veto shield hits are recorded within the event time window. Such events originate with inelastic interactions of cosmic ray muons within the rock surrounding the detector, with some of the resulting charged particles (e.g. pions, protons) entering the detector. These will usually be registered by the shield, in which case the event will be a shield-tagged rock event. However if no charged particles hit the shield but some neutral secondary particle (e.g. gammas, neutrons) enters the detector, it will produce a shield-quiet rock event which may enter the gold event sample.

MC events: These simulated events are the product of a full detector neutrino Monte Carlo (MC) simulation which is used to generate events representing reactions to be expected from the flux of atmospheric neutrinos described in Sect. 2.2. These neutrino MC events are injected, with their identity concealed, into the data stream throughout the entire exposure of the experiment.

Each event of the above samples proceeds through a standard data reduction chain. Both collected and simulated events pass through identical steps in the chain. The starting point is a detector hardware trigger. For an event to be recorded, the central detector requires at least seven contiguous pulse edges to occur within a 72 μs window. Then a trigger is registered and the calorimeter modules read out. For MC events which obviously lack a hardware trigger, a subroutine SIMTRG is called which rejects events that would not have satisfied the hardware trigger. From this point in the data reduction chain the above three event samples are treated in exactly the same manner.

3.2 Data Reduction

After triggering, the data in raw form (from the data crate output) is separated into events corresponding to each trigger and written to disk. The initial processing is done with a combination of software routines that belong to the software framework Soudan

Off-line Analysis Program (SOAP). Within this framework, different Fortran routines add information for these events such as pulse matching, event reconstruction, blob identification, T_0 determination and track identification. Additional routines identify single muons, multiple muons (MMU), horizontal muons (HMU), stopping muons (SMU) and other specific event types.

The SOAP framework relies on BOS (Bank Organization System), a dynamic memory management system that allows data storage and retrieval at different stages during processing. The data is stored in structures called banks. As each of the SOAP routines is executed, it reads from previously produced BOS banks and produces new ones. Other input needed by the SOAP routines are detector constants valid at the time the event was observed. These values are stored in the Soudan 2 database in BOS banks with assigned validity ranges. After this initial processing the data events pass through a series of software filters and physicist scans which extract events of interest, mainly neutrino and nucleon decay events. Note that through-going muons are not considered in this thesis. The earlier neutrino analyses in Soudan 2 [17] were performed with events that were completely contained in the detector. Thus there is an optimized data reduction chain for these events. Later, with the idea of exploring higher neutrino energies, a special data extraction and processing chain was set up for the partially contained neutrino events. In the paragraphs below I summarize the differences in processing for contained and partially contained events and describe how certain categories of events arise in the processing chain and have been subsequently added to the final data set. For a detailed description of the various stages of the data reduction see Ref. [30] for contained events and Ref. [40] for the partially contained events.

3.2.1 Contained Events (CEV)

The data reduction chain that leads to the "contained events" (the CEV sample) consists of two levels of software filters and two levels of physicist scans. The main objective of the initial software filters is to minimize the amount of uninteresting events that the physicists have to examine, since human scanning is very time-consuming. On the other hand, our procedures must preserve as many neutrino events as possible.

The first software filter, or Pass 1 ('Loose Cuts') filter, attempts to reject events which are clearly not contained or have an obvious problem related to detector malfunction. This filter is the combination of two separate software filters, the HIT filter and the SEARCH filter. The HIT filter analyzes clusters of hits, checking that the event topology is clearly inside the fiducial volume (events must have all hits more than 20 cm from the detector exterior) and that the identified cluster is not characteristic of a detector breakdown. The SEARCH (also know as TRACK) filter looks at 2-d (x–z and y–z) tracks in the event in order to reject incoming cosmic ray muons.

The Pass 3 (or 'Hard Cuts') filter begins with a more stringent set of the same cuts applied with the Pass 1 filter. In essence, the filters used are the same HIT and SEARCH filters but with more strict parameters on trigger, cluster containment, event size, crack muon, shield cut, etc. An extra set of conditions, known as final cuts of the Pass 3 filter, are applied, reducing further the number of resulting events to be scanned.

Before the output of the Pass 1 filter goes into the Pass 3 filter, the proper functioning and performance of the detector is checked during the period the data was taken, and 'Run Quality Cuts' are imposed. Further detector checks to ensure data quality are completed after reconstruction, see Ref. [41].

After the software filters, physicists examine all the surviving events, rejecting those that do not fulfill a given set of scan rules. The CEV FILTER scan is designed to eliminate residual events which are not contained and which have not been rejected by the software filters. It also rejects any remaining events that are due to detector or electronics malfunctions.

The second scan is the CEV BRONZE scan; it is used to further check containment and to provide an initial classification of events on the basis of topology. The rules used in this scan and described in Appendix A.2 are more difficult to apply than the ones at the FILTER level and are subject to interpretation. Bronze scans are carried out independently by at least two scanners and a certain degree of experience is required. Containment issues to be checked at this stage include: *i*) whether the event fails the filter rules; *ii*) whether it points out of the detector through a crack or an uninstrumented region of the module; *iii*) whether it leaves parallel to the anodes, and *iv*) whether other possible problems with the detector or the event itself exist. Once containment is assured the event is classified in one of three topology categories, namely track, shower or multiprong. Examples of reconstructed events in these categories are shown in Fig. 3.1a, Fig. 3.1b and Fig. 3.2. A detailed description of the different topologies and event types is given in Sect. 3.2.3.

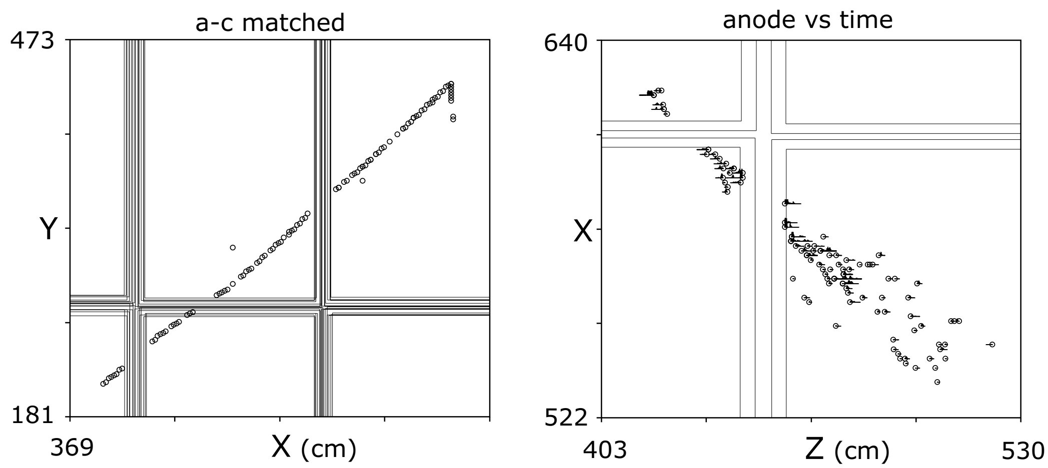

Figure 3.1: a) A quasi-elastic muon event having a long muon track and a short proton; b) a quasi-elastic electron event having a single $e^{\pm}$ shower.

During these scans, events that end in cracks (spaces between the detector modules) or have vertices outside the detector active region are rejected. Such events are more susceptible to background contamination in the atmospheric neutrino analysis context. On the other hand, events with several prongs are more likely to have at least one or two prongs ending on a crack; therefore throwing away all such events would significantly reduce the sample of multiple pronged events. It was decided to flag such events as potentially interesting for further studies. These events were later introduced into the processing chain as separate categories [42], although they are in fact contained events:

CVC events: Contained Vertex, track ends on an interior Crack.

VOA events: Vertex starting Outside the detector's Active region, in an interior loadplate or module sideskin.

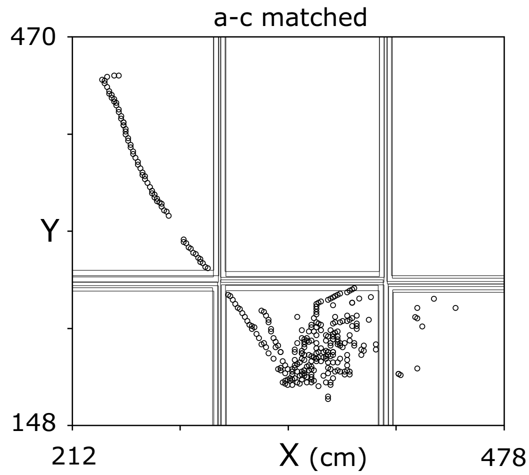

Figure 3.2: Multiprong event with a leading muon track which decays and some hadronic activity.

The rules used in the CVC scan are described in Appendix A.3

In scanning, it is also possible to find events which fall into the "Partially Contained" event or PCE category. Such events were flagged and were considered in subsequent studies as PCEs found in the CEV scan. Additionally all track events were subjected to a procedure that determines "protonicity", the probability that a track event is a proton. Single track events that were determined to be protons according to trajectory straightness and relatively high ionization were placed into a separate topology category.

3.2.2 Partially Contained Events (PCE)

Study and use of Partially Contained Events (or PCEs) was initiated after the CEV acquisition and reduction chain was completed. This required the creation of a special PCE filter that could be run on the same raw data as the initial CEV software filters (Pass 1 and Pass 3); as a result, a parallel data reduction chain was established for which the scanning rules and procedures were modified. The PCE filter was used after some of the initial SOAP routines had been run.

The purpose of the PCE filter was to reatin events that might have been produced by a neutrino interacting within the detector but for which the resulting lepton is not fully contained. The filter has two stages; the initial one accepts 0.6% of the incoming triggers including all stopping tracks and produces SMU files. This is achieved by requiring that there are no through-going tracks in the event, that the track is not characteristic of a malfunction of the detector, and that the candidate vertex is within the fiducial volume of the detector. The event must not be coincident with shield hits located on opposite faces of the shield.

In successive filter tests the resulting SMU files, which contain mostly downward stopping cosmic ray muons and through-going muons passing in part through a crack, are evaluated according to cluster containment, track length and other criteria related to shield hits and distances to the top or bottom of the detector. These selections reject 97.5% of the events in the SMU files. The resulting files contain a combination of downward stopping muons, through-going muons, partially contained events, contained events and upward-going stopping muons.

A partially contained neutrino candidate is defined as an event that has a clear and well-defined vertex within the fiducial volume of the detector and an outgoing lepton which clearly exits the detector (either directly or through a crack). In order to isolate these events from the other varieties, the sample which survives the software filter processing is subjected to multiple scans.

The first phase is the "Single scan" where all events are scanned by at least one experienced physicist scanner and classified. Some of the categories in this scan are shared with the CEV scan, but it also includes categories particular to the PCE scan. The categories of interest for our analysis are the PCE 2-prongs and PCE multiprongs, examples of which are shown in Fig. 3.3a and 3.3b.

The single scan is followed by a "Check scan" wherein the interesting categories are independently evaluated by a second scanner. Several iterations may be required until agreement is reached on all events. The final scans are the "Edit scans" in which the event T0 is specified, mass hypotheses are designated for the individual prongs, and the overall event flavor is assigned.

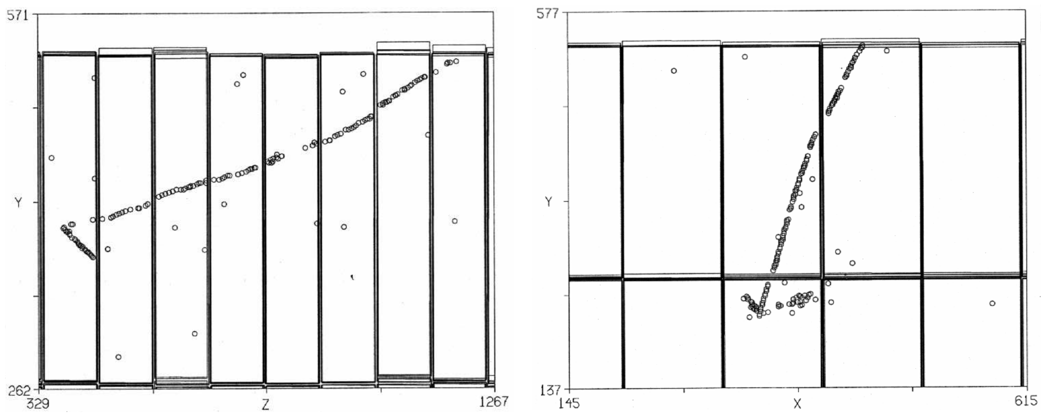

Figure 3.3: a) A PCE 2-prong with a leading muon track that exits the detector and a proton track at the vertex; b) a PCE multiprong with a leading muon track exiting the detector and a hadronic system of several prongs at the vertex.

3.2.3 Event Reconstruction

Once topologies and CEV, CVC, VOA or PCE categories are assigned, the momenta of the identified particles need to be determined. Events are reconstructed by physicists using the STING interactive graphics package. Table 3.1 shows the number of events reconstructed in each of the scan categories. Note that CVC and VOA events comprise a small fraction of the overall contained event sample.

Good separation between tracks and showers is essential for accurate identification of the topology of each event. A visual examination of the events allows muon tracks to be distinguished from electromagnetic showers [43]:

– A muon deposits its energy along a continuous line of tubes forming a track. Occasionally the muon decays, leaving a small shower at the end of the track and thus depositing ionization in tubes that do not cross it trajectory. Recoil proton tracks are generally shorter than muon tracks, are more heavily ionized, and have straight trajectories whereas muons exhibit small-angle multiple scattering.

– An electromagnetic shower initiated by an $e^{\pm}$ particle or by gamma conversion, may exhibit a track-like pattern at outset. However as the shower develops, the tube hits usually spread along the initial direction yielding a plume-like pattern with gaps separating some of the hits. When the shower traverses individual tubes, the ionization may exhibit multiple peaks as a result of electron multiplication within the developing shower.

Based upon the degree of containment and upon the observation of a single track or single shower or multiple prongs in an event, events are assigned one of the following topologies:

Single Track: The event has a single track which is not a proton track; it may also be accompanied by a proton track which is either prompt (recoil proton) or remote (produced by a recoil neutron) from the candidate vertex. The track may also have an endpoint decay (a low energy electron shower). Events in this topology predominantly originate from ν_μ or $\hat{\nu}_\mu$ quasi-elastic reactions.

Single Shower: The event has a single electron or gamma induced electromagnetic shower, and possibly a recoil nucleon. These events predominantly originate from ν_e or $\hat{\nu}_e$ quasi-elastic reactions.

Multiprong: These are non quasi-elastic (hence inelastic) contained events that do not fit the single track or single shower topology, having more prongs. They may be either charged current or neutral current inelastic neutrino events.

Single Proton: These events contain a single track considered to be a proton. This classification is done with the help of the protonicity procedure [44] and further scanning. Events placed in this category predominantly originate from neutron elastic scattering though they may have a neutrino neutral current contribution. This sample has not been subject to detailed analysis and is not used for the purposes of this thesis.

PCE 2-prong: These are partially contained events with an exiting muon or electron and a second track prong (usually a recoil proton).

PCE multiprong: These are partially contained events with multiple hadronic prongs.

Initially, contained single tracks and single showers were reconstructed by physicists at Argonne, Minnesota, Tufts and Rutherford. The resulting reconstructions

		Gold	Rock	MC
CEV	single trk	172	416	1374
	single shw	237	694	1279
	multiprong	196	317	1215
CVC	single trk	5	3	49
	single shw	2	0	17
	multiprong	5	5	61
VOA	single trk	2	0	21
	single shw	1	0	17
	multiprong	4	3	42
PCE	2-prong	2	1	23
	multiprong	69	14	540

Table 3.1: Population of Soudan-2 event samples subdivided according to category and topology.

were subjected to a number of remeasurements to ensure reliable identification of recoil protons and determination of momenta. Later, the Tufts group reconstructed all of the remaining topologies and, following numerous comparisons, the reconstructions provided by Tufts became the ones used in the atmospheric neutrino analysis [45].

Shower and tracks are identified using mark points, one placed before the first hits of the prong and a second placed along the prong to help determine direction. An additional mark is used to locate the vertex. The mark numbers are used for assigning particle ID for final-state prongs and scan scan flags to indicate remote, scattering or decaying particles. Muon, proton and pion tracks are reconstructed using the routine TRAJEC which fits a polynomial curve through all hits associated with the track and returns the range, energy and initial direction vector. Electron showers are reconstructed using the routine SHOWER. It uses a clustering algorithm to determine shower size, initial direction and energy for a cluster of hits tagged as shower hits. After each event is reconstructed, the information is saved to a file whose name includes the run and event number and the identifying topology. It is during subsequent processing of these event files that other physical quantities, such as event energy, invariant mass, event momentum, etc., are calculated.

3.2.4 Reduction of Event Files to DST records

The reduction of event reconstruction files to Data Summary Tape (DST) records was an activity which developed over a number of years at Tufts. Consequently there arose a series of different software packages which were devoted to the task. In order to maintain a degree of continuity, software for new tasks was usually added, as opposed to subjecting older codes to renovation. Considerable effort was made to make the data reduction steps as automated as possible; nevertheless a full round of processing was required each time new data was added. Event categories which are present at the onset of each processing cycle are shown in Table 3.1. In paragraphs below we briefly describe the data reduction steps. Specific run-time details are provided in Appendix B.

In the Tufts reconstruction, each event is saved to a single binary file (RECONOUT format) after reconstruction. All of these event files are joined into one large file per category and topology. Next the software package RDST8 is run to convert the reconstructed banks for each event into ASCII card images (DSF files). The card images summarize for each event: the event ID plus topological, geometric and kinematic information obtained by scanning and measuring. A detailed description of the DSF format appears in Appendix E of Ref. [46].

For each event category, the output of the RDST8 package is processed by the MCFLAV package. This software was originally developed by William Leeson [46] to assist with determining the flavor of multiprongs. The flavor of events in the contained single track and single shower sample is effectively determined by the bronze scan. That is, single track events are presumed to be interactions of ν_μ flavor neutrinos (mostly $(\nu_\mu + \hat{\nu}_\mu)$ quasi-elastics), and single shower events originate with neutrinos of ν_e flavor.

For multiprongs, MCFLAV determines the prong wich has the highest final state momentum but which is not a proton, nor a scattering track, nor a remote shower or track. It outputs the results to an ascii file (FOR-053.DAT). A physicist then scans all the multiprong events with the aid of the information in this file and determines the most likely flavor for each event. In each event, track prongs have been classified as being protons, charged pions or muons; shower prongs have been classified as either gamma or prompt electrons. The prong classification criteria used during reconstruction are:

1. **For tracks:**

   Protons are distinguished from $\mu^{\pm}$ and $\pi^{\pm}$ as being heavily ionizing tracks with relatively short, straight trajectories. Non-proton tracks with secondary kinks or scatters are identified as charged pions. Non-proton tracks without kinks or scatters are regarded to be either muons or charged pions. Tracks that do not appear to be connected to the event primary vertex are labeled as remote tracks.

2. **For showers:**

   A shower which starts beyond 7 cm from the vertex is assumed to be a gamma shower; a shower whose first hit is within 7 cm can be either a prompt electron or a gamma shower. On an event-by-event basis, shower pairs that yield an invariant mass in the range $80 - 200$ MeV/c^2 are considered π^0 candidates. Showers that do not appear connected to the vertex are labeled as remote showers.

The prong with the highest momentum, which is neither a proton, nor a scattering pion, nor a remote track or shower, is identified as the charged current lepton candidate. Then, each event is assigned a neutrino flavor as follows:

ν_μ **flavor:** If the charged current lepton candidate – the leading prong – is a muon track and its momentum exceeds 200 MeV/c, the event is assigned CC ν_μ flavor.

ν_e **flavor:** If the charged current lepton candidate is a prompt shower and its momentum exceeds 200 MeV/c, the event is assigned CC ν_e flavor.

NC or ambiguous flavor: If the event lacks a prompt lepton prong with momentum exceeding 200 MeV/c, the event is regarded to be a neutral current candidate. It is also possible that two or more hypotheses may characterize the event

Flavor Assigned	MC Truth ν_μ	ν_e	NC
μ	1695.3	101.2	180.9
e	74.7	1610.9	162,5
"NC"	70.0	62.0	74.2

Table 3.2: Flavor identification matrix for "blind" flavor tagging of neutrino MC events.

image, *e.g.* CC ν_e and NC ; such events are assigned to an "ambiguous flavor" category according to the different hypothesis combinations.

Flavor tag decisions are then edited into the FOR-053.DAT file. A history file is kept to minimize the flavor tagging each time a new set of events is added. Results for this identity-blind flavor tagging of the neutrino MC are displayed in Table 3.2.

After the flavor tagging is done, another software package is applied to the modified output files from MCFLAV in order to produce a set of NTUPLE (PAW binary format) and ASCII files (ASC files) [47]. This step combines the multiple files per category in the MCFLAV output into a single file with the physical quantities needed for the analysis.

This final set of ASCII files is made available for DST-making. Further processing at this stage includes merging of the truth information for all Monte Carlo events, calculating various event category tags (such as HILOFL, PCEFL, FL300), applying energy corrections, and other corrections explained in the next Section. The final output is a single file known as the Final DST containing all events.

3.3 Final DST

Each event in the Final DST has one entry and each entry contains two sections. The larger section is the "MaxiDST"; it holds all of the uncorrected information for the event (total energy, direction, etc.) and contains four-vector information for each of the reconstructed prongs. The smaller section is the "MiniDST"; it carries some of the same information after corrections have been applied, and all physical quantities and tags are corrected for use in the final analysis. Note that some of the corrections

Lepton Energy (MeV)	0-200	200-400	400-600	> 600
$\Delta\theta$ ν-lepton	$\sim 90°$	$75°$	$49°$	$28°$
$\Delta\theta$ ν-(lepton+proton)	$30°$	$23°$	$15°$	$8°$

Table 3.3: Resolutions, calculated as full-width-half-maximum of $|\theta_\nu - \theta_{recon}|$ distributions, for reconstruction of the incident neutrino direction using quasi-elastic events in Soudan 2.

applied to the MiniDST section were done manually. As a result, this section is a historical archive which must preserved. For reference the format and variables of the Final DST are described in Appendix C.

In the paragraphs below we describe the steps taken to produce the MiniDST section from the MaxiDST. These steps incorporate all the corrections and cuts developed by the Collaboration in order to obtain the final physical quantities for each event. These selection and cut criteria provide a foundation for all future analyses.

3.3.1 CEV Selections and cuts

Studies of Monte Carlo samples of single track and single shower contained events show that good event direction resolution is achieved when final-state leptons have energies exceeding 600 MeV. For final states having leptons of energy lower than this, it was shown that reliable pointing could be recovered for quasi-elastic events whose recoil protons were visible at the primary vertex. Applying these observations (see Table 3.3), a series of selections for a high resolution sample (HiRes) were defined as follows [47]:

– For single track and single shower events in which only a lepton prong is visible, we require the visible energy to exceed 600 MeV.

– For single track and single shower events which include a recoil proton, we require the lepton momentum to be higher than 150 MeV/c.

– Multiprongs after flavor tagging are required to have visible energy greater than 700 MeV, with net momentum exceeding 450 MeV/c and with the prong identified as the lepton having momentum greater than 250 MeV/c.

		Gold	Rock	MC
Contained LoRes	ν_μ	114	364	710
	ν_e	142	652	705
	MP	69	94	335
NC or ambiguous	–	46	190	246

Table 3.4: Populations of contained LoRes and "NC or ambiguous" event samples prior to the 300 MeV/c momentum cut.

The second requirement above for quasi-elastic events with recoil proton eliminates situations where a track with decay could be confused with a shower plus a recoil or vice versa. The requirements on visible energy and net momentum for multiprongs ensure that the events utilized have clear directionality and reliable flavor-tagging. These cuts ensure a resolution (FWHM) for recovering the incident neutrino direction of better than 28°.

The above criteria define the HiRes event sample; they are to be applied before making some of the corrections to the final physical quantities to be used in the analysis as described in Sect. 3.3.3. The reason for this is that the HiRes selection studies were done before the studies for the final corrections. Events that do not pass HiRes requirements are assigned to the low resolution category (LoRes), including neutral current and multiprong events of ambiguous flavor.

The LoRes sample contains relatively high levels of rock background as was shown in Ref. [48]. It was determined that an appropriate cut was to require the lepton momentum for single track and single shower events to be above 300 MeV/c. In the case of multiprongs, the total visible momentum was also required to exceed 300 MeV/c. Category populations of events in the contained LoRes sample before this cut are shown in Table 3.4; the numbers are to be compared with those after the cut shown in Table 3.5. We note that there is a considerable reduction in rock background for the different classes of events between Tables 3.4 and 3.5.

3.3.2 PCE Selections and cuts

Selection criteria are also applied to partially contained events beyond the scanning restrictions in order to minimize background events [40]. Cuts are placed on the "hadronic prong hits" and the event vertex depth. The hadronic prong hits are the number of hits around the candidate event vertex excluding those due to the lepton prong. The number of hadronic hits must be significantly higher than the maximum number of hits that result from end-point decay electrons from stopping muons. All events with less than 10 hits are eliminated by the scan rule for downward stopping cosmic ray muons. A further requirement, on PCE 2-prongs specifically, is that the number of hadronic prong hits be 20 or more, safely excluding residual background from downward stopping muons with endpoint decays.

For PCEs, examination of event vertex distributions shows that rock events tend to occur at shallow depths (D $<$ 80 cm). However, depth fits show no evidence for rock contamination in the PCE gold sample [40]. Instead, there is a need for a minimum track length to facilitate the event flavor identification and to facilitate energy and direction determination. A depth cut for ν_μ-flavor PCE candidates of 40 cm is required in order to ensure suitable muon track length. These cuts and distributions are discussed in more detail in Sect. 4.2.4.

Further investigations [49] found that one could include more ν_μ-flavor PCE candidates with a lower number of prong hits ($4 \leq$ PRHITS < 20) as long as they were downward going ($\cos\theta_z > -0.05$) and a cut was imposed on the minimum muon track length (MULEN $>$ 150 cm). This set is known as the "In-Downs" (CEVCVC = 8 and FLAVR = 1); and also (CEVCVC = 4 and FLAVR = 31). These are events that on scanning were evaluated to have a muon that exits rather than enters the detector. The requirements prevent the introduction of background in the sample while maximizing the statistics of the PCE sample. In-downs with lower prong hits were considered to be contaminated with up-stopping muons and their inclusion has been postponed until study of the latter sample is completed.

In an effort to use all data available, one other PCE sample was isolated to be added to the final data set [50]. This is a sample of non-ν_μ-flavor PCEs comprised predominantly of events assigned to ν_e flavor on the basis of observation of prompt showers which are the most energetic prompt prongs in these events.The sample also includes events which have ambiguities between or among ν_μ, ν_e and NC flavor assignments. Events in this sample are required to be multiprong events. With this sub-class of PCE events, it is necessary that enough of the event final state is visible to enable reliable separation from incoming showers. This is achieved by imposing a more stringent vertex depth cut, namely 80 cm. Also a stricter cut in visible energy is imposed in order to minimize rock contamination: $E_{vis} > 900$ MeV.

3.3.3 Corrections

All events in the Final DST are measured according to Tufts reconstruction rules [45]. In order to construct and correct the kinematic variables for the MiniDST, the following steps were taken starting from the MaxiDST values:

1. **Nucleon recoil identification and nuclear binding energy:** The original Monte Carlo simulations for Soudan 2 did not fully account for nuclear binding effects. As a result, the kinetic energies of outgoing nucleons in quasi-elastic scattering are overestimated by 30 MeV on average [51]. The effect of this was noted as a disagreement between the fraction of events which have recoils in the data compared to those in the Monte Carlo. The correction method proposed in Ref. [51] is to shift the Monte Carlo hit distributions by a single hit count in order to match the data. The proposed method requires:

   – For single tracks, eliminate recoils having less than or equal to 1 hit for data and recoils having less than or equal to 2 hits for MC.

   – For single showers, eliminate recoils having less than or equal to 2 hits for data and recoils having less than or equal to 3 hits for MC.

   – For multiprong events with proton tracks, take no action.

   The above requirements satisfy earlier suggestions [52] based on the reliability of the scan assessments, that single hit recoils not be used for tracks and one and two hit recoils not be used for showers (both for data and Monte Carlo). Events having a rejected recoil have their total event energy and momentum estimated from the lepton alone. This correction is applied before any HiRes selections are considered. For the corrected events the new values for visible energy (E_{vis}), total momentum (P_{tot}), and the presence of recoil flag (REC) are recorded in the MiniDST section.

2. **Shower hit cut:** It is known that electronic noise can produce small blobs of hits that resemble a shower. To address this issue, we require the number of hits in a single shower, including possible recoils, to be greater than 9 hits.

3. **Monte Carlo shower energy correction:** In independent studies [53, 54, 55] two important Monte Carlo discrepancies were identified: *i*) The reconstructed energies of MC showers were systematically $\sim 16\%$ lower than the truth values; *ii*) the data and Monte Carlo energy distributions disagreed by a similar factor, due to a disagreement in the average numbers of hits present in the data versus MC showers. It was eventually determined [56] that the two problems were related and were due to the tracking threshold set at 1 MeV (the minimum value endorsed by the EGS3 authors) in the production Monte Carlo. This threshold artificially limited the production of shower hits in the Soudan 2 Monte Carlo. Lowering the threshold to energies below 1 MeV produces a 15% increase in the number of shower hits which explains the effects observed in (*i*) and (*ii*).

   A method was proposed [57] which corrects the underlying problem, namely the shortage of hits in the production Monte Carlo. The number of hits in all electromagnetic Monte Carlo showers is increased by 15% and the energy is recalculated using the formula used by the SHOWER processor (for Tufts reconstructions the formula is the one used in SOAP Release 22). This correction is applied before HiRes selections are made.

4. **Calibration of momentum with respect to Monte Carlo truth:** Beyond the shower energy correction, small discrepancies remained in the overall calibration of momenta for tracks and showers with respect to Monte Carlo truth. One of the studies that confirmed the magnitude of the shower energy problem [55] also proposed a procedure for solving these residual differences.

   For MC event samples, the measured momentum is fitted to the true momentum and an overall calibration factor is obtained separately for tracks and showers. The correction factors are then applied to the measured MC and the data momenta, since the remaining issues are most likely due to deficiencies in the reconstruction.

The fit using the above method for the muon tracks gives the factor: 0.97 ± 0.02. The fit for the electron showers yield a similar value: 0.96 ± 0.03. These are relatively small corrections and they confirm that the method used to correct for the shower energy was appropriate. This correction is applied before any HiRes selections are made.

5. **Neutron recoil correction:** For events having neutron recoils, that is, proton tracks which are remote from primary vertices, the recoil is not considered a proton recoil for the HiRes definition. The neutron recoil prong momentum is added to P_{tot} and E_{vis} as reconstructed; the possible neutron flight path is not taken into account. The HiRes selection on E_{vis} is applied after this correction.

6. **Cuts and Selections:** All selection and cuts criteria described in Sect. 3.3.1 and Sect. 3.3.2 are applied at this stage. The selected HiRes, LoRes and PCE samples are based on physical quantities as corrected in the previous steps. The new values for visible energy (E_{vis}), total momentum (P_{tot}) and the presence of a recoil flag (REC) are written in the MiniDST section after all the corrections are made.

7. **Addition of invisible recoil energy:** For HiRes quasi-elastic events (single tracks and single showers) without a visible recoil, 180 MeV is added to the visible energy; for LoRes quasi-elastic events, 140 MeV is added. These corrections are required in order to account for the kinetic energy of the unseen recoil, since only recoil protons of momenta greater than approximately 350 MeV/c are imaged by the calorimeter. Note that the correction is applied after the HiRes cuts have been performed.

8. **Momentum correction for ν_μ flavor PCE events:** The momentum of the leaving muon is recalculated on the basis of a multiple-scattering flag (MSFLG)

assigned by visual scanning [40]. An algorithm is used to correct event energies and directions; it uses the observed amount of multiple scattering deflection to assign additional muon track length and therefore additional momentum. The additional track length, in a 1.60 g/cm^3 Soudan medium, is assigned to the exiting muon as follows:

– MSFLG = 1: If the muon track has no discernible multiple-scattering and the visible muon track length in the detector (L_{vis}) is greater than 400 cm, then 300 cm is added. If L_{vis} is less than 400 cm then the smaller of $2 \times L_{vis}$ or 250 cm is added.

– MSFLG = 2: For slight multiple-scattering, the smaller of $2 \times L_{vis}$ or 150 cm is added.

– MSFLG = 3: For some multiple-scattering, the smaller of $2 \times L_{vis}$ or 70 cm is added.

– MSFLG = 4: For obvious multiple-scattering, 20 cm is added.

– MSFLG = 5: For obvious multiple-scattering and when the muon track has its stopping endpoint outside the fiducial volume but fully visible within the calorimeter, no extra length is added.

The added length represent the minimum extra length implied by the scan table observations. Therefore the resulting momentum is almost always underestimated.

9. **Calculation of neutrino production height:** Neutrino path length (L) was calculated for each event using an algorithm for neutrino production height in the atmosphere [58]. The algorithm assigns 25 km as the production height of neutrinos incident from $\cos\theta_z < -0.2$; for other zenith angles it assigns path length based on the average production height of neutrinos for that flavor, energy and zenith angle.

		Gold	Rock	MC
Contained HiRes	ν_μ	114	73	1149
	ν_e	152	69	1070
Contained LoRes	ν_μ	37	48	351
	ν_e	49	145	340
	MP	46	60	217
Partially Contained	ν_μ	53	11	373
	ν_e	5	0	51
NC or ambiguous	–	32	110	171
Event Totals		512	643	3915

Table 3.5: Soudan-2 data and MC event samples after selections and cuts.

3.3.4 Final event sample

The final events classified and selected according to all of the above criteria are shown in Table 3.5. These are the events selected for final analysis. The flavor tagging for the multiprongs in the HiRes sample was found to be reliable, therefore these are included in the contained HiRes category together with the corresponding single track (ν_μ) and single shower (ν_e) events. The contained HiRes category includes the CEV, CVC and VOA events that pass the cuts as well as a small set of multiprongs which are identified as contained in the PCE scan (CEVPCE).

For the contained LoRes category the single track (ν_μ) and single shower (ν_e) events are separated from multiprongs (MP). This category includes only the CEV and CEVPCE categories since CVC and VOA events that do not pass HiRes selections are considered to have large residual background.

Partially contained events, both ν_μ and ν_e, that pass our cuts are in a separate category that combines 2-prong and multiprong topologies. Events, both contained or partially contained, with an ambiguous determination of flavor or deemed to originate from a neutral current interaction, are combined into a fourth category.

Chapter 4

Background Contamination in the Soudan 2 Data

The detector is located underground at a depth of 2100 meters-water-equivalent on level 27 of the Soudan mine in Tower, Minnesota. Consequently it is shielded from the high fluxes of cosmic ray induced particles which occur at the surface. Nevertheless, cosmic ray muons which have incident energies at the surface exceeding 200 GeV do reach the detector, and their occurrences are tagged by the active shield proportional-tube array which surrounds it. Additional non-neutrino background is also to be expected from the interactions of cosmic ray muons in the rock surrounding the cavern in which the detector is located. Such interactions produce a flux of neutrons and energetic photons which may emerge from the rock and impinge upon the Soudan detector. These neutral particles may then interact and create contained events which mimic neutrino interactions. Usually these events are accompanied by charged particles which will be registered by the active shield that surrounds the detector. An event with time-coincident shield hits is placed in a separate "rock event" sample. However, some events will not be accompanied by shield hits, either because none of the accompanying charged particles enters the shield or due to shield inefficiency for detection of a through-going charged particle. For particle detection via a coincident two-layer hit (CTL hit), the shield inefficiency is approximately 5%. This zero-hit background results in the contamination of the data sample and it must be assessed and subtracted from the data for any neutrino analysis.

As mentioned in Sect. 3.1, data events are separated into gold and rock event samples. The definitions for these samples differ depending on the event containment:

1. **For contained events (CEV):**

   The gold data sample contains events which are devoid of any shield hits during the allowed time window. The rock event sample holds events with more than one shield hit registered during the event time window.

2. **For partially contained events (PCE):**

   Gold data PCE events are allowed to have one shield hit correlated in time and space with the outgoing lepton candidate. Rock PCE events either have more than one in-time shield hit associated with the event or else have one or more in-time shield hits that are not aligned spatially with the outgoing lepton candidate.

An interesting set of events is the "silver event" sample; these are data events with only one shield hit and they were reconsidered for inclusion recently [59]. Silver events are a mixture of neutrino events with a random shield hit, stopping muons that pass containment tests, and multiple shield hit events where shield hits are missing due to shield inefficiency. The equivalent "silver MC" sample consists of events with a random shield hit and partially contained events with a MC generated shield hit. Initially, the silver data events were excluded from the analysis, since they had a preponderance of rock background and just a small component of gold due to the accidental association of shield hits. The exclusion of silver MC simulated the rejection of data neutrino events with randomly triggered shield hits. These events were rescanned to determine whether the shield hit was unrelated to the event, and therefore a gold event. This evaluation was based upon the geometrical relationship between the shield hit, the event within the calorimeter, and the amount of intervening detector mass. A total of 45 silver-to-gold data events and 276 silver-to-gold MC events were added to the corresponding gold and MC samples as a result of this re-evaluation.

Background to:	Event Topology	Particle reaction
quasi-elastic ν_e	single shower	$\gamma(N) \rightarrow e^+e^-(N)$
		$n\ N \rightarrow n\ N\ \pi^0$
quasi-elastic ν_μ	single proton	$n\ N \rightarrow n\ p$
	single pion	$n\ N \rightarrow (n,p)\ N\ \pi^\pm$
multiprong	double shower	$n\ N \rightarrow \pi^0 + X$
	2+ showers	$n\ N \rightarrow \pi^0\text{'s} + X$
	multiprong tracks	$n\ N \rightarrow$ (p's, $\pi^\pm$'s, ...)
	multiprong with showers	$n\ N \rightarrow$ (p's, $\pi^\pm$'s, π^0's, ...)

Table 4.1: Background contained event topologies and particle reactions.

4.1 Physics of the background

A portion of the background events in the detector have topologies which are not used for the neutrino oscillation analysis, and these are removed even before doing any background calculations. An important example of such events are single proton tracks. While neutral current elastic reactions can in principle contribute to this topology, the depth distribution of single proton track events in Soudan 2 indicates they are predominantly neutron-induced. This topology is flagged and removed during the scanning phases of the data reduction. It represents approximately 28% of the active-shield tagged sample [46].

The remaining rock background is a bigger concern since it matches the topologies deemed interesting for the analysis; namely single tracks, single showers and multiprongs for the contained sample, as well as 2-prongs and multiprongs for the partially contained events. A summary of the photon and neutron reactions which are the principal sources of the background topologies is given in Table 4.1. For contained event topologies, the single showers incur background from both photon and neutron processes, whereas the single track and multiprong events incur backgrounds from neutron reactions only.

Since contained background events are caused by either a photon or a neutron entering the detector, the events thus produced will have different penetration depth distributions than those of neutrino induced events. Neutrino events, because of their small cross sections, will distribute uniformly throughout the detector volume.

Neutrons and photons, on the other hand, will exhibit a decline of event rate with depth due to the finite absorption or conversion lengths for these particles in the Soudan medium. Photons will convert and create showers at depths characteristic of a radiation length (10-20 cm). Neutrons will travel deeper into the detector, interacting at distances on the order of nuclear interaction lengths (75-100 cm). In a study done by William Leeson [46], the effective penetration depth in Soudan 2 was estimated to be 26 ± 20 cm for photons and 86 ± 13 cm for neutrons, in agreement with the expectation.

For partially contained events, there are two potential sources of background: *i*) downward-stopping muons with energetic end-point decay electrons that are misclassified as upward-going PCEs; *ii*) incoming charged hadrons that are produced in the rock surrounding the detector and which are confused with outward-going PCEs. Stringent cuts, as described in Sect. 3.3.2, have been placed to prevent both incoming hadronic and downward stopping events from contaminating the final partially contained sample; these selections include a prong-hit cut and a vertex depth cut.

4.2 Depth distributions

For each event, the distance between the vertex position as defined by the event reconstruction and the nearest outside face of the detector, excluding the floor, is calculated. This distance is defined as the depth of the event. As indicated previously, the depth distributions may be useful in determining the background contamination of the gold sample. Since rock events tend to occur at higher rates than neutrino events at shallow depths, an initial vertex depth cut is applied to each sample according to their containement: 20 cm for contained events and 40 cm for partially contained events.

4.2.1 Single shower events

The vertex depth distribution for the gold events of the contained single shower sample is shown by the data points with error bars in Fig. 4.1; the neutrino MC is represented by the dashed line histogram and the rock background by the dotted line histogram.

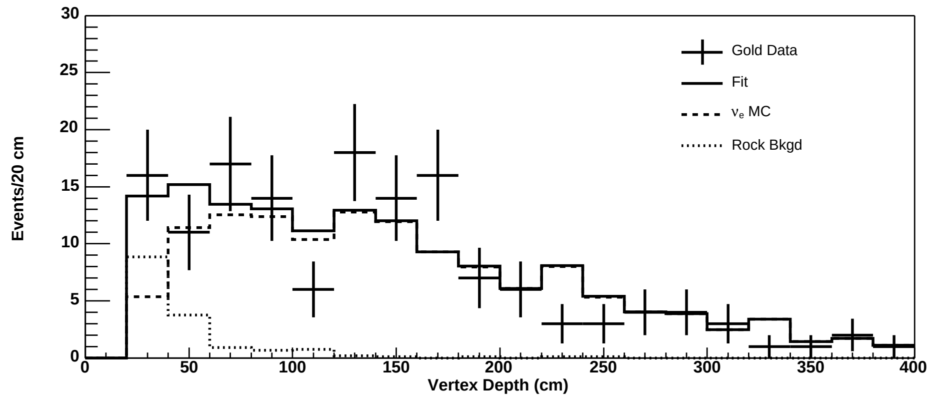

Figure 4.1: Depth distributions for contained single shower events. The gold data distribution (crosses) is shown compared to the best fit (solid histogram) obtained with a combined sum of neutrino MC (dashed) and rock background (dotted) distributions.

The gold data compared to the pure neutrino expectation shows greater discrepancy for shallow depths, *i.e* less than 60 cm. The neutrino MC is lower than the gold data in these bins, whereas the rock background has an important presence in these region. This is consistent with our knowledge that showers are initiated by photons emerging from the cavern walls which have small penetration depths ($\sim$ 20 cm), thus producing a sharp fall in the first few bins. The events at deeper depths in the rock distribution are consistent with a small neutron-induced shower component, with longer penetration depths corresponding to the nuclear absorption lengths in the Soudan medium ($\sim$ 86 cm). Both of these components contribute to the zero-shield hit background in the gold data as seen by the solid line histogram representing a fit of the data to a linear combination of the neutrino MC and the rock background distributions.

4.2.2 Single track events

The vertex depth distribution for single track events with no shield hits is shown in Fig. 4.2 by the data points with error bars. The neutrino MC is represented by the dashed line histogram and the rock background by the dotted line histogram.

The gold data histogram shows a relative excess compared to the neutrino MC

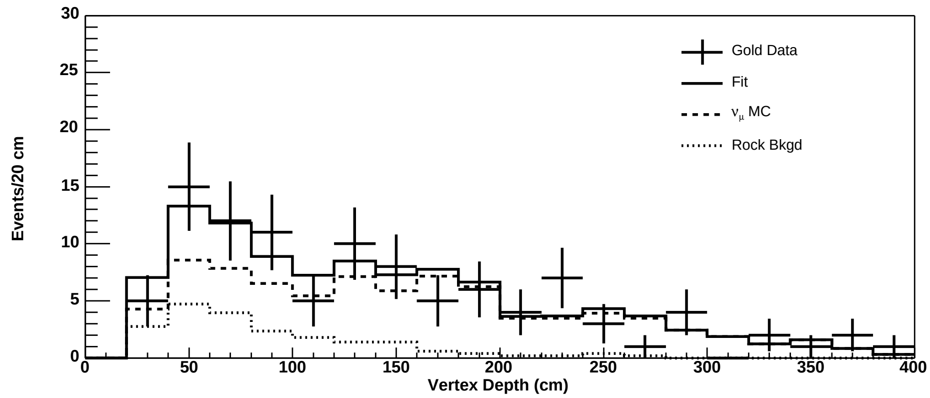

Figure 4.2: Depth distributions for contained single track events. The gold data distribution (crosses) is shown compared to the best fit (solid histogram) obtained with a combined sum of neutrino MC (dashed) and rock background (dotted) distributions.

distribution at depths greater than 40 cm. The rock background for single tracks extends to deeper depths than the single shower background. This is indicative of deeper penetration depths for this type of background, consistent with a pure neutron component. The first non-zero bin is notably lower than the subsequent bins due to containment effects.

4.2.3 Multiprong events

The vertex depth distribution for the gold multiprong events is shown in Fig. 4.3 by the data points with error bars. The neutrino MC is represented by the dashed line histogram and the rock background by the dotted line histogram.

The gold distribution shows a discrepancy compared to the neutrino MC up to 160 cm in depth, and the rock background extends to similar depths. As is the case for single track events, we conclude also for multiprongs that backgrounds are characterized by the longer interaction lengths of neutrons.

4.2.4 Partially contained events

The vertex depth distribution for the gold partially contained events is shown in Fig. 4.4 by the data points with error bars. The neutrino MC is represented by the

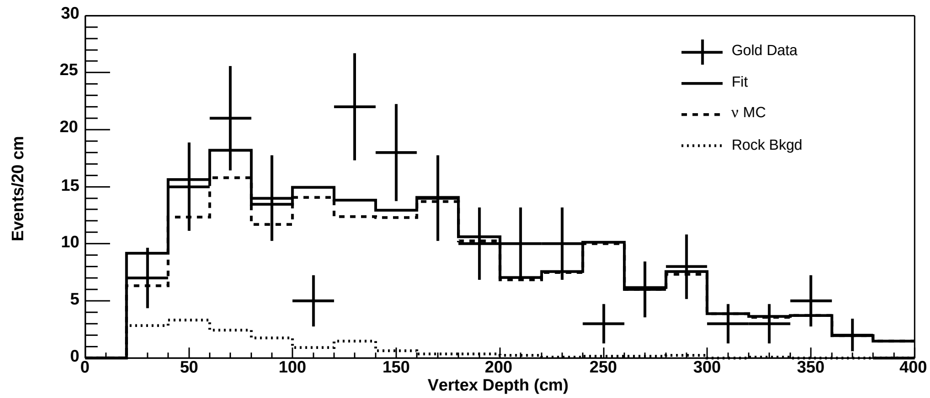

Figure 4.3: Depth distributions for contained multiprong events. Gold data, neutrino Monte Carlo and rock background distributions are shown together with the best fit of neutrino MC plus rock to the gold data.

dashed line histogram and the rock background by the dotted line histogram.

The rock background is minimal and only appears at shallow depths, namely below 80 cm. This is due to the stringent cuts already applied to the PCE events in order to eliminate background. The data and pure neutrino MC are seen to be in good agreement.

4.3 Depth fitting

Since the gold sample is a combination of genuine neutrino interactions together with some zero-shield-hit rock background, and given that the vertex depth distributions can serve as independent discriminators, we use these distributions to determine the amount of rock present in the gold sample. The underlying assumption here is that the shield multi-hit rock and the shield zero-hit rock background behave identically with respect to depth. That this is a reasonable assumption follows from our discussion about the origins of the contamination. Thus, we fit the depth distributions of the gold sample to those of the neutrino Monte Carlo and the rock background using an extended maximum likelihood fit.

Early studies [17, 60] of the background using depth were completed for each event category separately. The problem with this method is that some of the categories have

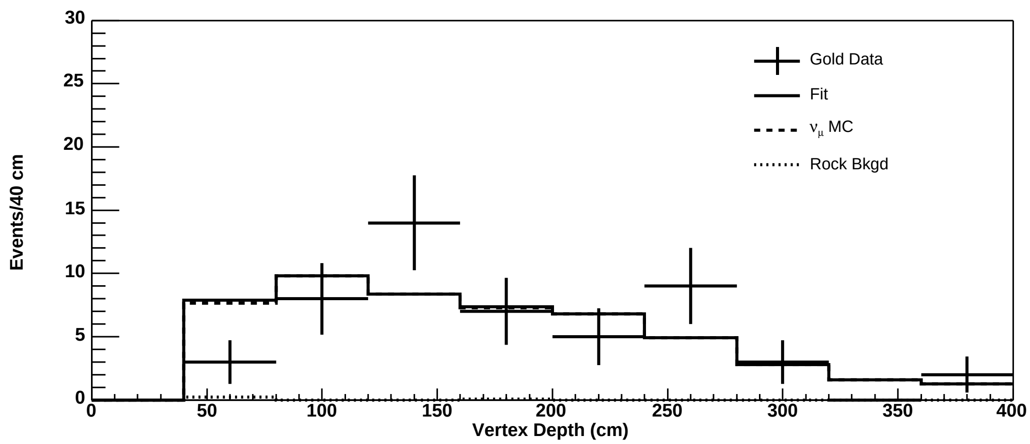

Figure 4.4: Depth distribution for partially contained events. Gold data, neutrino Monte Carlo and rock background distributions are shown together with the best fit of neutrino MC plus rock to the gold data.

very low statistical samples, particularly for gold and rock. In some of these studies, events were further separated by HiRes and LoRes selections; however this resulted in even lower statistics for an already statistically challenged sample. In a more recent study [48], a method was proposed to overcome this problem by combining rock categories of the same origin, either neutron or neutron plus gamma, while keeping the gold data and the neutrino MC events in the same topology categories as used for the depth distributions shown in this Chapter. Thus we carry out our background fits as follows:

- We fit the gold single shower depth distribution to the single shower MC distribution and the neutron plus gamma rock depth distribution which is composed of single showers.

- We fit the gold single track depth distribution to the single track MC distribution and the neutron rock depth distribution which is composed of the single track and multiprong samples.

- We fit the gold multiprong depth distribution to the multiprong MC distribution and the neutron rock depth distribution which is composed of the single track

Event Topology	f factor	b factor
single shower	0.105 ± 0.038	0.082 ± 0.029
single track	0.199 ± 0.124	0.197 ± 0.123
multiprong	0.084 ± 0.074	0.069 ± 0.061
PCE	0.005 ± 0.017	0.025 ± 0.085

Table 4.2: Background fractions and b factors for contained and partially contained events.

and multiprong samples.

As explained in Sect. 3.3.1 a 300 MeV/c momentum cut is applied to the LoRes sample in order to reduce the high levels of rock background present. The results from these fits are shown in Table 4.2. The fits return the fraction of gold which is background (f) for each of the event samples.

A different factor of interest is the background factor (b), which corresponds to the fraction of rock in the gold sample; $b = fG/R$ where G and R are the Gold and Rock total numbers for the selected sample. This factor is needed when subtracting any rock distribution from the corresponding gold distribution.

For purposes of fitting all Soudan 2 data to determine neutrino oscillation parameters, it is expedient to combine certain event samples in order to maximize statistics and sensitivity. This requires combining of event samples into different categories than those used in the background fits. In order to obtain an averaged b for each fitting category we use a weighted average:

$$b = \sum_i \frac{b_i R_i}{R} ,$$

where the error is given by:

$$\Delta b = \sqrt{\sum_i \left(\frac{R_i \Delta b_i}{R} \right)^2} .$$

The results of these calculations are presented in Table 4.3.

We find that the above-mentioned combination of categories for carrying out the depth fits results in significant improvement of background estimation for the neutrino analysis. However certain systematic errors are introduced. For example, we assume

		b factor
Contained HiRes	ν_μ	0.166 ± 0.094
	ν_e	0.077 ± 0.030
Contained LoRes	ν_μ	0.197 ± 0.123
	ν_e	0.082 ± 0.029
	MP	0.069 ± 0.061
Partially Contained	ν_μ	0.025 ± 0.085
	ν_e	–
NC or ambiguous	–	0.069 ± 0.061

Table 4.3: Fraction of rock in the gold event samples used for analysis.

that the mixture of neutron and gamma-induced rock is the same for the HiRes and LoRes shower sample, which might not be the case. Similarly, for tracks we are assuming that there is negligible difference between the depth distributions for HiRes and LoRes, even though the neutrons may have different energy distributions. These assumptions are reasonable since it is known that neutron and gamma cross sections vary little over our energy range. It is likely that these systematic effects are much smaller than the statistical errors involved.

4.4 Other background studies

An independent background determination was done using a multivariate discriminant analysis [61, 62]. There are several advantages to this method: the use of all information available, the maximization of the statistics since no cuts are made on the variables, and an automatic accounting of correlations among the variables. This analysis employed four different physical quantities to separate background from neutrino events in the gold data:

Depth: As stated previously, this variable is defined to be the perpendicular distance of the vertex position for the event to the nearest outside face of the detector, excluding the floor. As discussed in Sect. 4.2, neutrino events distribute nearly uniformly (aside from event containment restrictions) throughout the detector medium whereas the vertex depths of rock backgrounds tend to peak at shallow depths.

Inwardness: This variable is the cosine of the angle between the event momentum and the perpendicular to the nearest outside face of the detector. Inwardness distributions tend to be more uniform for neutrino events in comparison to rock events for which inwardness is almost always of positive values. Rock events favor angles smaller than 90 degrees ($\cos\theta_I > 0$) due to the short path length of neutrons and gammas in the detector.

Visible energy: This the total reconstructed energy of all visible prongs of the event. Rock events appear to be mostly of lower energies, neutrino events cover a wider range.

Zenith angle cosine: We take the cosine of the angle between the event momentum and the zenith line. Rock events peak in the downward direction ($\cos\theta_z > 0$) whereas neutrinos are distributed more uniformly. However ν_μ-flavor neutrinos can be expected to favor downward-going zenith angles as a result of neutrino oscillations.

The first quantities, depth and inwardness, are not affected by neutrino oscillations, whereas visible energy and zenith angle are affected by them. It was originally suggested that it would be better to use variables independent of the physics that we are trying to study. However, as was pointed out in Ref. [61], it is possible to study the results for the different physics scenarios, no oscillations or oscillations for different values of the parameters. As before, the method assumes that the zero-shield hit background in the gold data has the same distribution in the four variables as does the rock background. The gold data is fitted to the neutrino Monte Carlo and the rock distributions separately for each category.

The results obtained for single showers and multiprong ν_e were compatible with the ones from the depth-only fits. Unfortunately the error estimates do not improve since this method does not take advantage of combining the rock distributions of different categories. A multivariate fit for single tracks and multiprong ν_μ needs to take into account neutrino oscillations since two of the quantities used are affected by the phenomenon. Thus a fit was done for each pair of values of $\sin^2 2\theta$ and Δm^2 by oscillating the MC each time. The fit indicates somewhat less background in this sample than in the depth fit and a variation of the values for different oscillations parameter pairs. The results are consistent within the errors and there is no improvement in the errors with respect to the depth-only fits.

Chapter 5

Evidence of oscillations in atmospheric neutrinos

The fluxes of ν_μ, $\overline{\nu}_\mu$, ν_e, and $\overline{\nu}_e$ neutrinos arriving at the Earth's surface originate from cosmic ray interactions in the upper atmosphere. The atmosphere is being constantly bombarded with cosmic ray particles; the primary cosmic ray flux consists mostly of protons but also includes nuclei of light and medium-heavy elements as well as electrons. The interactions of these particles with nuclei of air molecules create cascades of hadronic particles. Within the hadronic cascades are pions and kaons; their in-flight decays yield secondary muons. The decays of all these particles lead to the atmospheric neutrino flux detected on Earth by underground experiments such as Soudan 2. The fluxes of muon and electron neutrinos have been studied extensively and detailed calculations have been carried out [63, 64, 65, 66, 67]. A detailed interpretation of our data requires comparison to a reliable calculation of the expected atmospheric neutrino flux. In the next section we describe the calculated atmospheric neutrino flux expectation (assuming null neutrino oscillations) as it relates to our data. For a detailed review on atmospheric neutrino flux models see Ref. [68]; we have used several figures from this reference in the next Section.

5.1 Atmospheric neutrino prediction

There are several calculations for the atmospheric neutrino flux available. The key ingredients for these calculations are models of the primary cosmic ray flux, estimates for geomagnetic effects, and modeling of the interactions of the cosmic rays in the air including interactions and decays of the secondary particles.

In the last decade, the primary cosmic ray flux has been well measured at low energies ($E_{cr} < 100$ GeV) using balloon-borne magnetic spectrometers and by the AMS Space Shuttle flight. Our knowledge of the spectrum at higher energies is less precise because the ballon-borne calorimeters used for this purpose do not capture all the energy of the primary, and the energy determination is not as precise as with spectrometers. The cosmic ray flux in the energy range which yields our contained neutrino interactions is composed of 75% H, 17% He, and of heavier elements. Fig 5.1 shows the observed flux of cosmic-ray protons and helium, note the larger errors at higher energies.

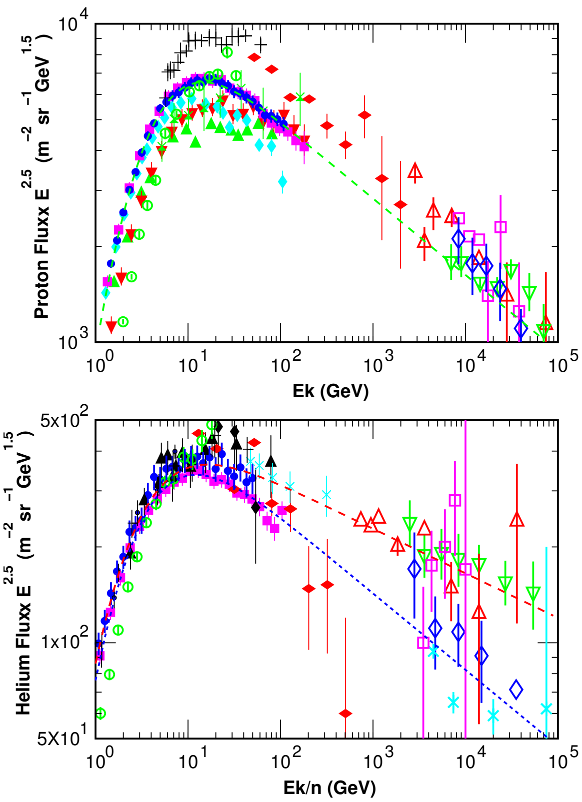

Figure 5.1: Observed flux of cosmic-ray protons and helium. The dashed lines show fits to the data which provide parametrizations for atmospheric neutrino models. For the cosmic-ray proton data, the crosses belong to an earlier measurement which had previously been the standard but newer measurements have been consistently lower.

At low energies the effects of solar activity on the primary flux are quite pronounced, resulting in a modulation of the solar activity which varies with an 11 year period. During periods of high solar activity the low-energy portion of the primary cosmic flux becomes diminished due to the increased density of scattering particles and fields which comprise the solar wind. This reduction at high geomagnetic latitude sites such as Soudan for 10 GeV protons is estimated to be about 20% whereas at 1 GeV it can vary up to a factor of 2 between the solar minimum and maximum. The effect must be considered by atmospheric neutrino flux models. These fluxes are usually calculated just for solar min and solar max which is when the majority of the low energy cosmic ray measurements are made, and so it is necessary to interpolate between these calculations. This is accomplished by using neutron monitor data to determine the solar cycle activity, and normalizing neutrino rates to this activity assuming a linear relation between the two fluxes. Current flux weights for Soudan 2 use monthly data from the the CLIMAX neutron monitor (located in Colorado, USA) shown in Fig. 5.2.

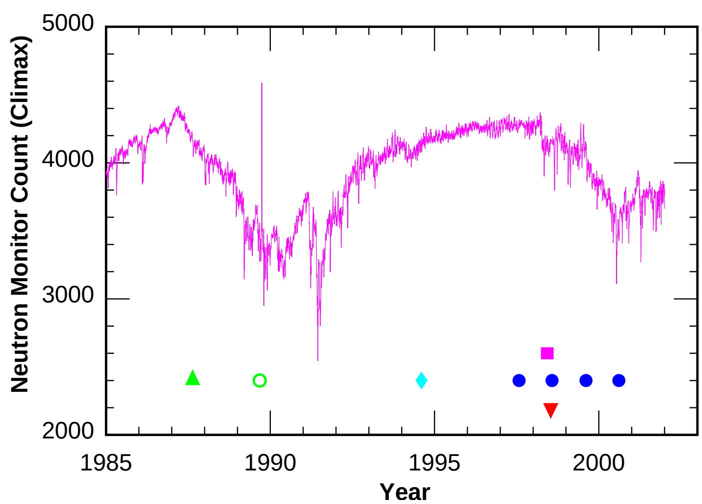

Figure 5.2: Record of count rates for the Climax neutron monitor [69]. Times of various balloon flights are marked using the same symbols as in Fig. 5.1.

The cosmic ray particles incident upon the upper atmosphere are positively charged and the Earth's magnetic field deflects them significantly at low energies. The primary cosmic ray flux is nearly isotropic, except for these geomagnetic effects. The geomagnetic field acts upon cosmic rays before and after entering the atmosphere. Before entering, the field behaves as a deflector that allows only particles with sufficiently high rigidity (total momentum divided by charge) to penetrate the Earth's magnetic field. After the interaction of the cosmic rays in the atmosphere, the resulting charged particles are bent by the field.

The minimum rigidity, or "cutoff rigidity", is a function of the entering position on the Earth and of the arrival direction. It is calculated as the minimum rigidity with which a test particle leaving the surface of the Earth can escape form the magnetic field. A particle arriving from the east has a higher cutoff than one arriving from the west. Thus a higher cosmic ray flux is expected from the west than from the east. At low geomagnetic latitudes (*ie*. Kamioka site) there is a higher local cutoff compared to the cutoff rigidity averaged over the Earth. The effect is reversed for a detector located near the geomagnetic pole as the in the case of Soudan 2. In addition, a site at low geomagnetic latitude presents a strong azimuthal asymmetry, with the cutoff higher for particle arriving from the east than from the west, while such effect is washed out at higher geomagnetic latitudes. These effects for the different locations on Earth have been incorporated in the atmospheric neutrino calculations.

The interactions of cosmic ray nuclei in the atmosphere create pions and kaons which then decay producing neutrinos. The fraction of kaons to pions varies over the full energy range and some assumptions about their relative importance have to be made. Early calculations parametrized the pion production spectrum in the atmosphere to fit an observed flux of muons. In this way the primary spectrum and the particle production did not enter the calculation of the neutrino flux explicitly. More recent calculations use detailed Monte Carlo simulations starting from the measured cosmic ray flux.

The fundamental source of uncertainty in the neutrino yield for each cosmic ray interaction comes from the treatment of particle production in the individual collisions that make up the atmospheric cascades. The models of hadron production in use for calculations of the atmospheric neutrino flux are based on accelerator data for protons on light nuclei, for which the coverage of phase space generally does not match fully the atmospheric neutrino range. There are several models available. Fig 5.3 from

Ref. [68] shows the changes in the atmospheric flux predictions due solely to the differences in the treatment of the hadronic interactions. The flux calculations used for Soudan are based on Target 1.0 and FLUKA. The larger difference among the calculations at the Soudan site are the result of differences in the treatment of the low-energy interactions which are more important at Soudan than at Kamioka because of the higher geomagnetic cutoff at the latter site.

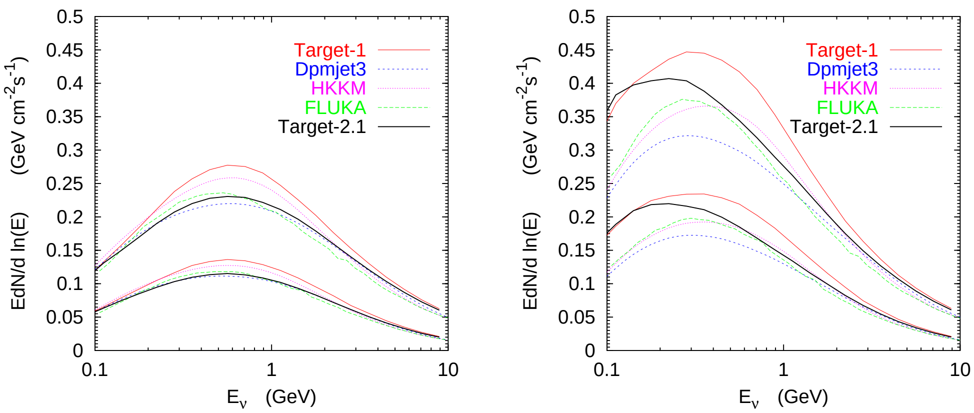

Figure 5.3: Angle-integrated neutrino fluxes ($\nu + \bar{\nu}/3$) at Kamioka (left) and Soudan (right) with several interaction models: HKKM [64], DPMJETt3 [70], FLUKA [67], TARGET 1.0 [63] and TARGET 2.1 [71]. The upper set of curves is for muon neutrinos and the lower set for electron neutrinos.

The most widely used independent flux calculations used for the interpretation of measurements of atmospheric neutrinos are one-dimensional where all decays are assumed to take place along the primary cosmic ray direction. The net effect of this approximation is to overestimate the number of low energy (less than 100 MeV) neutrinos. The neutrinos come primarily from the two-body decay modes of the pions and kaons and the subsequent muon decays. The decay chain for pions is:

$$\pi^{\pm} \to \mu^{\pm} + \nu_{\mu}(\overline{\nu}_{\mu}) \tag{5.1}$$

and the decay chain for the resulting muon is:

$$\mu^{\pm} \to e^{\pm} + \nu_{e}(\overline{\nu}_{e}) + \overline{\nu}_{\mu}(\nu_{\mu}), \tag{5.2}$$

with a similar chain for charged kaons. For conditions where all particles decay, we expect:

$$\frac{\nu_e + \bar{\nu}_e}{\nu_\mu + \bar{\nu}_\mu} \sim 1/2, \tag{5.3}$$
$$\nu_\mu/\bar{\nu}_\mu \sim 1 \qquad \text{and} \qquad \nu_e/\overline{\nu}_e \sim \mu^+/\mu^- .$$

The kinematics of the π and μ decays are such that the energy carried on average by each neutrino in the chain is roughly equal. Most mesons below 10 GeV decay before interacting, but the interaction probability grows significantly above 100 GeV. The result is that the ratio in Eq. 5.3 varies as a function of energy and for energies around 1 GeV, it is fairly different among the several flux calculations. The calculations agree in predicting the ratio to be slightly below 1/2 for energies from 100 MeV to few GeV as seen in Fig. 5.4.

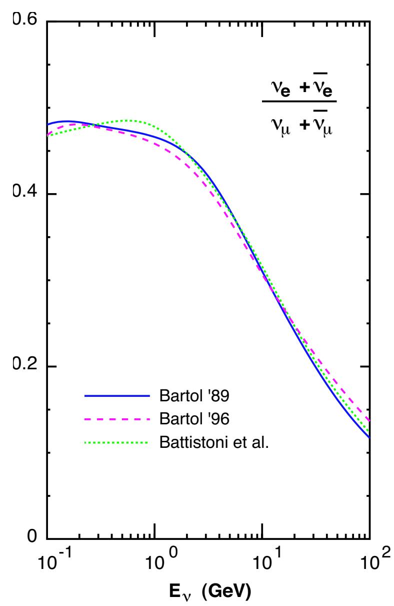

Figure 5.4: Ratio of $(\nu_e + \bar{\nu}_e)/(\nu_\mu + \bar{\nu}_\mu)$ as a function of neutrino energy for different calculations of the flux. The original flux calculation used in Soudan 2 (Bartol '89) is the solid line, the revised Bartol flux (Bartol '96) and the new 3D flux calculation done by the Battistoni group are represented by the dashed and dotted lines.

Convolution of the measured cosmic ray spectrum with the geomagnetic rigidity cutoff and the neutrino yields produces the neutrino spectrum as a function of energy and zenith angle. The different models produce significantly different predictions for the total neutrino rate, however they agree to within 5% on the ν_μ to ν_e ratio. The estimated systematic uncertainty in the absolute neutrino event rate is 20%.

Fig. 5.5 shows the distribution of neutrino energies that give rise to the three different classes of events used in the Soudan 2 analysis. The contained samples peak at 500 MeV for LoRes events and 1 GeV for HiRes events. The distributions are broad and substantially overlap. Probing the atmospheric neutrino flux at higher energies ($E_\nu \sim 5$ GeV) is the partially contained event sample distribution. Upward-stopping muons are not used in the current analysis; their distribution would peak at an energy modestly above the peak for Partially Contained events.

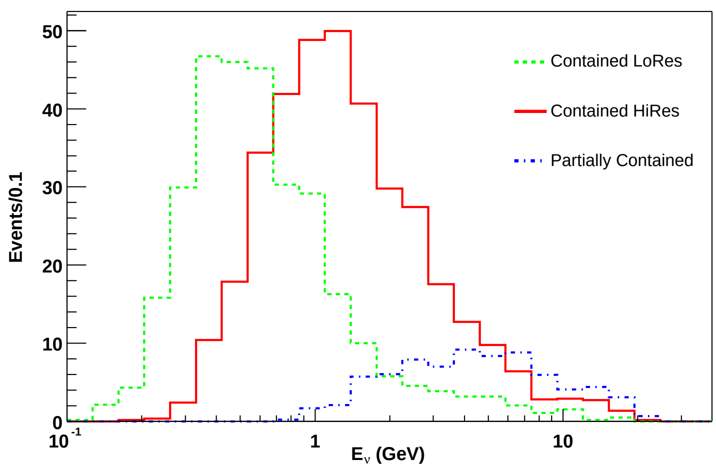

Figure 5.5: Distributions of neutrino energies in bins of $\Delta \log(E_\nu)$ for three classes of events at Soudan 2 used in the current analysis. The distributions peak at 500 MeV, 1 GeV and 5 GeV. They have been scaled using 1/6.09 to match the detector exposure.

The atmospheric neutrino flux used in the Soudan 2 Monte Carlo was based on the BGS flux, also know as Bartol '89 [34]. Modifications of the neutrino flux were accommodated by weighting the generated events. The Bartol group later updated their flux calculation. The newer version, Bartol '96 [63], was incorporated into the Soudan MC with a set of extra weights. The improvements over the previous calculation included an updated version of the model for hadronic interactions (from TARGET to TARGET+). It also extended the calculation beyond the original 3 GeV energy limit for the neutrinos or equivalently 1 TeV for the primary flux. The TARGET model is based on a parametrization of particle interactions on targets of different mass. The main change in the new version concerned kaon production at high energies. The new Bartol calculation also improved upon approximations used originally for the geomagnetic effects. The overall uncertainty in the flux remained 21%.

Calculation	Primary Flux	Geomagnetic Effects	Model Atmosphere	Hadronic Model
Bartol '89	Bartol	Offset dipole	1-dimensional	TARGET
Bartol '96	Bartol+	$\bar{p}$ backtracking Intl. Geomagnetic Ref. Field	1-dimensional	TARGET+
Battistoni	Bartol+	$\bar{p}$ backtracking magnetic field expansion	3-dimensional	FLUKA

Table 5.1: Comparison of atmospheric neutrino flux calculations.

The Bartol group predictions are based on a one-dimensional model, where all decays are assumed to take place along the primary particle direction. More recently, a three-dimensional calculation made by Battistoni et al. [67] has been made available. As with Bartol '96, a set of extra weights was generated for the Soudan MC. The flux calculation uses the same primary spectrum and composition as the Bartol group used in their most recent calculation, however they differ in the 3D modeling of the interactions, in the hadronic interaction model used and in the treatment of geomagnetic effects. Table 5.1 indicates the main differences among the three flux calculations available in the Soudan MC. The hadronic model used in the Battistoni flux is known as FLUKA. It uses a more sophisticated microscopic model of particle production with intranuclear cascading and its results for pion production are different than those from TARGET. A comparison of the three fluxes (Bartol '89, Bartol '96 and Battistoni et al.) without any geomagnetic field and the same primary spectrum is shown in Fig 5.6 from Ref. [72]. Observe the overall lower normalization of the 3D flux for any neutrino flavor chosen.

The zenith angle distribution for Bartol '89, Bartol '96 and Battistoni shown in Fig. 5.7 highlight the differences among the three flux predictions. The Bartol '89 calculation used originally for the Soudan MC had coarse binning and was essentially flat at the horizon for low energies (Fig. 5.7a). The more recent Bartol calculation

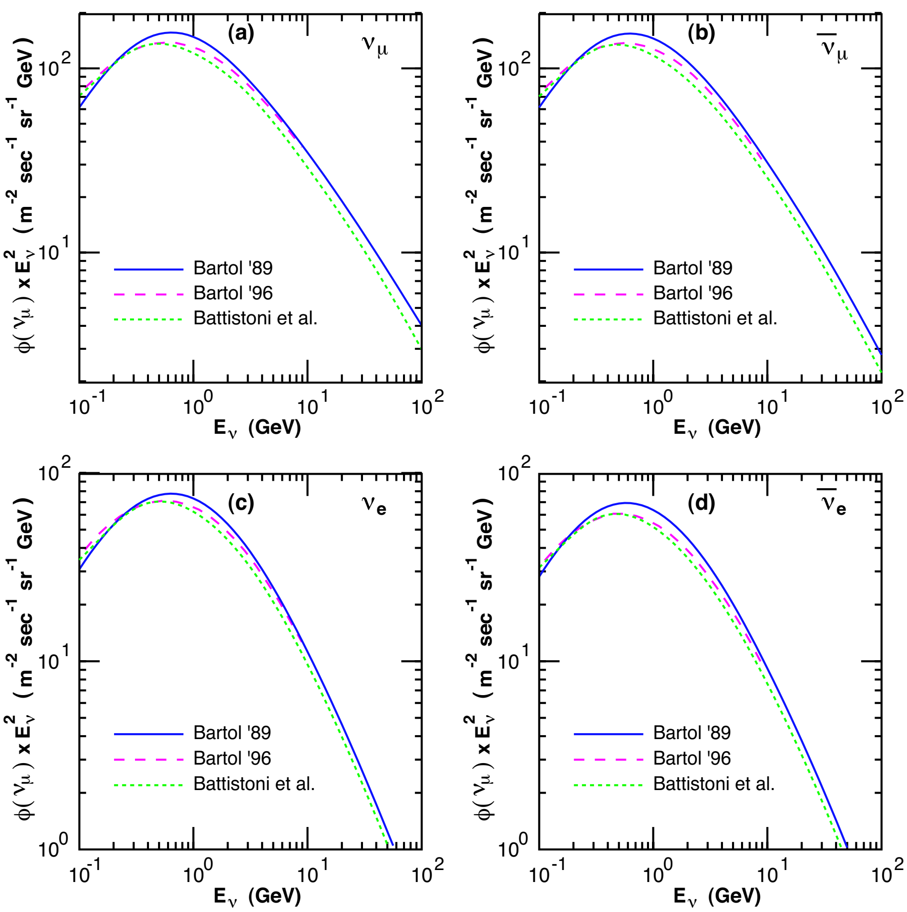

Figure 5.6: Comparison of the energy distributions for three neutrino flux calculations. The original flux calculation used in Soudan 2 (Bartol '89) is the solid line, the revised Bartol flux (Bartol '96) and the new 3D flux calculation done by the Battistoni group are represented by the dashed and dotted lines.

was provided as a continuous function and has a small dip at the horizon, except at higher energies (Fig. 5.7d). This calculation presents a slightly lower rate than the original Bartol. The Battistoni 3D calculation has a characteristic peak near the horizon for lower energies and its overall rate is lower than the Bartol '96 calculation.

The enhancement of the neutrino flux, near the horizon for sub-GeV energies, in the three-dimensional calculation is a geometrical effect not present in the one-

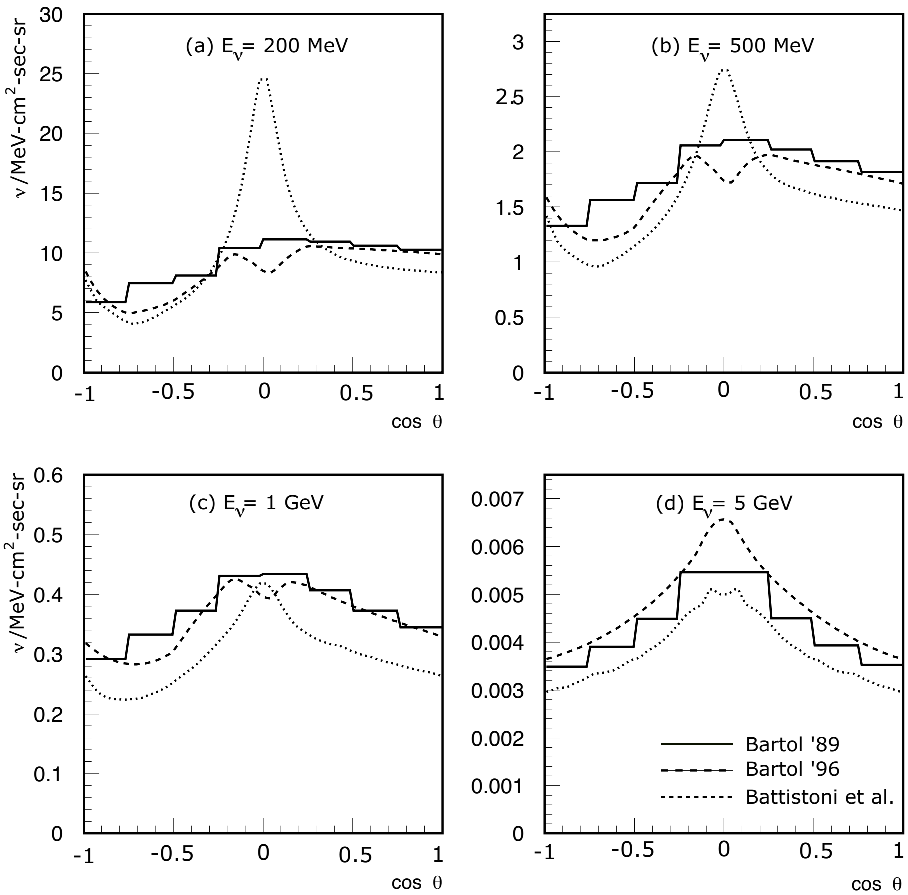

Figure 5.7: Comparison of zenith angle distributions for different neutrino flux calculations in four energy bins. The original flux calculation used in Soudan 2 (Bartol '89) is the solid line histogram, the revised Bartol flux (Bartol '96) and the new 3D flux calculation done by the Battistoni group are represented by the dashed and dotted lines.

dimensional calculations. Unfortunately, the horizontal enhancement of the neutrino flux appears mainly at low energy where the resolution for reconstruction of the incident neutrino direction is worse, making it impossible to detect with our experiment. It is important to note that the 3D calculation is not considered final by the authors, since it does not include yet the effects of the local geomagnetic field in the transport of charged particles in the atmospheric shower development. There have been suggestions that such effect could be relevant.

		Data (bkgd subt'ed)	bkgd	MC (weighted)
Contained HiRes	ν_μ-like	101.9 ± 12.7	12.1 ± 6.9	1115.1
	ν_e-like	146.7 ± 12.5	5.3 ± 2.1	1047.4
Contained LoRes	ν_μ-like	49.5 ± 9.9	11.5 ± 6.2	457.5
	ν_e-like	57.0 ± 9.6	14.0 ± 4.6	402.5
Partially Contained	ν_μ-like	52.7 ± 7.3	0.3 ± 0.9	384.3
	ν_e-like	5.0 ± 2.2	0.0 ± 0.1	51.5
NC+ambiguous	ν_μ-like	24.4 ± 8.8	7.6 ± 6.7	165.7
Total		437.2	50.8	3624.0

Table 5.2: Populations in all samples separated in ν_μ-like and ν_e-like events using the 300 MeV/c momentum cut. The data has been background subtracted and the Monte Carlo has been weighted using the Bartol '96 flux calculation.

5.2 Ratio of ratios

The atmospheric neutrino flavor ratio or ratio of ratios,

$$R_\nu = \frac{[(\nu_\mu + \bar{\nu}_\mu)/(\nu_e + \bar{\nu}_e)]_{Data}}{[(\nu_\mu + \bar{\nu}_\mu)/(\nu_e + \bar{\nu}_e)]_{MC}}\,, \tag{5.4}$$

has been used to measure the deviation from the prediction of the neutrino flux at several underground experiments including Soudan 2 [17]. The ν_μ/ν_e ratio is known to be near 2 for energies around 1 GeV and has a well predicted spectrum. The comparison of this ratio for the data to the Monte Carlo prediction provides a reliable measurement of the excess or deficit in the neutrino count independently of uncertainties in estimating the ν_μ and ν_e spectra separately.

In Soudan 2 the neutrino flavor is assigned as described in Sect. 3.2.4 where single tracks and multiprongs with leading tracks are tagged as being of ν_μ-like flavor and single showers and multiprongs with leading showers of ν_e-like flavor. In Table 5.2 we show the resulting number of events for each category. The totals in the data column of this table are the result of subtracting the background calculated using the procedure described in Sect. 4.3 from the gold sample shown in Table 3.5. The Monte Carlo events have been weighted using the Bartol '96 atmospheric neutrino flux calculation.

For the ratio of ratios we use all non-ambiguous flavor contained events shown in

Flavor Assigned	MC Truth ν_μ	ν_e	NC
μ	1396.8	59.0	116.8
e	41.0	1311.9	98.0
"NC"	50.8	40.5	45.5

Table 5.3: Flavor identification matrix for "blind" flavor tagging of neutrino MC events after 300 MeV/c momentum cut. The columns are the true flavor for the event and the rows the flavor assigned during reconstruction.

Table 5.2 and obtain a raw ratio of ratios, R, defined as:

$$R = \frac{[\nu_\mu\text{-like}/\nu_e\text{-like}]_{Data}}{[\nu_\mu\text{-like}/\nu_e\text{-like}]_{MC}} \tag{5.5}$$

$$= 0.69 \pm 0.10(stat) \pm 0.06(sys) \tag{5.6}$$

The deviation of R from the expected value of 1.0 is the first indication of a ν_μ deficit in the atmospheric neutrino flux. Note that for the data the number of ν_μ-like events is lower than the number of ν_e-like events whereas the reverse is expected, as seen in the Monte Carlo. This result is consistent with the previously published result by the Soudan 2 Collaboration: $R = 0.64 \pm 0.11(stat)^{+0.06}_{-0.05}(sys)$ [17] which used two thirds of the final exposure and did not contain the multiprong sample. The systematic error quoted is an estimate due to the uncertainties on the expected flavor ratio, the Monte Carlo, the scanning procedure and the background subtraction assumptions [17].

The ratio of ratios in Eq. 5.5 is based on the measured ν_μ/ν_e ratio or more precisely ν_μ-like/ν_e-like. The fraction of ν_μ remaining after oscillations, R_μ, and the normalization a relative to Bartol '96 prediction, can be determined using the flavor identification matrix for this sample of events shown in Table 5.3 [73]. If we assume that only muon neutrinos oscillate and that electron neutrinos are not different than the expectation, R_μ is equivalent to R_ν, namely the ratio of ratios corrected for mis-identification.

The number of ν_μ-like and ν_e-like events are given by

$$[\nu_\mu\text{-like}]_{Data} = a(R_\mu T_\mu + T_e + T_{nc})[\nu_\mu\text{-like}]_{MC} \tag{5.7}$$

$$[\nu_e\text{-like}]_{Data} = a(R_\mu S_\mu + S_e + S_{nc})[\nu_e\text{-like}]_{MC} \tag{5.8}$$

where T_μ, T_e and T_{nc} are the probabilities for ν_μ-like events to be true ν_μ, ν_e, or NC

Sample	R	R_ν	a	% Bartol
CEV trk/shw	0.54 ± 0.12	0.51 ± 0.13	0.145 ± 0.016	90%
CEV	0.69 ± 0.10	0.64 ± 0.11	0.142 ± 0.012	87%
CEV+PCE	0.75 ± 0.10	0.72 ± 0.10	0.140 ± 0.012	86%

Table 5.4: Ratio of ratios and normalization for different event samples. The rows are shown in increasing average energy per sample.

as obtained from the identification matrix and S_μ, S_e and S_{nc} are those probabilities for ν_e-like events. Solving the two equations for R_μ and using Eq. 5.5, we obtain a relation between R_μ and R:

$$R_\mu = \frac{(1 - S_\mu)R - 1 + T_\mu}{T_\mu - S_\mu R} \tag{5.9}$$

which for the contained sample yields

$$R_\mu = 0.64 \pm 0.11 \pm 0.06 \tag{5.10}$$

and gives a corresponding normalization value of $a = 0.145 \pm 0.016$, 87% of the Bartol '96 flux.

In Table 5.4 we show the raw ratio of ratios, the fraction of ν_μ remaining after oscillations and the normalization for three different combinations of data samples: (i) contained single track and single showers, (ii) contained track, shower and multiprongs and (iii) contained and partially contained sample. The first sample is equivalent to the sample used in the ratio of ratios original publication [17] and has a lower average energy than the other two samples as seen in Figure 5.8. The second result is the one obtained above for all contained events. The final sample adds the partially contained events. It can be seen that the values of R and R_μ increase with increasing average energy of the sample, as expected if the deviation from 1.0 is due to oscillations.

5.3 Angular distributions

The comparison of the angular distributions for the data to the unoscillated Monte Carlo prediction provides insight into the oscillation trend present in the data. The

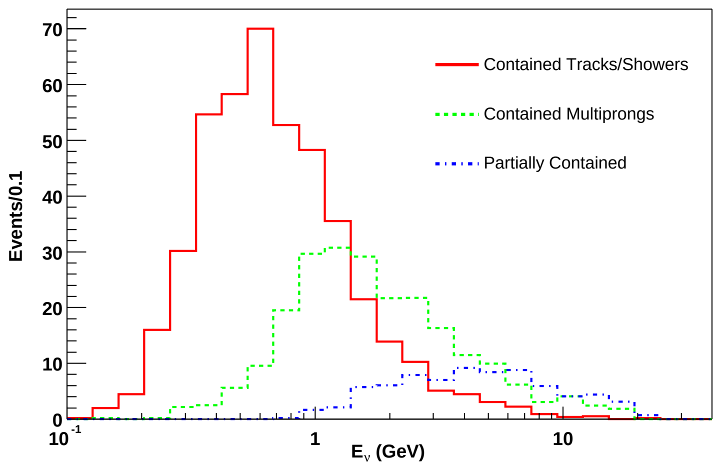

Figure 5.8: Distributions of neutrino energies in bins of $\Delta \log(E_\nu)$ for three classes of events at Soudan 2 used in the current analysis. They have been scaled using 1/6.09 to match the detector exposure.

atmospheric neutrino flux at Soudan 2 is isotropic in its azimuthal distribution since the East-West effect is muted at northern geomagnetic latitudes. No distortion is expected due to neutrino oscillations since the distance of neutrino travel is constant as a function of azimuth. In contrast, neutrino path length varies as a function of the zenith angle, therefore if oscillations are present we expect to see an effect in the data distribution. To study the azimuthal and zenith angle distributions we use the contained HiRes and the ν_μ partially contained samples. The MC null oscillation reference distributions are normalized to the absolute rate of the Bartol '96 atmospheric neutrino flux. To convert these reference distribution into simulated neutrino oscillated MC distributions, we apply to every MC event an L/E-dependent weight representing the probability of ν_μ flavor survival for a given Δm^2 and $\sin^2 2\theta$.

The azimuthal distributions at Soudan 2 are found to be isotropic in agreement with the expectation and they are shown in Fig. 5.9 for the ν_e and ν_μ samples. The ν_e distribution shows no deviation within statistics from the Monte Carlo distribution, albeit $\sim 10\%$ lower than the non-oscillation prediction. The ν_μ flux is uniformly depleted in azimuth relative to the null oscillation expectation and is compared to a histogram weighted by the best fit oscillation parameters and fitted normalization

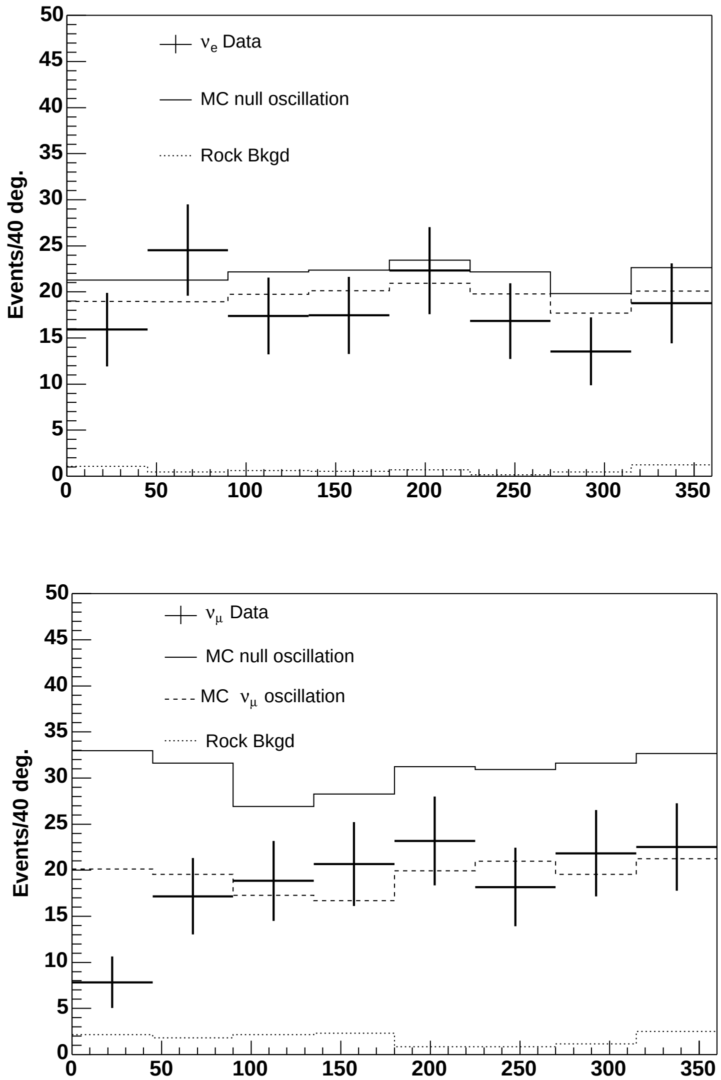

Figure 5.9: Azimuth distributions for ν_e flavor (top) and ν_μ flavor (bottom) samples. The points with errors bars are the data, the solid histogram is the unoscillated Monte Carlo prediction, the dashed histogram is the MC weighted by the best fit oscillation parameters and the fitted normalization, the dotted histogram is the rock background contribution subtracted from the data.

(89% of the absolute rate of the Bartol '96 flux) from the analysis presented in Chap. 6. The ν_μ Monte Carlo events are oscillated using their true identification, similarly a small portion of mis-identified ν_e's are also oscillated giving a slightly lower ν_e prediction. Furthermore, the normalization of the predicted flux has to be lowered by 10% to fit both the ν_e and ν_μ samples.

The distributions in cosine of zenith angle are shown in Figure. 5.10 for the ν_e and ν_μ samples. For ν_e events, the shape of the distribution for the data coincides with that predicted by the Monte Carlo for null oscillations allowing for the scaling down by 10% in the normalization. In contrast, the distribution of ν_μ falls below the MC prediction in all bins with a greater depletion for neutrinos incident from below the horizon (*i.e.* negative zenith angle). The data distribution is consistent with the oscillated MC distribution using the best fit parameters and the fitted normalization as in the case of the azimuthal distributions. The greater depletion at negative $\cos(\theta_z)$ for ν_μ implies a deficit in neutrinos traveling larger path lengths, a signature of neutrino oscillations.

5.4 L/E Distributions

The neutrino oscillation probability, from Eq. 1.13, may be optimally analyzed by evaluating the variable L/E_ν for each event,

$$P(\nu_\mu \to \nu_\tau) = \sin^2 2\theta \sin^2 \left[\frac{1.27\ \Delta m^2(\mathrm{eV}^2) L(\mathrm{km})}{E_\nu(\mathrm{GeV})}\right], \tag{5.11}$$

where L is the path length traveled by the neutrino and E_ν the energy of the neutrino.

The path length L is a function of the zenith angle θ_z of the incident neutrino and can be calculated using:

$$L(\theta_z) = \sqrt{(R-d)^2\cos^2\theta_z + (d+h)(2R-d+h)} - (R-d)\cos\theta_z, \tag{5.12}$$

where R is the Earth's radius, d is the depth of the detector, and h is the mean neutrino production height. The latter is a function of neutrino flavor, neutrino energy and zenith angle and it is calculated as described in item 9 in Sect. 3.3.3. The resolution in zenith angle for reconstructed neutrino events is shown in Table 3.3.

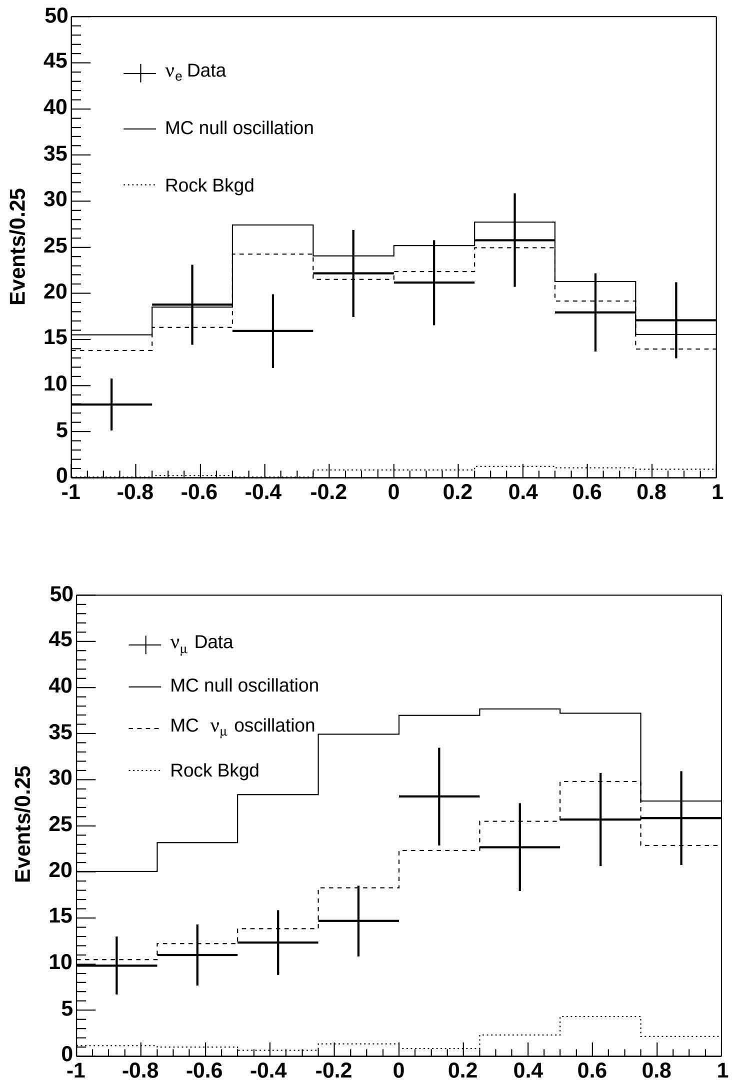

Figure 5.10: Zenith angle distributions for ν_e flavor (top) and ν_μ flavor (bottom) samples. The points with errors bars are the data, the solid histogram is the unoscillated Monte Carlo prediction, the dashed histogram is the MC weighted by the best fit oscillation parameters and the fitted normalization, the dotted histogram is the rock background contribution subtracted from the data.

With the Soudan 2 calorimeter, the neutrino energy for charged current reactions is measured via the final state reconstruction, with resolutions $\Delta E/E$ of 20% for ν_μ CC's and 23% for ν_e CC's in the HiRes sample.

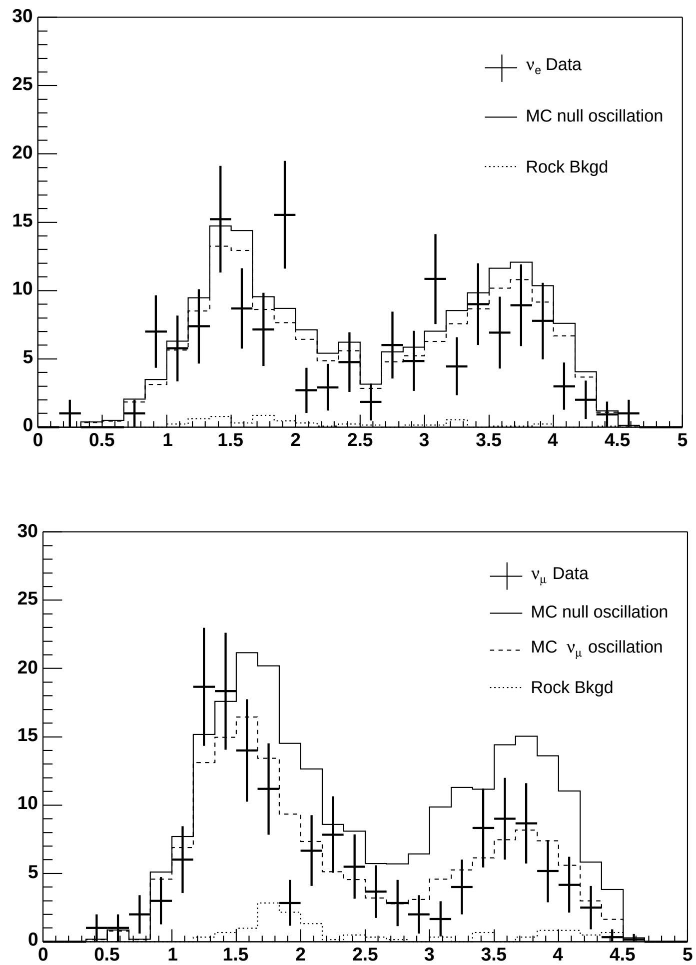

Figure 5.11: HiRes $\log(L/E_\nu)$ distributions for ν_e flavor (top) and ν_μ flavor (bottonm) samples. The points with errors bars are the data, the solid histogram is the unoscillated Monte Carlo prediction, the dashed histogram is the MC weighted by the best fit oscillation parameters and the fitted normalization, the dotted histogram is the rock background contribution subtracted from the data.

For null oscillations the L/E_ν variable distributes according to a phase space which reflects the neutrino points of origin throughout the volume of the Earth's atmosphere resulting in a doubly peaked distribution. The left hand peak is populated by downward-going neutrinos from the atmosphere above the detector, the dip region in the middle are from neutrinos incident from near the horizon and the right hand peak is from upward-going neutrinos from the other side of earth. Figure 5.11 (using $\log_{10}(L/E_\nu)$) shows that the ν_e flavor data follows the shape of the null oscillation MC distribution within $\sim 10\%$ of the overall normalization. The ν_μ data falls below the null oscillation MC above a $\log(L/E_\nu)$ value of ~ 1.5. As shown for the angular distributions, the data is consistent with oscillations of the ν_μ sample but not for the ν_e events.

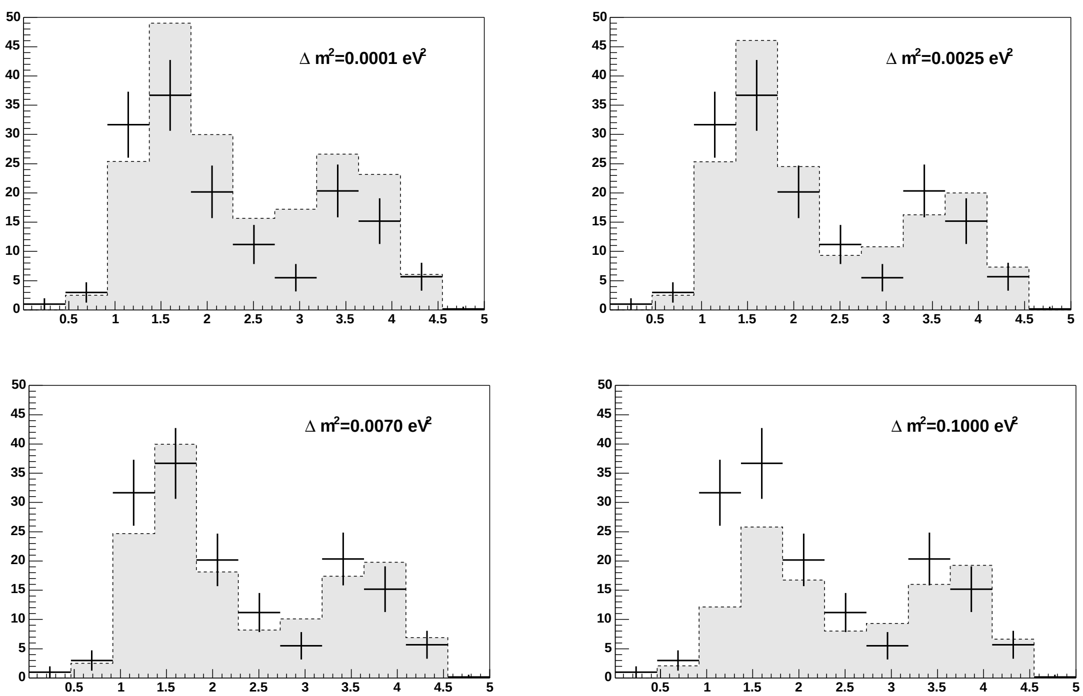

Figure 5.12: HiRes $\log(L/E_\nu)$ distributions for ν_μ flavor sample compared to different oscillation hypotheses. The points with errors bars are the data, the dashed histogram is the MC weighted by oscillation parameters ($\sin^2 2\theta = 1$) for each hypothesis and the fitted normalization.

It is possible to explore the possible oscillation hypotheses by comparing the ν_μ data to MC distributions weighted by different sets of oscillations parameters as shown in Figure 5.12. We choose $\sin^2 2\theta = 1$ for the maximal oscillation effect and plot the MC distribution weighted for ν_μ oscillations with different Δm^2 settings.

With $\Delta m^2 = 10^{-4}$ eV^2, the oscillation prediction stays above the data in most bins, indicating that not enough neutrinos oscillate. For $\Delta m^2 = 2.5 \times 10^{-3}$ eV^2 (Super-K value), the up-going neutrino flux (right peak) is now better described by the MC, but the expectation remains high for down-going neutrinos (left peak). The best agreement is achieved at $\Delta m^2 = 7 \times 10^{-3}$ eV^2. At a higher Δm^2, we find that the oscillation weighted MC falls below most bins, clearly a hypothesis disfavored by the data. These explorations of the oscillation parameters confirm that neutrino oscillations describe our data appropriately and that $\log(L/E)$ is an optimal variable to use in a detailed determination of the oscillation parameters for our data.

Chapter 6

Neutrino oscillation analysis

In our exploration of the Soudan 2 data in the previous Chapter, we have determined that the ν_μ component of the atmospheric neutrino data is consistent with oscillation whereas the ν_e component behaves within statistics as expected in the case of no oscillations. Thus it is natural to pursue an estimation of the oscillation parameters that best describe our data within a two neutrino oscillation model, namely ν_μ oscillating into ν_τ and ν_e unaffected by oscillations. Determining the statistical significance of the result, that is, appropriate confidence level (C.L.) intervals is also highly desirable.

In an initial approach we carried out a χ^2 fit of the oscillated Monte Carlo to the L/E data distribution of the data for each pair of values in the $\sin^2 2\theta$–Δm^2 plane. The minimum value among these χ^2 corresponded to our best fit ($\sin^2 2\theta_{best}$ and Δm^2_{best}). In order to obtain the 90% confidence level we took χ^2_{best}+4.61 and that defined the C.L. contour. The results for Soudan 2 data with this method were given in Ref. [74].

The method used in the above approach is known as a "global scan". It is a powerful technique but it does not provide reliable confidence intervals, more specifically it fails to achieve what statisticians denote as "proper coverage". The lack of proper coverage takes one of two forms: *i*) the determination of confidence intervals in parameter space is conservative (or is said to overcover) which is not considered a problem except for the loss of power in determining the best parameters; *ii*) the determination of confidence intervals underestimates the allowed region size (or is said to undercover) which is considered a serious flaw. The use of χ^2 provided a simple method to account for errors in the background determination as shown in Ref. [74], however it has the disadvantage of requiring a minimum number of events per bin. Since Soudan 2 is a low statistics experiment, this requirement forced us to choose wider bins in L/E, thereby limiting the resolution that could otherwise be achieved by the experiment.

The Particle Data Group has recommended [75] the use of the "unified approach" proposed by Feldman and Cousins in Ref. [2] as the best way to construct reliable confidence level intervals. The Feldman-Cousins method uses classical (non-Bayesian) intervals and therefore avoids the use of subjective prior probability density functions for the parameters being measured. It is recommended in cases where other classical methods and Bayesian analyses are either over-conservative or give pathological results (e.g. empty sets in the physical region). In particular, the Feldman-Cousins approach is preferred over the other methods when the physics of the problem implies that *i*) there are non-Gaussian errors, and/or *ii*) at least one of the parameters to be determined is constrained by physical arguments. The Feldman-Cousins approach addresses these problems and has a further advantage, namely, the goodness of fit C.L. is decoupled from the construction of the confidence interval C.L.

6.1 Feldman-Cousins method

In their paper, Feldman and Cousins use Neyman's original construction to obtain classical confidence intervals and advocate a particular choice of ordering based on likelihood ratios. The choice of ordering is not novel and it was explained to be naturally implied by the theory of the likelihood ratio test in the classic text by Kendall and Stuart (Sec. 23.1 of Ref. [76]) much earlier. The paper presents several applications of this choice of ordering to the construction of confidence intervals for the presentation of scientific results. In particular, they described in detail a recipe for the case of neutrino oscillation searches.

The ordering principle proposed is the likelihood ratio which for a vector of measurements x is

$$l = \frac{\mathsf{L}(x|\theta)}{\mathsf{L}(x|\theta_{best})} \tag{6.1}$$

where θ is the vector of unknown parameters which are to be determined and θ_{best} represents the parameters that give the highest probability for $\mathsf{L}(x|\theta)$ for physically allowed values of θ. The θ_{best} parameters correspond to our best estimate of the true hypothesis H_0 with the unknown true parameters θ_0. Arranging all possible measurements for a given θ in decreasing rank, the critical region is defined as the set of measurements such that

$$\int_0^{l_\alpha} l(x|\theta) = \alpha \tag{6.2}$$

where α is the confidence level probability and l_α is the likelihood ratio at α confidence. Once an actual measurement is made, the confidence region for the true value θ_0 is the union of all θ whose acceptance regions include the value θ_{best}.

Thus, in the Feldman-Cousins prescription, there is a condition that must be satisfied for any confidence interval probability α (*i.e.* 90%) that the true unknown value should lie inside the interval in a fraction α of experiments. An interval that satisfies this requirement provides proper coverage of the measured parameter. However, for any value α, the confidence regions which satisfy this requirement can be any of upper limits, central intervals or lower limits. This method specifies a mechanism for choosing particular confidence belts that provide proper coverage while retaining the power to eliminate unlikely values.

The prescription assumes the ability to simulate hypothetical measurements in order to produce the likelihood ratio l_α for each possibility of the unknown parameters θ. The simulation of hypothetical experiments and the use of this method also accomodate the treatment of nuisance parameters and systematic errors in a very convenient way. For the nuisance parameters the likelihood ratio can be extended to include them as a new set of parameters θ_s for which the likelihood is maximized. The systematic errors can instead be included as variations of a parameter or a variable within a known (and independently calculated) error in the simulated experiments.

The elements of the method used for our neutrino oscillation analysis now include:

Desired parameters (θ): These are the parameters to be determined by maximizing the likelihood for which proper coverage is provided by the described prescription, simulating hypothetical measurements for each possible parameter set. For our neutrino oscillation analysis these are Δm^2 and $\sin^2 2\theta$.

The nuisance parameters (θ_s): Parameters of "no or little interest" but which are needed to determine the desired parameters. Statisticians suggest that proper coverage is obtained by maximizing the likelihood with respect to them. They become parameters of the fit but coverage is not ensured. For our analysis this will be the overall Monte Carlo normalization.

The systematic errors: Each simulated hypothetical experiment receives a random variation within the known error in any parameter or variable that may have a systematic error. If this is done on a nuisance parameter, the likelihood can be then maximized respect to this parameter. An example of this element in our analysis is the background fraction.

The method can be converted to use a χ^2 formulation but, due to the limited number of events and the issues with χ^2 described earlier, we prefer the likelihood approach. In Sect. 6.2, the determination of the desired parameters using this method is described. Sect. 6.3 shows the procedure to obtain the confidence level contours using simulated experiments.

6.2 Determination of the oscillation parameters

To determine the neutrino oscillation parameters Δm^2 and $\sin^2 2\theta$ from our data we construct a likelihood function L which will later allows us to implement the ordering principle proposed by Feldman and Cousins. For points (i, j) in the physical region of the $(\sin^2 2\theta_i, \log \Delta m_j^2)$ plane, we wish to find the MC expectation which minimizes the negative logarithm, $\mathcal{L}$, of the likelihood L at each point:

$$\begin{aligned}(\mathcal{L}_{data})_{ij} &= -\ln \mathsf{L}(\sin^2 2\theta_i,\ \Delta m_j^2,\ f_\nu) = \\ &= \sum_{k=1}^{bins} \left[-N_k(data - bkgd)\ln(f_\nu N_k(MC)) + f_\nu N_k(MC)\right] \qquad (6.3)\end{aligned}$$

where $N_k(data - bkgd)$ is the number of neutrinos obtained from background subtracted gold data, $N_k(MC)$ is the weighted MC expectation and the MC flux normalization f_ν is a free parameter in the fit and therefore a nuisance parameter. The function $(\mathcal{L}_{data})_{ij}$ is summed over thirty-three data bins which include all events from Table 6.1.

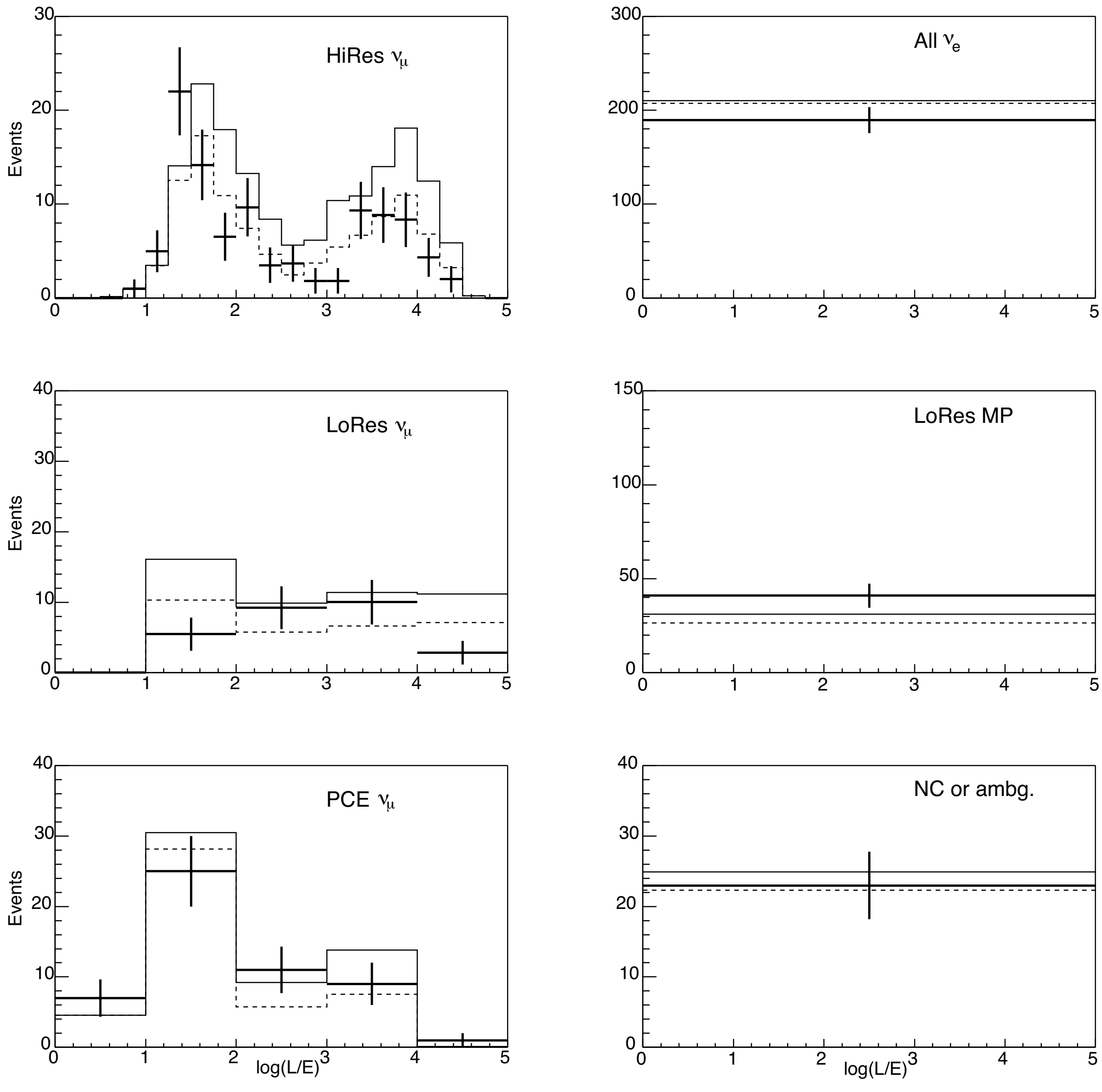

Figure 6.1: Comparison of data samples with the null oscillation expectation (solid histogram) and the best fit Monte Carlo (dashed histogram).

	# bins	$N(data - bkgd)$	$N(MC)$
Contained HiRes ν_μ	20	101.9	1115.1
Contained LoRes ν_μ tracks	5	27.5	332.8
Partially Contained ν_μ	5	52.7	384.3
All ν_e	1	188.8	1412.6
Contained LoRes MP	1	41.9	213.5
NC or ambiguous	1	24.4	165.7
Event Totals		437.2	3624.0

Table 6.1: Soudan 2 total number of neutrinos in background subtracted data event samples and weighted MC used for the analysis.

We choose the binning to maximize the impact of the $\log(L/E)$ distributions that may have an oscillation signature. We assign 20 bins of widths consistent with resolution for the contained ν_μ HiRes sample, 5 bins for the partially contained ν_μ and 5 more for the LoRes single track events. Separate event population bins are assigned for ν_e events, LoRes multiprongs, and NC/ambiguous flavor samples; these populations will further constrain the flux normalization. Fig. 6.1 shows the data distributions compared to the null oscillation expectation and to the Monte Carlo oscillated to the best fit oscillation parameters. The categories have been optimized both to give maximum resolution in $\log(L/E)$ where required and to facilitate background subtraction.

To take into account oscillations for a given pair of values ($\sin^2 2\theta$, Δm^2), we weight each Monte Carlo true ν_μ-flavor event by the probability that the neutrino has oscillated using the factor:

$$w = (\ 1 - \sin^2 2\theta\ \sin^2[1.27(L/E)\Delta m^2]\ )$$

where L/E is calculated from the truth values for the particular event. The total number of events in each Monte Carlo bin is then the sum of the weights for events in that bin.

At every point (i, j) on the plane, where (i, j) denotes a pair of values of Δm^2 and $\sin^2 2\theta$, we fit the expected MC distribution to the data. We restrict ourselves to the physical region following the Feldman-Cousins prescription and find the minimum negative log likelihood $\mathcal{L}_{best}$ on the plane which occurs for some $\sin^2 2\theta_{best}$ and Δm^2_{best}.

For every point in the plane we construct the quantity,

$$(\Delta\mathcal{L}_{data})_{ij} = \mathcal{L}_{ij} - \mathcal{L}_{best}$$

which is the implementation of the ordering principle suggested by Eq. 6.1 and as in Sect. V.B. of Ref. [2]. The $\Delta\mathcal{L}$ surface obtained for our data can be seen in Fig. 6.2.

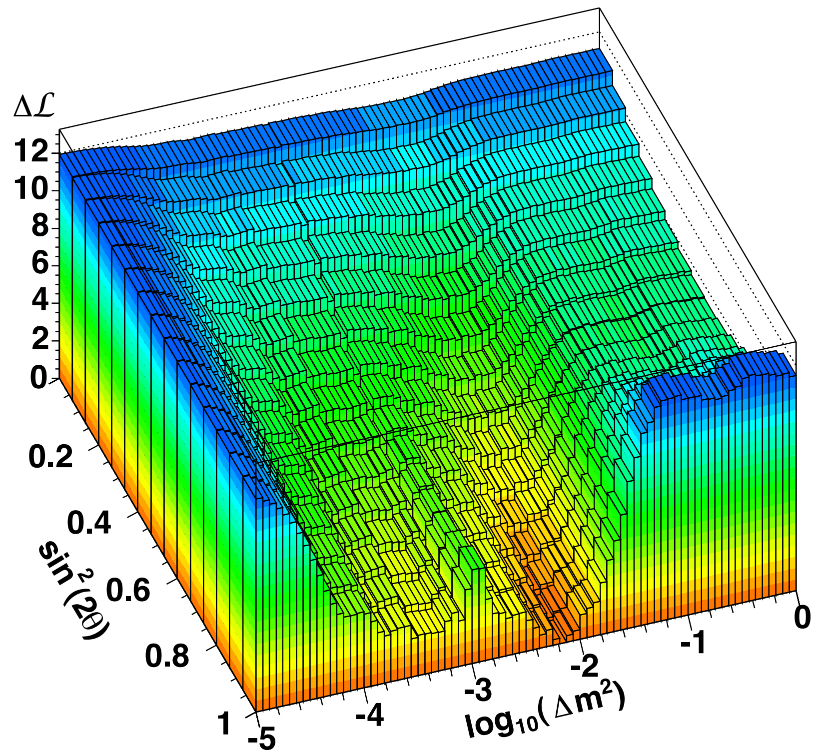

Figure 6.2: The surface $\Delta\mathcal{L}$ for Soudan 2 data. The height of the ij-th bin is the calculated $(\Delta\mathcal{L}_{data})_{ij} = \mathcal{L}_{ij} - \mathcal{L}_{best}$.

A valley of low $\Delta\mathcal{L}$ values is clearly discernible slightly below $\log(\Delta m^2) = -2$. The lowest point occurs at values $\sin^2 2\theta = 0.97$, $\Delta m^2 = 7 \times 10^{-3}$ eV^2, with flux normalization $f_\nu = 0.90$. Note that the normalization has been used as a parameter of the fit and the likelihood has been maximized with respect to it, effectively treating it as a nuisance parameter. The background instead has been introduced as an input obtained from the independent determination shown in Chapter 4 and the errors in its determination need to be taken into account in determining the confidence level intervals.

6.3 Determination of confidence level regions

After calculating $\Delta\mathcal{L}$ at every point for the data, we then calculate the acceptance at each of these points effectively implementing Eq. 6.2. In order to accomplish this, we simulate large groups of "synthetic data sets" [77] for each possible combination of oscillation parameters. By construction, each simulated data set holds the same statistical relationship to the oscillation parameters from which it was generated as our data holds to Nature's true oscillation parameters. In this way we mimic our understanding of the underlying process and of the measurement errors in our experimental procedure.

For each of these synthetic data sets we perform the same procedure to estimate the oscillation parameters as was followed for the original data. We carry out a likelihood minimization and then a search for the $\mathcal{L}_{best}$ from which a $\Delta\mathcal{L}$ is then produced.

By simulating enough synthetic data sets at a point, we map out a probability distribution of $\Delta\mathcal{L}$ and thus determine the acceptance at that point. The advantage of this technique is that it allows the errors of parameter estimation to be characterized in a precise way at each point.

6.3.1 Monte Carlo simulation of synthetic data

In order to carry out the determination outlined above, we must decide how to simulate a synthetic data set at each point of the $\sin^2 2\theta$–Δm^2 plane. In Soudan 2, generating thousands of experiments and then scanning and reconstructing them in the standard way is not feasible. However for our analysis we need only to generate an L/E distribution for each synthetic data set from an *a priori* known distribution. The known distribution we use is the two dimensional $\log(L/E)_{true}$ versus $\log(L/E)_{meas}$ distribution taken from our measured Monte Carlo sample; this distribution for the HiRes ν_μ sample is shown in Fig. 6.3. The use of the this distribution accounts for errors and biases in the reconstruction of L/E without having subject generated events to a laborious processing chain. Similar distributions are used for the other ν_μ samples. For non-ν_μ events however, this procedure is not needed since we do not need to take their L/E distributions into account.

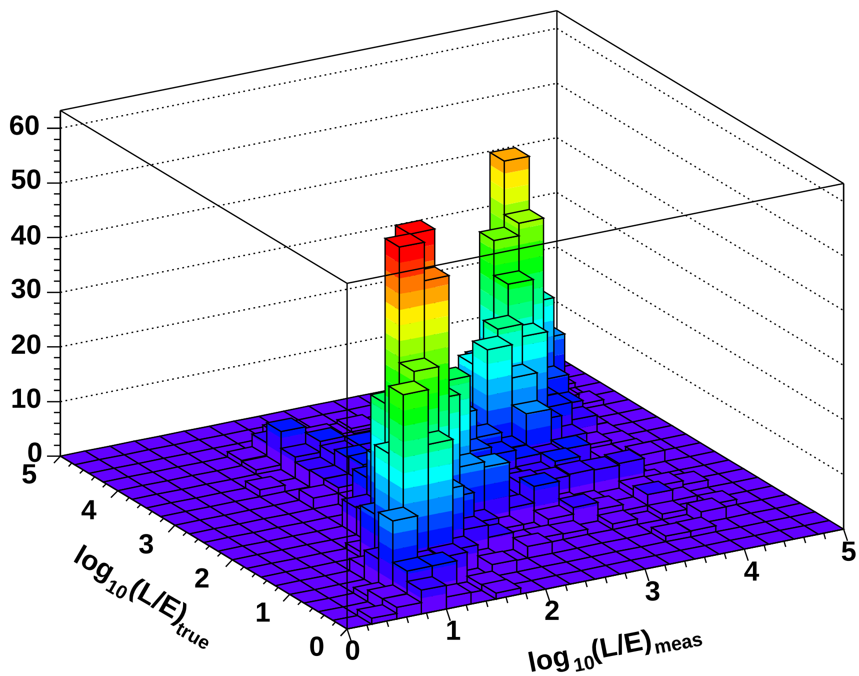

Figure 6.3: Two-dimensional $\log(L/E)_{true}$ vs. $\log(L/E)_{meas}$ distribution for the Soudan 2 null oscillation HiRes Monte Carlo.

Thus we simply generate synthetic data sets that follow the distribution of Fig. 6.3. The total number of events in each experiment is assigned randomly according to Poisson distributions with means at $\bar{n}_e$ and $\bar{n}_\mu$ in order to account for the statistical error in the ratio-of-ratios. To preserve the ratio between ν_μ–flavor and ν_e–flavor events, we generate a mean number of ν_e events equal to the number of data events in that sample. That is, we generate using

$$\bar{n}_e = n_e^{data}$$

and with a mean number of ν_μ events which is set according to

$$\bar{n}_\mu = n_\mu^{MC(oscillated)} n_e^{data} / n_e^{MC}.$$

Note that we use the ν_e events as a reference sample since we assume that they have not oscillated.

Once the neutrino $\log(L/E)$ distribution has been obtained, we then generate a background distribution for the synthetic data set from which we then subtract the background that has been previously obtained for the data. This simulates the error in the background determination that we may have incurred using the depth fits. The synthetic rock distribution is sampled from the $\log(L/E)$ distribution of shield-tagged rock data, and the b factor is randomly generated according to a Gaussian distribution with the mean equal to the b determined from the corresponding distribution in the data and $\sigma = \Delta b$. In a separate study [78], we showed that for a fixed value of b and statistical fluctuations in the rock distribution, the calculated b-values are distributed as a Gaussian.

6.3.2 Construction of the C.L. contour

At each point (i, j) of the $\sin^2 2\theta$–Δm^2 plane we generate N_{exp} experiments of $N_D = n_e + n_\mu$ events, where n_e includes all non-ν_μ samples. We have chosen N_{exp} to be 1000 in order to obtain reasonably populated distributions at each of 1200 points. Each of these simulated experiments is treated as if it were the data. Thus for experiment k ($k = 1...N_{exp}$) we minimize the $\mathcal{L}$ at every point in the plane and we find $\mathcal{L}_{best}$. Once $\mathcal{L}_{best}$ is obtained, we have

$$\Delta\mathcal{L}_{ij} = \mathcal{L}_{ij} - \mathcal{L}_{best}$$

for experiment k, where $\mathcal{L}_{ij}$ is the minimum at the point (i, j).

By repeating this procedure 1000 times, we generate a distribution of $\Delta\mathcal{L}_{ij}$. An example of such a distribution is shown in Fig. 6.4 for an illustrative point in the plane. By generating this distribution, we are in effect arranging $\Delta\mathcal{L}$ by ranking as in Eq. 6.2. From this distribution we find the value of $\Delta\mathcal{L}$ below which α of the simulated experiments occur; this value becomes $(\Delta\mathcal{L}_\alpha)_{ij}$. Repeating the latter procedure for

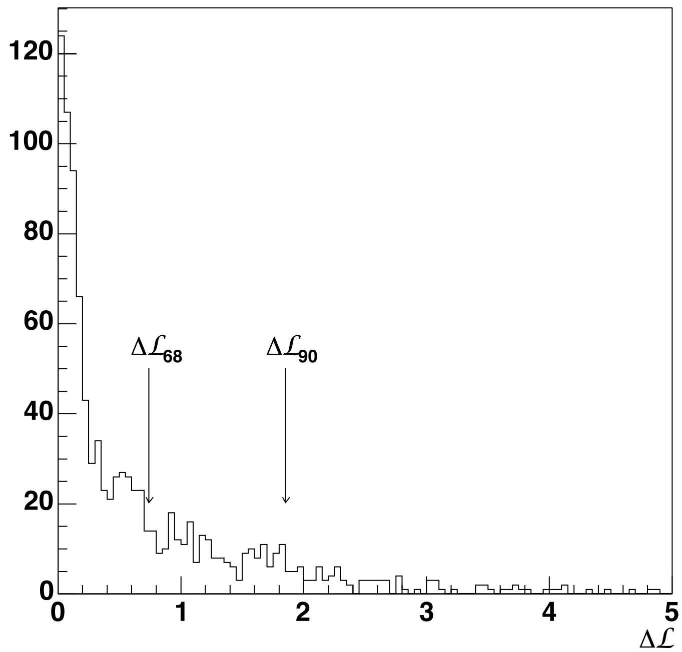

Figure 6.4: A $\Delta\mathcal{L}$ distribution for 1000 synthetic data sets at $\Delta m^2 = 10^{-4}$ eV^2 and $\sin^2 2\theta = 0.5$. For the distribution at this particular point in the parameter plane, $\Delta\mathcal{L}_{68} = 0.75$ and $\Delta\mathcal{L}_{90} = 1.86$.

every point in the $\sin^2 2\theta$–Δm^2 plane, we obtain the surface which is shown in Fig. 6.5 for $\alpha = 90\%$. Note that the $\Delta\mathcal{L}_{90}$ value on the surface differs significantly from the plane at 2.3; it varies from point to point. The central shaded portion has values above $\Delta\mathcal{L}_{90} = 2.3$, however outlying regions have $\Delta\mathcal{L}$ values that are lower.

Finally, to obtain the acceptance region we impose the condition that a point (i, j) is within the confidence interval probability α (which in this case is a confidence level contour) if

$$(\Delta\mathcal{L}_{data})_{ij} < (\Delta\mathcal{L}_{\alpha})_{ij}.$$

The contours thereby obtained for $\alpha = 90\%$ and $\alpha = 68\%$ are shown in Fig. 6.6. A sensitivity contour for 90% is also shown. The sensitivity contour is obtained by using the Monte Carlo expectation at the best fit point as if it were the data and calculating the confidence level contour for that point. The allowed 90% region is in reasonable agreement with the expected sensitivity for our result.

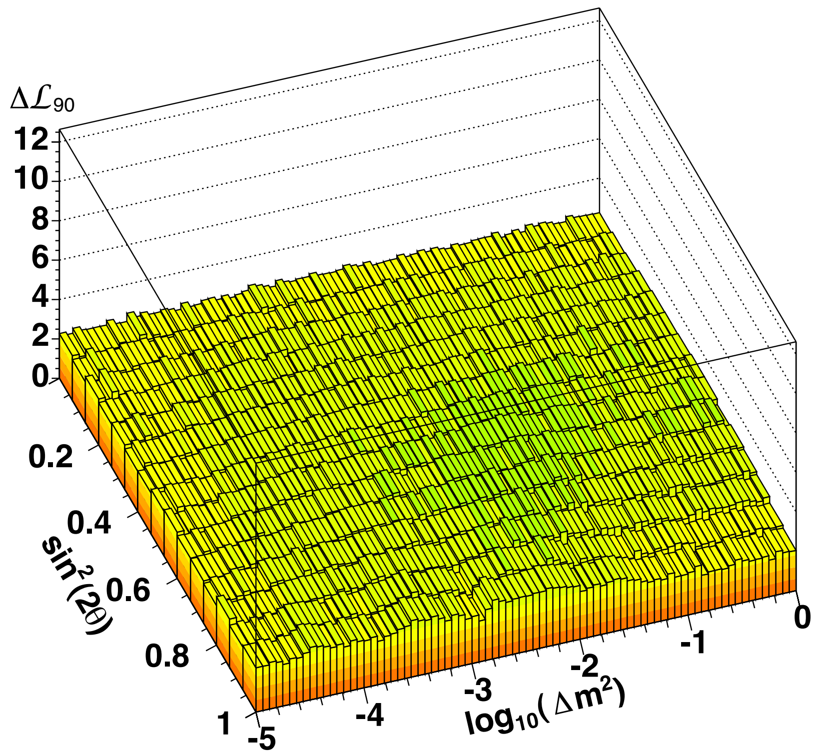

Figure 6.5: The acceptance surface $\Delta\mathcal{L}_{90}$ generated for the Soudan 2 data.

It must be noted that, even for the modest number of points ($N_p = 1200$) in the oscillation parameter plane, this is an intensive computing task. Furthermore, 1200 points, 80 along the $\log(\Delta m^2)$ axis and 15 along the $\sin^2 2\theta$ axis, give only a precision of only 0.075 and 0.067 respectively. We implemented less sampling density in $\sin^2 2\theta$ because the function is very smooth in this direction and therefore a simple interpolation can be done later. The situation in $\log(\Delta m^2)$ is more complicated since there are fluctuations due to the oscillatory nature of the function and the lack of statistics.

The number of $\mathcal{L}$ minimizations needed goes as the factor $N_{loops} = N_{exp} \times N_p \times N_p$. In our case $N_{loops} \approx 10^9$, therefore the minimization time has to be optimized as much as possible. We found that using the likelihood method in the form of Eq. 6.3 allows us to find the analytical solution for the normalization: $f_\nu = N_{tot}(data -$

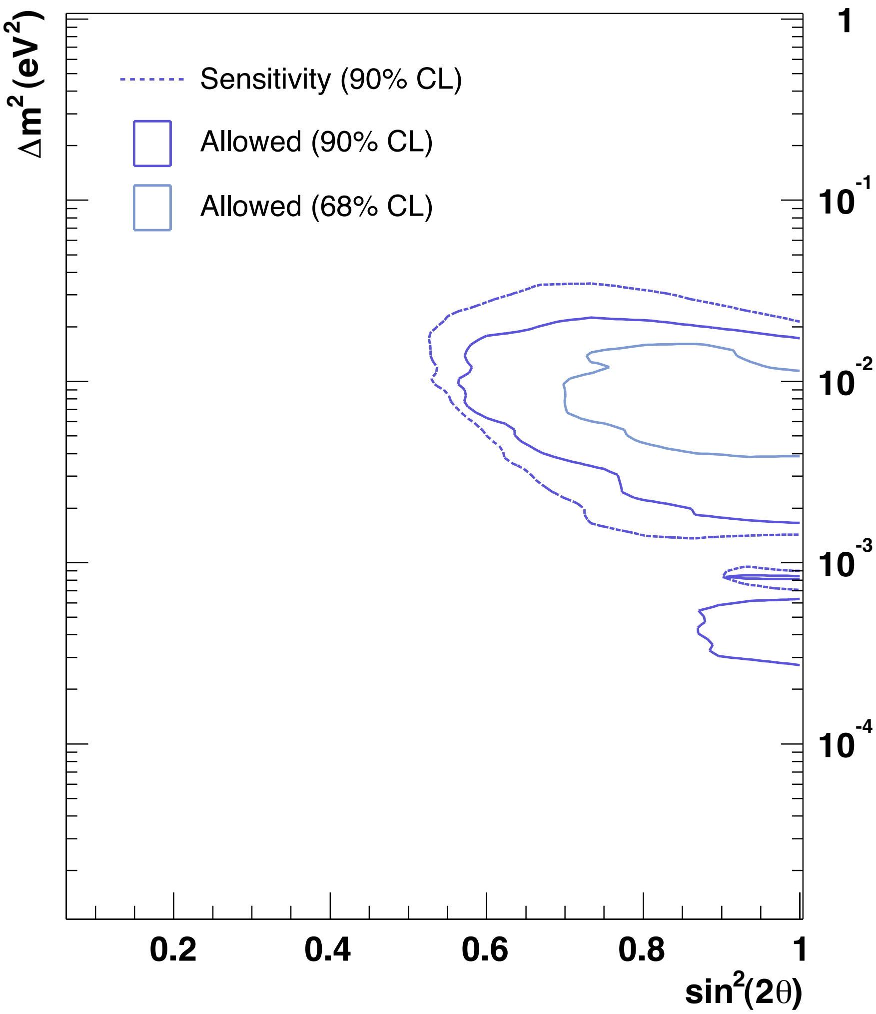

Figure 6.6: The 68% and 90% C.L. allowed regions for the Soudan 2 data.

$bkgd)/N_{tot}(MC)$. Other forms of the likelihood can use this value as an approximation, if an analytic solution is not possible. In the case of χ^2 where our analytical solution does not hold, then optimization of the algorithm using known fast minimization routines such as the *golden section method* and *Brent's method* [77] are highly recommended to reduce computing time to a minimum.

6.3.3 Statistical and systematic error

We considered statistical and systematic errors that could affect our measurement and therefore have an impact on the determination of the confidence level regions. These errors were introduced as one of the elements in the method described in Sect. 6.1.

Low statistics in the data neutrino events affect the overall size of the allowed region and impose a limit on the quality of the measurement. They also produce other systematic effects that we have taken into account in this analysis. Variations in the relative number of ν_μ events with respect to ν_e events could have an impact on the value of the normalization and therefore in the confidence region along $\sin^2(2\theta)$. As described in the previous section the number of events in each sample was allowed to vary independently in the synthetic experiments and the normalization fitted each time as a nuisance parameter.

A further impact of the low statistics occurs due to the necessity of having finite bin widths in the histograms created in $\log(L/E)$ for data and MC. Fluctuations in the resulting confidence level contours were observed depending on the bin starting point. This was resolved by averaging the results from many starting points. Later on, in order to address this issue, an independent analysis was carried out using an unbinned method which has been presented as the experiment's official result. The resulting contours of the two analyses are in excellent agreement as can be seen in Fig. 6.9. The level of agreement obtained strongly suggests that our averaging of the different binned results addresses the issue of binning dependence satisfactorily.

A systematic error of possible impact arises with the determination of background in the data sample. In the analysis reported here this was carried out independently using the depth distributions, assuming that the rock distributions are a good model of the zero-shield-hit background. To address this systematic error, we generated synthetic rock distributions and allowed the b factor to vary within the errors of the background determination for the data. Since the b factor is not determined for each experiment we have assigned it randomly based on the error from the depth fit. It is possible that this method overestimates the error in the determination of b resulting in slightly bigger confidence level intervals. We address this by comparing to a result where the background has not been randomly generated and just pure neutrino distributions are compared in Fig. 6.7. A less conservative approach would result in a confidence level region passing somewhere in between both contours.

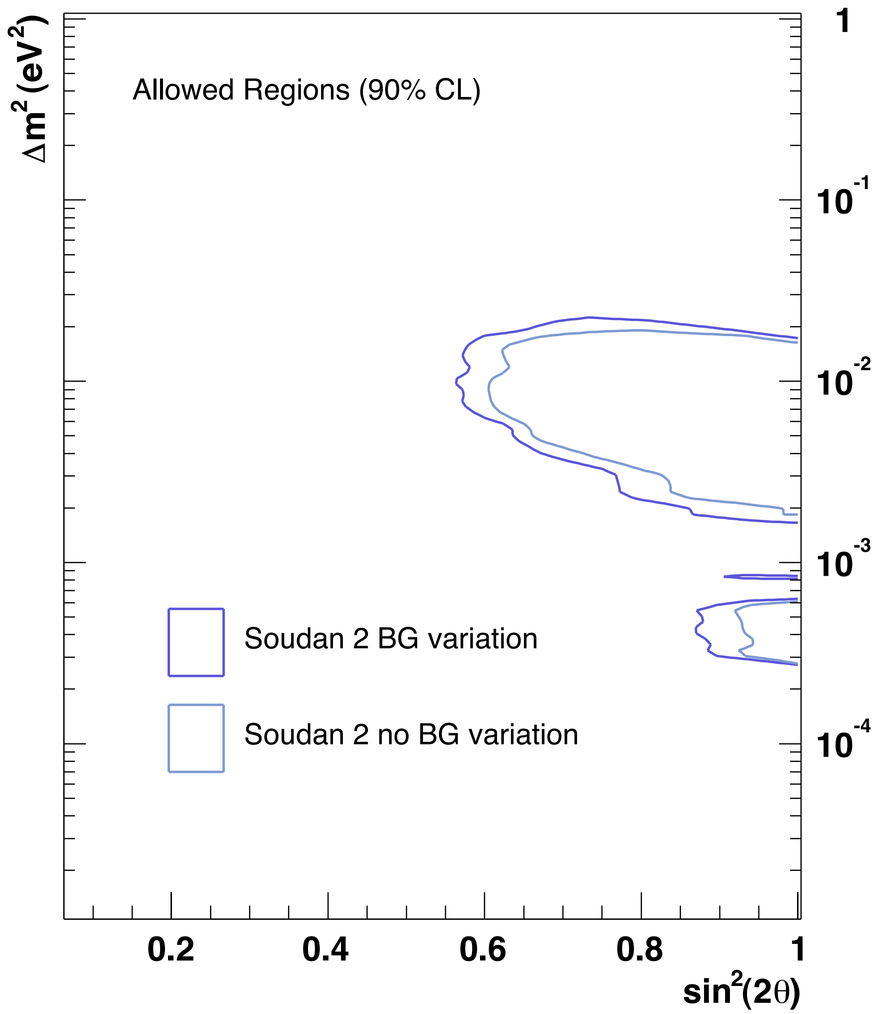

Figure 6.7: The allowed regions at 90% C.L. allowed regions for the Soudan 2 data with and without background systematic variations.

Another systematic error to be considered is the model of the atmospheric neutrino flux used for the Monte Carlo. The results of this thesis is based on the Bartol '96 fluxes, calculated using a one-dimensional model as described in Sect. 5.1. We have also calculated the allowed regions using the Battistoni *et al.* 3D calculation to study the impact of a different neutrino flux model. For this exercise, we have used the neutrino fluxes at the Soudan site as calculated by Battistoni *et al.*, however we use the collaboration's production height algorithm which is based upon a 1D model atmosphere [58]. The results are shown in Fig. 6.8. In comparison to the Bartol '96 result, the fit with a 3D flux is of similar quality and yields identical best fit oscillation parameters. Moreover, the alteration in the 90 % allowed region is quite modest. The main difference between the two fits lies in the best fit for the normalization parameter; this is high by 5% in this case compared to 10% low in the Bartol '96 case.

Other possible systematics arising with the neutrino flux as a function of energy and the ratio of ν_e to ν_μ events were not taken into consideration in this analysis since we regard them to be negligible in comparison to the statistical and systematic errors already considered. However, the latter systematics in the flux together with possible systematics in the energy calibration of the detector were taken into account by the unbinned analysis shown in Fig. 6.9. The resulting best fit parameters and allowed regions are quite consistent which gives us confidence that these effects are indeed small and do not change the result in any significant way.

6.4 Discussion of results

The official Soudan 2 atmospheric neutrino result is based on an analysis that is similar to the one presented in this thesis which was carried out independently. Both analyses use the Feldman and Cousins method with the ratio of likelihoods as an ordering principle for the calculation of the confidence levels and both use the same data sets with the same cuts. The substantive difference between the analyses are: *i*) the official analysis uses continuous pdfs for $\log(L/E)$ rather than the binned distributions used in this analysis; *ii*) the background determination in the official analysis is part of the overall likelihood fit using both the depth variable and the $\log(L/E)$ variable, whereas in this analysis the background was an input parameter to the overall fit determined independently of the oscillation hypothesis; *iii*) the official

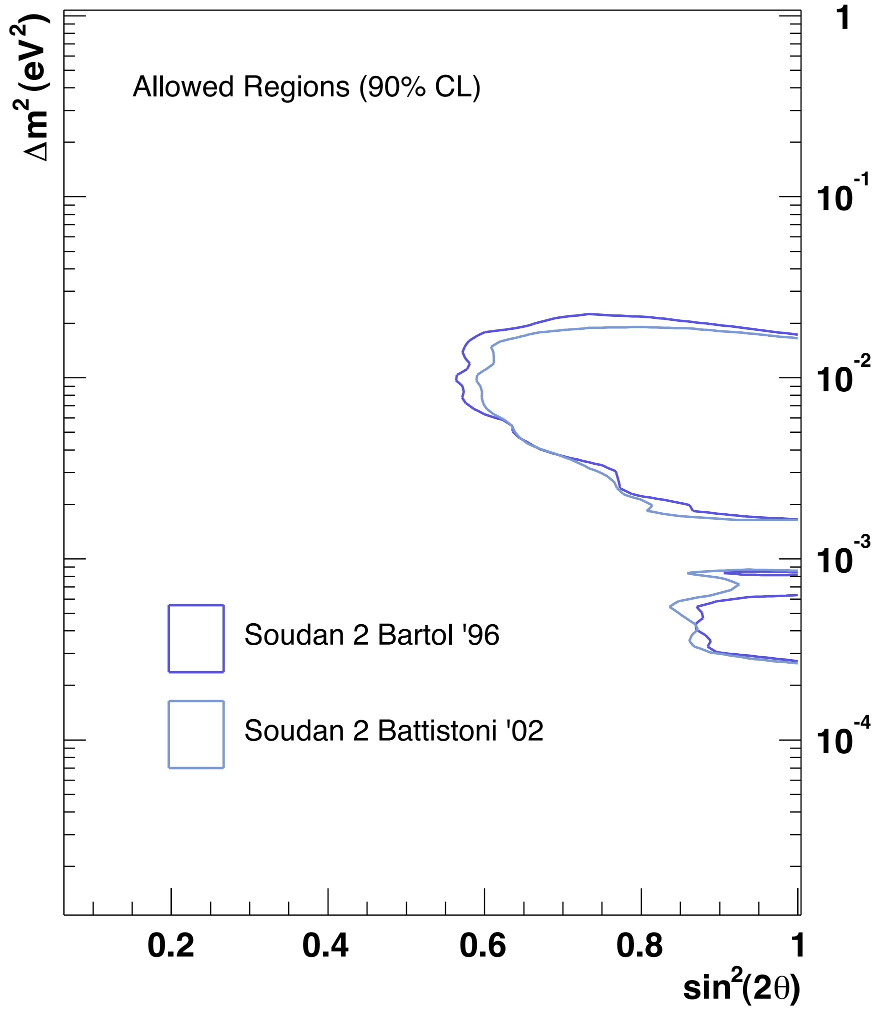

Figure 6.8: The allowed regions at 90% C.L. for the Soudan 2 data for two different flux calculations.

analysis used a bootstrapping method to create the synthetic experiments, whereas for this analysis the two-dimensional $\log(L/E)_{true}$ vs. $\log(L/E)_{meas}$ distribution of the Monte Carlo was used; and *iv*) different systematics were taken into account in each of the analysis as described in the previous section. Despite these differences the results are in good agreement as is shown in Fig 6.9.

Our 90% confidence level region is shown in Fig 6.9, compared to the most recent

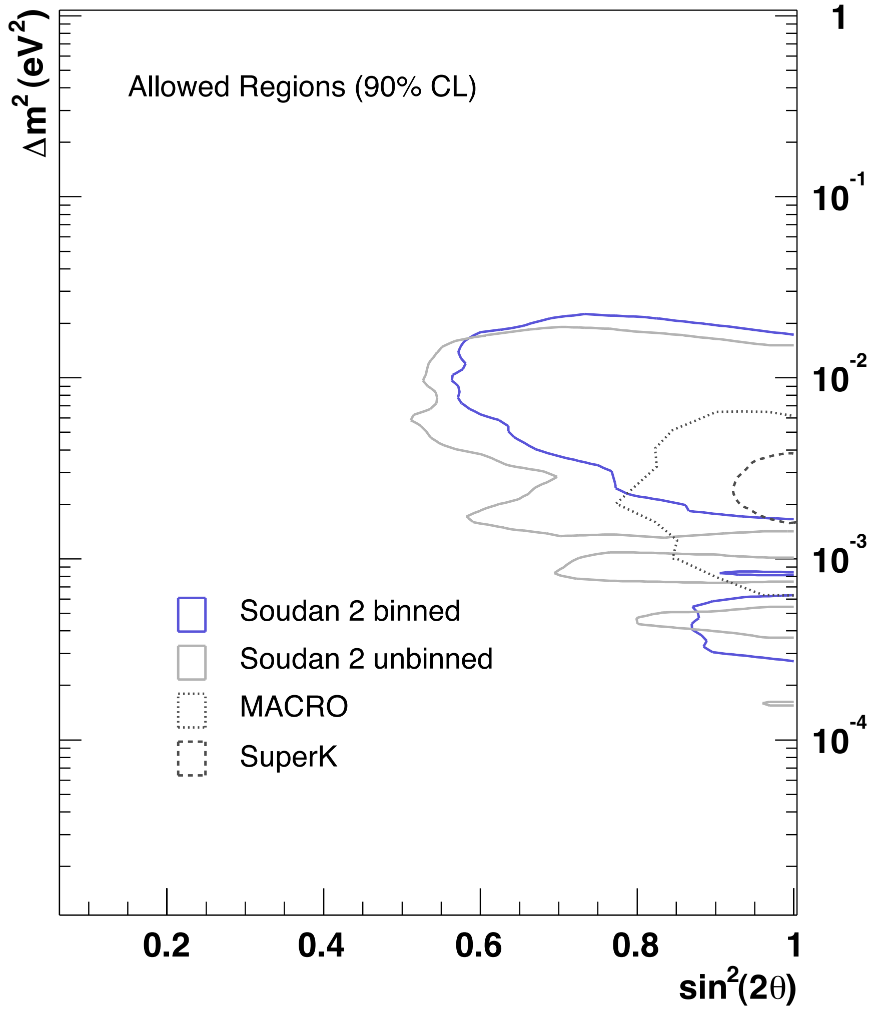

Figure 6.9: The allowed region at 90% C.L. for the Soudan 2 data compared to the unbinned Soudan 2 analysis and other experiments.

Super-K allowed region [79] and to a contour from the MACRO experiment [80] using upward muons. The Soudan 2 result presented here is in agreement with the results of both experiments. Although $\mathcal{L}_{best}$ occurs at $\Delta m^2 = 7 \times 10^{-3}$ eV^2, the flat basin of the $\Delta\mathcal{L}_{data}$ surface extends to lower Δm^2 values. Super-K has reported their best fit to be $\Delta m^2 = 2.5 \times 10^{-3}$ eV^2 and $\sin^2 2\theta = 1.0$. Our allowed region is compatible with that as well as with somewhat higher Δm^2 values. Our measurement provides confirmation, for atmospheric neutrino oscillations in the oscillation parameters allowed region obtained by Super-K using a very different detection technique.

Appendix A

Scan Rules

A.1 Filter scan rules

Following an extensive collaboration internal discussion and review, the Filter Scan Rules were finalized and distributed in a Soudan 2 internal note [81]. Subsequently these rules were used for first pass scanning of all Soudan 2 data for contained events. The Filter scan is designed to ensure event containment and to eliminate remnant cosmic ray background or detector noise events which managed to get through the experiment's initial FILTER codes. These rules are distinct from those used for the subsequent Bronze scanning and assorted check scans wherein events are classified according to final state topology.

A.2 Bronze scan rules

The final version of the Bronze scanning rules were distributed via e-mail on September 18, 1996. The Bronze scanning (of the Filter scan output) provides evaluations of contained events in three general areas:

A) Bronze containment and background rejection criteria are more restrictive than those of FILTER processing, and these may cause events to be rejected.

B) Quality and information flags on individual events are introduced by the scan. Flags that indicate problems (e.g., a higher probability as cosmic ray related background) can result in event rejection under a "two strike" rule.

C) Events are classified according to topology, as single track, single shower, multiprong or as CVC or PCE events. Observation of primary or remote recoil protons, of endpoint decays, and of protonicity aspects are recorded using various information flags.

Category A

1. The event fails the filter scan rules and should not have reached this stage. The filter scan rule it failed should be indicated by bringing up the filter scan box and clicking on the appropriate section. A comment may also be helpful if the failure is obscure.

   Click on "FILTER RULES FAILURE"

2. A track or shower with a T0 defined by a loom crossing,blob or shield hit can extrapolate out of a detector crack OR a track or shower without a defined T0 can extrapolate out of a detector crack with a suitable adjustment of T0.

   In either case no more than 10cm of active, unhit detector should be crossed

   Click on "TRACK CAN POINT OUT"

3. A track (not shower) extrapolates out of the detector via the inefficient central trace region, defined to be +- 20 ticks on either side of the central trace. The distance to the outside of the detector must be less than 50cm.

   The track must have a defined T0 (loom crossing,blob or shield hit)

   Click on "TRACK LEAVES MODULE CENTRE"

4. A track (not shower) exits between columns of tubes. The tube column may be either vertical or at the two 60 degree lines of symmetry. There must be at least 4 tubes read out in the line of symmetry at the end of the track and the track end must be less than 50cm from the detector exterior.

   Click on "TRACK LEAVES PARALLEL TO ANODES"

5. The event has a vertex in the side-skin,cover-plate or load-plate region, *i.e.* outside the active detector volume.

Click on "VERTEX OUTSIDE ACTIVE REGION"

6. The event is defined as breakdown.

   Click on "BREAKDOWN"

7. The event is a crack splat that does not satisfy the filter scan rules. It must have at least two separated ionisation clusters along the crack OR a shield hit consistent with a muon passing down the crack and an ionisation cluster touching the crack with the shield T0.

   Click on "CRACK SPLAT"

8. There is something else against the event (not defined here) which must reject the event. The "something else" must be detailed in a comment.

   Click on "OTHER FATAL PROBLEM"

Category B

9. There are a suspiciously large number of single or double hits that could be in time with the event, and in the vicinity of the event. This should be checked by an objective program. There is neither a clear 4-hit track/shower that should reject the event for FILTER fiducial volume reasons, nor a clear 3-hit entity that would set the FATAL EXTERNAL SHOWER flag (see rule 27 below). This does not constitute a "strike".

   Click on "CHECK FOR EXTERNAL SHOWER"

10. A track starts within 3 cm of the module centre, using a T0 defined by a wireplane crossing or blob. A strike.

    Click on "TRACK STARTS NEAR MODULE CENTRE"

11. A track or shower starts on anodes 2,3,61 or 62. A strike.

    Click on "TRACK STARTS NEAR ANODE CRACK"

12. A track or shower starts on cathodes 235,236,237,238,257 or 258. Strike.

    Click on "TRACK STARTS NEAR LOAD PLATE CRACK"

13. A track or shower starts within 10 ticks of a wire plane crack (using the T0, compatible with the other information in the event, that puts the first hit furthest from the wireplane) but does not have a wire plane blob at its end. A strike.

    Click on "TRACK STARTS NEAR WIRE PLANE CRACK"

14. A track or shower has hits on cathodes 21-22,470-474,anodes 14,15 or 240,241 if the latter are exterior to the detector. A strike.

    Click on "HITS NEAR EDGE OF FIDUCIAL VOLUME"

15. There is something else against the event (not defined here) which is a problem against the event to be counted in a two strike rule. The problem must be documented in the comment.

    Click on "OTHER NON-FATAL PROBLEM"

16. There is a possible detector problem, i.e. a track looks as though it might exit through a dead or inefficient region of the detector. Events flagged thus will be checked via SDI, ANLTUBE and all the other diagnostics we posses. Many of these events will in fact be OK and thus the category C classifications must be carried out.

    Click on "CHECK DETECTOR FUNCTION"

Category C

17. The event is a single, short, highly ionized track, and thus very likely to be a NC- or neutron-induced single proton. Such events will be checked by an independent program and removed from the track sample before analysis if verified.

    Click on "SINGLE PROTON CANDIDATE"

18. The event has a proton recoil. Recoils are defined as heavily ionising tracks which have no noticeable curvature. These will be checked by the independent proton-identification program.

Click on "PROTON RECOIL"

19. The event has a neutron recoil. Neutron recoils are defined as secondary interactions not attached to the primary event vertex which are either showers which are more than 80 grams distant from the vertex or tracks or multiprongs. The distance from the primary vertex must be less than 320 grams.

    Click on "NEUTRON RECOIL"

20. The track has a decay. Decays are defined as showers with ge 2 hits and le 8 hits within 30cms of a track end. At least one of the hits must be closer than 15cms to the track end (Carmen's criteria).

    Click on "TRACK WITH DECAY"

21. The event is categorised as a single contained track, with or without a proton recoil or decay or both. See note below on track+decay.

    Click on "CONTAINED TRACK"

22. The event is categorised as a single contained shower, with or without a proton recoil.

    Click on "CONTAINED SHOWER"

23. The event is categorised as a contained multiprong.

    Click on "CONTAINED MULTIPRONG"

24. There is one or more shield hits in time with a good internal T0 determination (blob or loom crossing). The shield time can be up to 5 ticks early and 25 ticks late with respect to the physical event T0.

    Click on "SHIELD HIT COINCIDENT WITH T0"

25. There is one or more shield hits at physically allowable times for events without a good internal T0 measurement. Shield times which move hits on good continuous tracks up to 1cm across the centre of a module are allowable. Beware of

slow drifting in the low field region of the centre of the tube which can produce hits apparently several cms over the module centre.

Click on "SHIELD HIT AT ALLOWED T0"

26. An event without a good internal T0 determination (blob or loom crossing) but with a physical shield hit is contained if the shield T0 is used but could point out of the detector if the shield hit is ignored. Events in this category are probably contained and can be used to study rock events but will not be included in the Silver file as background to neutrino events. Non-shield conditions are the same as for the "TRACK CAN POINT OUT" rule.

    Click on "CAN POINT OUT IF SHIELD IGNORED"

27. The event contains a 3-hit cluster outside the fiducial volume. This may indicate the presence of an entering track or shower that is a sign of activity external to the detector. (A cluster with 4 or more hits or a diffuse collection of hits is treated in rule (9), above).

    Click on "FATAL EXTERNAL SHOWER"

28. The event is contained but has some characteristic that makes it unlikely that it is a neutrino event. Type a comment detailing the characteristic. Multiple events where the separation of the events is more than 320 grams (2m) are examples of such events.

    Click on "NON-NEUTRINO-LIKE CEV (TYPE COMMENT)"

Notes

1. If the direction of a shower is well determined from its topology then the fact that as many as two hits in the tail of the shower end on a crack or point at a shield hit should not be taken as a fault. The same considerations apply to hits outside the fiducial volume.

2. To be counted as crossing a wire plane crack there should be some evidence that a track or the body of a shower has penetrated into the stack on the far side of

the crack. Clear drifting counts as such evidence. Just a blob in the wireplane could come from low momentum particles produced in a crack interaction.

3. A blob which will define a track or shower as starting in a wire plane must have at least two large anode hits and two large (non-crosstalk) cathode hits OR one large anode hits and 4 large (non-crosstalk) cathode hits, all starting within 1 tick. If the event is nearly perpendicular to the wire plane, the requirement relaxes to one large anode hit and two large (non- crosstalk) cathode hits. Detailed pulse shapes cannot be used, as they are not adequately modeled by the Monte Carlo.

4. An event will be failed as an "END LOOM FIDUCIAL VOLUME" failure if it can be stretched into the external 20cm by adjusting the loom crossing T0 to its maximum allowable extent.

5. Events with a track+recoil+decay should be flagged as such (only).

6. Events that trigger only in an end loom will not be automatically rejected.

7. A track+decay that is relatively linear should be classified as a shower instead.

8. A blob or equivalent hit in a wireplane at a well-known event T0 - with a geometry consistent with background activity - should reject an event. Use "Other Fatal" with an appropriate comment.

A.3 Scan rules for CVC events

A result of routine Filter and Bronze scanning of Soudan 2 data was that a sub-class of contained events was isolated for which the primary vertex was clearly imaged but a final state prong (usually a track) ended on an internal gap or load plate region of the calorimeter. These Contained Vertex end-on-Crack events (CVC events) were subsequently rescanned to identify those which are highly probable as neutrino interactions. Scanning Rules for CVCs were distributed via e-mail on June 17, 1998. The default rules and STING menu for CVC scanning are those of the Bronze Scan as listed in A.2. The CVC definitions below make reference to the numbered category definitions of the Bronze Rules.

A.3.1 Event classification

Events are to be classified as in the Bronze scan, with Bronze Category C descriptions 17 through 25 being applicable (21-23 = CONTAINED TRACK or SHOWER or MULTIPRONG, 17-20 = track which is or has SINGLE PROTON CANDIDATE or PROTON RECOIL or NEUTRON RECOIL or TRACK WITH DECAY, 25-26 = SHIELD at ALLOWED or COINCIDENT T0).

To the Bronze classifications, there is one embellishment: In events wherein shield hits occur AT ALLOWED or COINCIDENT T0s, the Scanner is requested to consider whether the event topology (e.g. candidate vertex and prong momentum flow) suggests point of origin inside the fiducial volume. In such a case, the Scanner is requested to record the comment "PCE CANDIDATE".

A.3.2 REJECTION and STRIKES:

In general, Bronze Scan rules and recording practices are to be adhered to, unless they are overruled by a CVC Scan OVER-RULE.

1. Bronze Category A: REJECTION

   Events are to be rejected which Fail the Filter Rules for the following cases:

   > Random trigger, Breakdown, Blob, Zen, Snake, Less than 6 matched hits, More than 500 ticks long, Crack Splat, and Crack/Crack at both ends of a single track .
   >
   > These categories remain valid and are Rejection categories.

   OVER-RULE: Since one of the goals of the CVC Scan is to isolate an "examination sample" of candidate PCEs, the following Filter categories are Inoperative - they are NOT TO BE USED:

   A/C fid. vol. exit

End loom fid. vol. exit

Crack fidvol.

[Crack/shield and Shield/Shield of course remain Inoperative, since they violate the principle of shield-blind scanning].

Bronze Rejection categories 5 through 8 and also 27, 28 remain Operative; an event can be classified and rejected as:

Vertex outside active region

Breakdown

Crack splat

Something else awful - you comment.

Fatal ext. shower - if it is distinct from the main body

Non-neutrino-like CEV - comment.

OVER-RULE: Bronze categories 2 through 4 are Inoperative - NOT TO BE USED (since they can eliminate PCE candidates):

Track can point in

Track leaves through module centre

Track leaves parallel to anodes.

2. Bronze Category B: STRIKES

   Bronze Strike categories which tag proximity to cracks and to the edge of the fiducial volume, are not useful for recovering CVC and PCE events and are not used:

   OVER-RULE: Strike categories 10 through 14 are Inoperative; DO NOT RECORD Tracks starts - near module center, near anode crack, near load plate crack, near wire plane crack, near edge of fiducial volume.

3. REJECTION for downward-going, stopping muons (DSMs):

   Downward muons which enter the calorimeter through the top or sides and which range to stopping with or without an endpoint decay, constitute the most abundant background for the goal of CVC scanning, which is to isolate events initiated by neutral particles within the detector.

An event is a DSM Candidate if it contains one and only one track-like segment whose more elevated end is compatible with entrance to the detector through a crack, module center, or region exterior to the fiducial volume.

Now consider the other end of the track-like segment which is of lower elevation:

> If the lower-elevation endpoint has zero or only a few (less than four) hits within 15 cm, the event is a DSM and can be REJECTed.
>
> If the lower-elevation endpoint has more than four hits but less than ten hits within a 15 cm radius, and if these hits comprise shower prong(s) but not an additional track, the event is a DSM (with endpt decay) and can be REJECTed.
>
> If an event is a DSM by the above criteria, then click on OTHER FATAL PROBLEM and enter as a Comment, either of
>
> > DSM (for Downward Stopping Muon), or
> >
> > DSMD (Downward Stopping Muon with endpt Decay).

Appendix B

Data Reduction at Tufts

The reduction of event reconstruction files to Data Save Tape (DST) records developed at Tufts involves a series of steps applied to all events in all reconstruction categories. An effort has been made to make the process as automated as possible using a combination of job control scripts and fortran code.

For each step described in this Appendix, a command (or a combination of commands) is run from a particular host system of the VMS cluster in the disk area stated. The input and output file directories are also specified. It is possible to run a "single procedure" for processing events in one reconstruction category in each of the RCN (CEV), CVC, VOA or PCE directories. Scripts are also provided for a "collective procedure" which handles all events in all reconstruction categories for each of the RCN (CEV), CVC, VOA or PCE directories. The input and output locations can be modified in the scripts.

1. **On merging reconstructed files into one Reconout file:** After reconstruction, each event is written to a single binary file (in RECONOUT format). Subsequently all event files are joined into one file per reconstruction category in each of the main CEV, CVC, VOA and PCE directories. In order to add new events, to change an event category, or to eliminate an event from the process, the corresponding connect.com script must be modified. As of 9-15-98, files in the RCN track sample are consistent with the "collaboration-standard" track sample which was entirely reconstructed by physicists.

   The input files are located in disk$neutrino:[USER.DWALL.RECONOUT.*]

and the output files are *.rcn files left in the disk area directory. A connect.com file is required for each sub-directory in the disk area (these commands do not need to run from a particular host). For RCN events, we use disk$cosmos:[MSANCHEZ.RECONOUT.RCN]; the subdirectories are: [MPDATA], [MPMC], [MPROCK], [QESHWDATA], [QETRKDATA], [QESHWMC], [QETRKMC], [QESHWROCK] and [QETRKROCK]. For CVC,VOA and PCE, we use disk$cosmos:[MSANCHEZ.RECONOUT.*] with no subdirectories (the sub-categories in PCE sample changed to MP*, PCE* and UPTRK*, where * stands for DATA, MC and ROCK).

To run a single procedure, use @connect.com in each sub-directory to produce a single merged file (*.rcn, *.cvc, *.voa or *.pce). To run a collective procedure, use @all-*-connect.com in each main category directory to produce all merged files (*.rcn, *.cvc, *.voa and *.pce).

2. **On producing an ascii card image file from Reconout file:** The RDST8 program converts the reconstructed banks for each event into ASCII card images (DSF files). A description of the DSF format is given in Appendix E of Ref. [46].

   The input files are disk$cosmos:[MSANCHEZ.RECONOUT.*] *.rcn, *.cvc, *.voa and *.pce. The output files are disk$soudan_2:[MSANCHEZ.RDST8.*]*.dsf, *.log, *.out. Use rdst8.com and files specified therein. These commands must be run from hosts tuhep7 or tuhep1. We use the disk area

   disk$neutrino:[MSANCHEZ.RDST8].

   To run a single procedure, use @rdst8-'*p2*'.com '*p1*'; here, *p1* is the relevant reconstruction category and *p2* corresponds to RCN, CVC, PCE or VOA. To run a collective procedure, use @all-rdst8-'*p2*'.com. This will produce a complete RCN, CVC, PCE or VOA collection of *.dsf.

3. **On producing WL analysis files from ascii card image file:** For each event category, the output of the RDST8 package is processed with the MCFLAV package. The package outputs several ASCII files with different combinations of physical variables and flags.

The input files are disk$soudan_2:[MSANCHEZ.RDST8.*]*.dsf. The output files are disk$soudan_2:[MSANCHEZ.*.*]*.dat. Job command files are mcflav-*.com and files specified therein. These commands run from host tuhep2 and use disk area disk$soudan_2:[MSANCHEZ.RDST8]

To run a single procedure, use @mcflav.com '*p2*' '*p1*', where *p1* is the relevant reconstruction category and *p2* corresponds to RCN, CVC, PCE or VOA. To run a collective procedure, use @all-'*p2*'-mcflav.com will produce a complete set of *.dat.

4. **On updating flavor tags of multiprongs in WL analysis files:** For multiprongs and partially contained 2-prongs, MCFLAV determines the prong with the highest momentum and outputs the results to an ascii file (*-053.DAT), where * specifies the reconstruction category. This file is essential for the flavor tagging process. The file is first updated with the contents of the history file for flavor tags, it is then printed and the flavor tags are decided for the newer events. New tags are then input using a text editor. Lastly, a short script is run in order to ensure the history file is updated.

   The input files for this task are disk$soudan_2:[MSANCHEZ.*p2.p1*]*-053.dat and disk$soudan_2:[MSANCHEZ.*p2*.TEMP]*-053.dat. The output files are flavor tagged *-053.dat. Command files to run the jobs are prog53-'*p2*'.com, update53.com and files specified therein. These commands are run from host tuhep2; the disk areas used is disk$soudan_2:[MSANCHEZ.'*p2*'].

   To run a single procedure, use @prog53-'*p2*'.com '*p1*', where *p2* is the relevant multiprong file type and *p1* corresponds to the RCN, CVC, PCE or VOA. New events will initially be assigned tag values; these will be 0.0 and later modified with a text editor. When using NEDIT, do not forget to erase the first blank line and shift one space to the right after selecting entire text (first column must have 3 spaces). After flavor tagging of new events, one must run update53.com. This ensures that a safe copy of the new flavor tagging will kept.

5. **On preparing Ntuple and ascii files from WL analysis files:** The final

step in our processing chain is to produce a simple ASCII file and a NTUPLE with only the physical quantities needed for the analysis.

The input files for this are *.dat files. The output files are

disk$soudan_2:[MSANCHEZ.FINALFILES]*.asc. Job command files are all-ntupler.com, sgl-ntupler.com and files specified therein. The commands are run from host tuhep2. We use disk area

disk$soudan_2:[MSANCHEZ.NTUPLER] fo this task.

To run a single procedure for one file use @sgl-ntupler.com '*p2 p1*', where *p2* is the relevant RCN, CVC or VOA directory and *p1* is the sub-category. To run a collective procedure, use @all-ntupler.com '*p2*', where *p2* is the relevant RCN, CVC, or VOA directory. For PCE use @all-pce-ntupler.com The output file structure is has the following format:

RUN|EVT|VAR|TOP|XC|IP|zenith|L |EF4|TMAG|ELEAD|EF1|EF2|EF3

where:

- RUN|EVT: run|event numbers
- VAR: 1=gold 2=rock 3=mc
- TOP: 1=trk 2=shw 3=mp
- XC: (flavor tag) 1=trk 2=shw -1=NC -9.9=? 99.9=trk or shw
- IP:
- zenith: $\cos\theta_z$
- L: L, path length
- EF4: E_{vis}
- TMAG: magnitude of $\vec{P}_{vis}$
- ELEAD: magnitude of leading lepton momentum
- EF1|EF2|EF3: x,y,z components of $\vec{P}_{vis}$

Appendix C

Final DST format

```
30Aug2002TK - Tufts MaxiDST contents:

All variables are contained in common blocks within CMAX02.INCLUDE

(1) The Mini part:

(a1) The Recon card - Header section:

CTYPi  = continuation flag ('card type' of the card to follow):       (I1)
       = 0 ... no continuation record
       = 1 ... continuation record present: MC truth
       = 2 ... continuation record present: PCE
R      = run number                                                    (I6)
EV     = event number                                                  (I5)
GRMC   = 1 ... gold data                                               (I2)
         2 ... rock data
         3 ... Monte Carlo event
TSMP   = 1 ... track                                                   (I2)
         2 ... shower
         3 ... multiprong
         4 ... proton
```

```
FLAVR  = 1 ... nu_mu                                                (I3)
         2 ... nu_e
         3 ... NC
         4 ... nu_mu or nu_e
         5 ... nu_mu or NC
         6 ... nu_e or NC
         7 ... completely ambiguous
         9 ... rejected
         REJECT*10 + FLAVR
         where REJECT = 1 ... (PCE) vtx OFV
                        2 ... (PCE) incoming hadron-like
                        3 ... (PCE) opposite-hemisphere down-stopping muon
                        4 ... (PCE) downgoing stopping muon
                        6 ... failed detector checks
                        7 ... (CEV) small shower (< 9 hits, incl. recoil)
                        8 ... to be remeasured
                        9 ... general reject
RECOIL = 0 ... event without a recoil                               (I2)
         1 ... event with a proton recoil / n ... number of proton recoils?
        -1 ... event with a neutron recoil

(a2) The Recon card - Reconstructed/measured variables:

COSZEN = cosine of the zenith angle (from p_tot)                    (F9.6)
L      = neutrino path length (calculated from COSZEN and neutrino  (F9.2)
         production height chosen according to one of several prescriptions)
EVIS0  = total visible energy of the event                          (F8.1)
       = sum of energies of all leptons and pions
         plus sum of kinetic energies of all nucleons
PLEPT  = final_state lepton momentum magnitude                      (F8.1)
        NOTE: There are few events with PLEPT = 0.0 - these are
```

```
              low energy lone tracks with hadronic signature (pi or proton),
              i.e. there is no muon in the event
PVISX,PVISY,PVISZ = total visible momentum of the event           (3F8.1)
LOG_LE = log(L/E)                                                  (F7.4)
CEVCVC = 1 ... CEV                                                 (I2)
         2 ... CVC
         3 ... VOA
         4 ... PCE
         5 ... (work in progress - PCEs found in the CVC scan)
         6 ... CEVPCE (contained events (multis) found by the PCE Filter)
         7 ... upgoing stopping muon
         8 ... "in-downs" (selected uptrks reclassified)
VS     = total number of intime shield hits (adj. groups)          (I3)
       = -1 ... silver-turned-gold
       = -9 ... no value)
D      = vertex depth in the detector (-99.99 = no value)          (F7.1)
VSPCE  = For PCEs: number of VS hits caused by                     (I3)
         prongs outgoing from the evt
       = -9 ... no value
MSFLG  = Multiple_Scattering_FLaG for PCEs (Tony's scan decisions)  (I3)
       = 1 ... no m.s.
         2 ... dubious m.s.
         3 ... some m.s.
         4 ... obvious m.s. but not rangeout
         5 ... obvious m.s. with rangeout
         -1 ... no value; event scanned, but value not appropriate
         -9 ... no value
PRHITS = Number of (non-leaving) prong hits for 2-pr PCEs          (I3)
         (Tony's scan count)
         -1 ... no value; event scanned, but value not appropriate
         -9 ... no value
```

```
RECHIT = Number of hits for the recoil proton, if any, trk&shw only      (I3)
            = -9 ... no value
INWD   = Inwardness                                                      (F6.2)
            = -9.99 ... no value
HILOFL = HiRes vs. LoRes flag                                            (I2)
              =  1 ... HiRes;
              =  0 ... .NOT.HiRes (LoRes CC or any NC or ambig)
PCEFL  = PCE_acceptance flag                                             (I2)
              =  0 ... .NOT. good PCE
              =  1 ... good numu PCE
              =  2 ... good non-numu PCE
FL300  = reject flag for Peter's 300 MeV cut                             (I2)
              =  1 ... fails 300 MeV cut
              =  0 ... does not fail 300 MeV cut
```

(b) Monte Carlo truth:

```
COSZTR = cosine(zenith)                                                (F9.6)
LTRU   = neutrino path length (calculated from COSZTR and h)           (F9.2)
ETRU   = true EVIS                                                     (F8.1)
PLEPTR = true PLEPT                                                    (F8.1)
PTRU   = true PVIS                                                     (3F8.1)
LOG_LET= true log(L/E)                                                 (F7.4)
NUTYPE = incoming neutrino type                                        (I3)
ILEPOUT= outgoing lepton type                                          (I3)
HWT(5) = Hugh's weights for Monte Carlo events                         (5F6.3)
         (1) weight for MC events with run < 66933
         (2) to correct Bartol87 flux to Bartol96 flux in MC
         (3) to correct solar cycle calculation to new neutron_monitor data
         (4) to correct Bartol 1-D flux to Battistoni 3-D flux
```

(5) spare

(c) PCE kinematics:

MULEN	= track length of the leaving muon, in cm	(F7.2)
MUMOM	= momentum of the lv_mu, in MeV/c (calculated using the visible track length as the range)	(F9.2)
NEWMOM	= momentum calculated using track length modified according to its multiple scattering flag MSFLG	(F9.2)
MU1(3)	= unit vector in the muon direction at the vertex	(3F9.5)
NONMU(4)	= fourvector of the hadronic system (all non-mu prongs)	(4F10.2)

(2) The Maxi part:

For each and every card, columns 1 through 16 contain

CEVRUN	Run number	(I7)
CEVEVT	Event number	(I5)
NN	Card number (within the event)	(I4)

Formats for the various card types are given below, beginning with column 17.

(a) HEADER Card:

Topology information:

NTRK	Total number of tracks	(I3)
NSHW	Total number of showers originating at the primary vtx	(I3)

NSHWDK	Total number of decay showers	(I3)
NPROT	Total number of protons at the primary vtx	(I3)
NRPROT	Total number of remote protons	(I3)

Event kinematics:

EVIS	Total visible energy (kin. en. for protons), MeV	(F10.2)
NETMOM	Total momentum, MeV/c	(F10.2)
INVMAS	Total invariant mass, MeV/c**2	(F10.2)
FASTT	Fastest track (track number)	(I4)
FASTS	Fastest shower (shower number)	(I4)
FASTPR	Fastest prong type (1=trk, 2=shw)	(I3)

T0 info for veto shield hit association:

T0		(I4)
T0MIN (currently not used)		(I4)
T0MAX (currently not used)		(I4)

LEPTPR	Lepton prong type (1=trk, 2=shw)	(I3)
LEPNUM	Lepton track or shower number	(I3)

(b) VERTEX card (one per event)

XYZVTX	x, y, z of the vertex, in cm.	(3F8.2)

(c) TRACK Geometry Card (one per track)

I	Track number	(I3)
XYZTRK(I,1,j),j=1-3	x, y, z of the beg. mark	(3F8.2)
XYZTRK(I,2,j)	x, y, z of the direction_point mark	(3F8.2)

TRANGE(I)	Range in g/cm**2 (length of the TRAJEC fit * 1.6)	(F8.2)
REMOTE(I)	Remote track flag (0 = not remote, 1 = remote)	(I2)
SCATR(I)	Scatter flag (0 = track does not scatter, 1 = it does)	(I2)

(d) TRACK KINEMATICS Card (one per track)

I	Track number	(I3)
TRKID(I)	Particle ID (1=mu, 2=pi, 3=proton)	(I3)
PXYZT(I,j)	Track momentum Px, Py, Pz in MeV/c	(3F9.2)
ETRK(I)	Track energy in MeV	(F9.2)
PMAG(I)	Momentum magnitude, MeV/c	(F9.2)
TMASS(I)	Mass, MeV/c**2	(F8.3)
ESHITS(I)	End-point shower, number of hits	(I3)
ESENRG(I)	End-point shower energy, MeV	(F7.2)
NTRHIT(I)	Number of hits in the fit for this track (= -99 ... no value)	(I4)

(e) SHOWER GEOMETRY Card (one per shower)

I	Shower number	(I3)
XYZSHW(I,1,j)	x, y, z of shower vertex	(3F8.2)
XYZSHW(I,2,j)	x, y, z of the direction point	(3F8.2)

(f) SHOWER KINEMATICS Card (one per shower)

I	Shower number	(I3)
PXYZS(I)	Shower momentum Px, Py, Pz in MeV/c	(3F9.2)
EHITS(I)	Shower energy in MeV from the number of hits	(F9.2)
EPHS(I)	Shower energy in MeV from the total anode pulse height (currently not used)	(F9.2)
NHITS(I)	Number of 3D hits	(I5)

PHS(I)	Total anode pulse height (currently not used)	(F9.2)

(g) EVENT KINEMATICS Card:

TOTAL(j)	Event total momentum Px, Py, Pz in MeV/c	(3F10.2)
TOTAL(4)	Event total energy in MeV	(F10.2)

SCALTD, SCALTM, SCALSD, SCALSM =

	Energy scale factors (preset to 1.000)	(4F6.3)

Bibliography

[1] Y. Fukuda et al., *Evidence for oscillation of atmospheric neutrinos*, Phys. Rev. Lett. **81**, 1562–1567 (1998).

[2] G. J. Feldman and R. D. Cousins, *A Unified approach to the classical statistical analysis of small signals*, Phys. Rev. **D57**, 3873–3889 (1998).

[3] K. Hagiwara et al., *Review of particle physics*, Phys. Rev. **D66**, 010001 (2002).

[4] B. Kayser, Neutrino mass, mixing, and oscillation, in *Boulder 2000, Flavor physics for the millennium*, pages 625–650, Boulder, Colorado, June 2000.

[5] M. C. Gonzalez-Garcia and Y. Nir, *Developments in neutrino physics*, Rev. Mod. Phys. **75**, 345 (2003).

[6] B. T. Cleveland et al., *Measurement of the solar electron neutrino flux with the Homestake chlorine detector*, Astrophys. J. **496**, 505–526 (1998).

[7] W. Hampel et al., *GALLEX solar neutrino observations: Results for GALLEX IV*, Phys. Lett. **B447**, 127–133 (1999).

[8] J. N. Abdurashitov et al., *Measurement of the solar neutrino capture rate with gallium metal*, Phys. Rev. **C60**, 055801 (1999).

[9] E. Bellotti, *First results from GNO*, Nucl. Phys. Proc. Suppl. **91**, 44–49 (2001).

[10] Y. Fukuda et al., *Solar neutrino data covering solar cycle 22*, Phys. Rev. Lett. **77**, 1683–1686 (1996).

[11] Y. Fukuda et al., *Measurements of the solar neutrino flux from Super-Kamiokande's first 300 days*, Phys. Rev. Lett. **81**, 1158–1162 (1998).

[12] Q. R. Ahmad et al., *Direct evidence for neutrino flavor transformation from neutral-current interactions in the Sudbury Neutrino Observatory*, Phys. Rev. Lett. **89**, 011301 (2002).

[13] K. Eguchi et al., *First results from KamLAND: Evidence for reactor anti- neutrino disappearance*, Phys. Rev. Lett. **90**, 021802 (2003).

[14] R. Becker-Szendy et al., *Atmospheric neutrinos: Results from IMB*, Prepared for International Symposium on Neutrino Astrophysics, Takayama / Kamioka, Japan, 19-22 Oct 1992.

[15] K. S. Hirata et al., *Observation of a small atmospheric ν_μ/ν_e ratio in Kamiokande*, Phys. Lett. **B280**, 146–152 (1992).

[16] Y. Fukuda et al., *Atmospheric muon-neutrino / electron-neutrino ratio in the multiGeV energy range*, Phys. Lett. **B335**, 237–245 (1994).

[17] W. W. M. Allison et al., *The atmospheric neutrino flavor ratio from a 3.9 fiducial kiloton-year exposure of Soudan 2*, Phys. Lett. **B449**, 137–144 (1999).

[18] M. Ambrosio et al., *Matter effects in upward-going muons and sterile neutrino oscillations*, Phys. Lett. **B517**, 59–66 (2001).

[19] M. H. Ahn et al., *Indications of neutrino oscillation in a 250-km long- baseline experiment*, Phys. Rev. Lett. **90**, 041801 (2003).

[20] C. Athanassopoulos et al., *Evidence for $\nu_\mu \to \nu_e$ neutrino oscillations from LSND*, Phys. Rev. Lett. **81**, 1774–1777 (1998).

[21] K. Eitel, *Latest results of the KARMEN2 experiment*, Nucl. Phys. Proc. Suppl. **91**, 191–197 (2000).

[22] J. Wolf, *Final LSND and KARMEN-2 neutrino oscillation results*, Prepared for International Europhysics Conference on High- Energy Physics (HEP 2001), Budapest, Hungary, 12-18 Jul 2001.

[23] J. M. Link, *Short baseline neutrino oscillations and MiniBooNE*, Nucl. Phys. Proc. Suppl. **111**, 133–135 (2002).

[24] M. Apollonio et al., *Limits on neutrino oscillations from the CHOOZ experiment*, Phys. Lett. **B466**, 415–430 (1999).

[25] S. M. Bilenky, D. Nicolo, and S. T. Petcov, *Constraints on $|U(e3)|^2$ from a three-neutrino oscillation analysis of the CHOOZ data*, Phys. Lett. **B538**, 77–86 (2002).

[26] F. Boehm et al., *Final results from the Palo Verde neutrino oscillation experiment*, Phys. Rev. **D64**, 112001 (2001).

[27] B. Kayser, Neutrino physics, superbeams, and the neutrino factory, in *Proceedings of 4th NuFact '02 Workshop (Neutrino Factories based on Muon Storage Rings)*, London, England, July 2002.

[28] *Soudan 2: A 1000 ton tracking calorimeter for nucleon decay*, Technical report, September 1981.

[29] W. W. M. Allison et al., *Contained neutrino events observed in Soudan-2*, Nucl. Phys. Proc. Suppl. **35**, 427–429 (1994).

[30] H. Gallagher, *Neutrino oscillation searches with the Soudan 2 detector*, PhD thesis, University of Minnesota, April 1996.

[31] S. Werkema, *Monte Carlo evaluation of the atmospheric neutrino background to nucleon decay in the Soudan 2 detector*, PhD thesis, Univerisity of Minnesota, July 1989.

[32] D. Schmid, *First nucleon decay results from the Soudan 2 detector*, PhD thesis, Univerisity of Minnesota, May 1992.

[33] D. Roback, *Measurement of the atmospheric neutrino flavor ratio with the Soudan 2 detector*, PhD thesis, University of Minnesota, August 1992.

[34] G. Barr, T. K. Gaisser, and T. Stanev, *Flux of atmospheric neutrinos*, Phys. Rev. **D39**, 3532–3534 (1989).

[35] G. Barr, *The separation of signals and background in a nucleon decay experiment*, PhD thesis, University of Oxford, December 1987.

[36] H. Gallagher, *The NEUGEN neutrino event generator*, Nucl. Phys. Proc. Suppl. **112**, 188–194 (2002).

[37] H. Fesefeldt, *The simulation of hadronic showers: physics and applications*, PITHA-85-02.

[38] R. L. Ford and W. R. Nelson, *The EGS code system: computer programs for the Monte Carlo simulation of electromagnetic cascade showers (Version 3)*, SLAC-0210.

[39] W. R. Nelson, H. Hirayama, and D. W. O. Rogers, *The EGS4 code system*, SLAC-0265.

[40] D. Petyt, *Extraction and analysis of partially contained events in Soudan 2*, Soudan-2 internal note PDK-771, August 2001.

[41] H. Gallagher, *Detector perfomance checks for CEV data*, Soudan-2 internal note PDK-687, November 1997.

[42] T. Kafka and W. Mann, *The Hi-Res samples of CVC and VOA events*, Soudan-2 internal note PDK-721, March 1999.

[43] C. Garcia-Garcia, *El experimento de Soudan 2 para el estudio de la estabilidad de la materia: interacciones de neutrinos*, PhD thesis, Univerisidad de Valencia, September 1990.

[44] P. Litchfield, *Protonicity*, Soudan-2 internal note PDK-696, March 1998.

[45] W. Leeson, *Measuring procedures for multi-tracks contained events*, Soudan-2 internal note PDK-652, July 1996.

[46] W. Leeson, *Study of atmospheric neutrino interactions and search for nucleon decay in Soudan 2*, PhD thesis, Tufts University, December 1995.

[47] H. Tom, Search for Neutrino Oscillation Effects Using Neutrino Zenith Angle and L/E Distributions in Soudan 2, Master's thesis, Tufts University, May 1998.

[48] P. Litchfield, *CEV background fitting*, Soudan-2 internal note PDK-777, October 2001.

[49] W. Mann, Private communication, October 2002.

[50] R. Thompson and W. Mann, *Partially contained events of non-ν_μ flavor*, Soudan-2 internal note PDK-790, July 2002.

[51] H. Gallagher, *Nuclear binding energy and recoil identification in quasi-elastic neutrino scattering*, Soudan-2 internal note PDK-785, February 2002.

[52] W. Mann, Private communication, February 2002.

[53] H. Gallagher, *Shower energy calibration issues*, Soudan-2 internal note PDK-725, May 1999.

[54] J. Schneps, *Calibration of Soudan 2 Shower energies*, Soudan-2 internal note PDK-764, May 2001.

[55] P. Litchfield, *Calibration of Soudan 2 momenta*, Soudan-2 internal note PDK-799, November 2002.

[56] B. Speakman and H. Gallagher, *Impact of tracking cutoffs on electromagnetic simulations in Soudan 2*, Soudan-2 internal note PDK-769, May 2001.

[57] H. Gallagher and B. Speakman, *A method for correcting Monte Carlo shower energies*, Soudan-2 internal note PDK-774, September 2001.

[58] H. Gallagher and K. Ruddick, *The use of production height distributions in atmospheric neutrino analyses*, Soudan-2 internal note PDK-784, March 2002.

[59] M. Goodman, Soudan 2 collaboration meeting at RAL, March 2002.

[60] J. Schneps, *Depth fits for high and low resolution events and the ratio of ratios, old and new*, Soudan internal note PDK-755, August 2000.

[61] J. Schneps, *Multivariate analysis of atmospheric neutrino data: Part 1 - the ratio of ratios*, Soudan-2 internal note PDK-690, November 1997.

[62] J. Schneps, Soudan 2 collaboration meeting, January 2002.

[63] V. Agrawal, T. K. Gaisser, P. Lipari, and T. Stanev, *Atmospheric neutrino flux above 1 GeV*, Phys. Rev. **D53**, 1314–1323 (1996).

[64] M. Honda, T. Kajita, K. Kasahara, and S. Midorikawa, *Calculation of the flux of atmospheric neutrinos*, Phys. Rev. **D52**, 4985–5005 (1995).

[65] E. V. Bugaev and V. A. Naumov, *On the interpration of the Kamiokande neutrino experiment*, Phys. Lett. **B232**, 391–397 (1989).

[66] D. H. Perkins, *A new calculation of atmospheric neutrino fluxes*, Astropart. Phys. **2**, 249–256 (1994).

[67] G. Battistoni et al., *A 3-dimensional calculation of atmospheric neutrino flux*, Astropart. Phys. **12**, 315–333 (2000).

[68] T. K. Gaisser and M. Honda, *Flux of atmospheric neutrinos*, Ann. Rev. Nucl. Part. Sci. **52**, 153–199 (2002).

[69] http://ulysses.uchicago.edu/NeutronMonitor/Misc/neutron2.html.

[70] M. Honda et al., in *Proc. 27th Int. Cosmic Ray Conf.*, page 1162, 2001.

[71] R. Engel et al., Hadronic interactions for atmospheric cascades, in *Proc. 27th Int. Cosmic Ray Conf.*, page 1381, 2001.

[72] T. K. Gaisser, *Atmospheric neutrino flux: A review of calculations*, Nucl. Phys. Proc. Suppl. **87**, 145–151 (2000).

[73] M. Sanchez and J.Schneps, *The ratio of ratios, ν_μ disappearance rate and normalization in Soudan 2*, Soudan-2 internal note PDK-804, June 2003.

[74] M. Sanchez et al., *Neutrino oscillation parameter from a chi-square analysis of Soudan 2 L/E distributions and R for high resolution contained events*, Soudan-2 internal note PDK-736, September 1999.

[75] C. Caso et al., *Review of particle physics*, Eur. Phys. J. **C3**, 1–794 (1998).

[76] A. Stuart and J. Ord, *Kendall's Advanced Theory of Statistics, Vol. 2, Classical Inference and Relationship*, Oxford University Press, New York, 5th edition, 1991.

[77] W. Press, B. Flannery, S. Teukilsky, and W. Vetterling, *Numerical Recipes in Fortran*, Cambridge University Press, 1986.

[78] M. Sanchez, Soudan 2 collaboration meeting, January 2002.

[79] C. Yanagisawa, Presented at NOON '03 for the Super-Kamiokande collaboration, Kanazawa, Japan, Feb 2003.

[80] M. Ambrosio et al., hep-ex/0304037 (April 2003).

[81] M. Goodman, D. Roback, and P. Litchfield, *Filter scan rules*, Soudan-2 internal note PDK-519, June 1992.